Near-surface Geophysical Imaging of Complex Structures: Meteor Crater, AZ and Jemez Pueblo, NM

A Thesis Presented to

the Department of Earth and Atmospheric Sciences

University of Houston

In Partial Fulfillment

of the Requirements for the Degree of

Master of Science

By

Arkadiusz Turolski

May 2013

Near-surface Geophysical Imaging of Complex Structures: Meteor Crater, AZ and Jemez Pueblo, NM

_____

Arkadiusz Turolski

APPROVED:

_____

Dr. Robert R. Stewart, Advisor

_____

Dr. Stuart A. Hall, Committee Member

_____

Dr. David A. Kring, Committee Member

_____

Dean, College of Natural Sciences and Mathematics

Acknowledgements

There are many people and organizations to acknowledge. First I would like to thank Dr. Robert Stewart for his guidance and stewardship throughout this project, whose help made this work feasible. I thank Drs. Kring, Liner, and Hall for their expertise and invaluable insight throughout this long process. A special thanks to Eray Kocel and Bode Omoboya for their countless hours in helping me process and interpret geophysical data. Thanks to Marisa Palucis from UC Berkeley for making the LiDAR data available. I thank Roy Burnstad from Saudi Aramco for his tips on shallow seismic processing and Neda Bundalo from Marathon Oil for her insight on potential field processing. I would also like to thank The Barringer Crater Company and The Pueblo of Jemez for giving me the unique opportunity to work on such important geological projects.

The results presented in this paper also rely on the data collected at the Tucson Magnetic Observatory—I thank the USGS for supporting its operation and INTERMAGNET for promoting high standards of magnetic observatory practice (www.intermagnet.org). I also acknowledge the Allied Geophysical Laboratories and its staff for providing assistance and acquisition equipment. I would also like to extend my gratitude to Gedco, Geosoft, and Paradigm Geophysical for technical and software support. And finally, I thank the many others who were a part of this project, from beginning to end. Thank you.

Near-surface Geophysical Imaging of Complex Structures: Meteor Crater, AZ and Jemez Pueblo, NM

An Abstract of a Thesis

Presented to

the Department of Earth and Atmospheric Sciences

University of Houston

In Partial Fulfillment

of the Requirements for the Degree of

Master of Science

By

Arkadiusz Turolski

May 2013

Abstract

This work is the culmination of two independent but related projects regarding the near-surface. The first involves a geophysical examination of Barringer Meteorite Crater (a.k.a. Meteor Crater) in northern Arizona. The objective, to obtain ground-truth data to better characterize the subsurface, was accomplished via a 660 m 2-D seismic line and several potential field surveys. The reflection seismic results, although lacking in vertical resolution, indicate several prominent horizons and possible faults. A tomographic inversion of the refraction data reveals a complex near-surface velocity structure that is in agreement with a faulted subsurface. Forward models based on the gravity and magnetic surveys were created and complement the seismic findings—they too indicate a possible fault at 250 m along the seismic survey and suggest the top of the Moenkopi to be at a depth of 20-30 m below the surface, similar to results obtained by Roddy et al. (1975).

The purpose of the 2nd study was to characterize the near surface at Pueblo of Jemez, New Mexico, to assess the geothermal potential of the geologically active rift zone via a 475 m 2-D seismic reflection line and a 1.44 km gravity survey. Specifically, imaging faults in the subsurface may indicate possible hydrothermal migration pathways. The results show beds dipping to the south at 5°, cross-cut by the large Indian Springs fault zone, consistent with previous geologic work in the area.

Table of Contents

List of Figures

Chapter 1

Introduction

1.1 Motivation/Objective

The main purpose of this study is to gain a better understanding of imaging complex near surface structures through the integration of various geophysical techniques, namely seismic and potential field methods. Initially, two projects were undertaken as separate works. As they progressed, the Meteor Crater and the Pueblo of Jemez projects were combined into a single larger work as a result of their similar goals—imaging the near-surface.

The impetus for geophysical work at Meteor Crater was several fold: 1) to help unravel the mystery of the astrobleme's square shape, 2) to delineate the thickness of the ejecta blanket, and 3) to characterize the crater's rock properties. Recent geological studies (Poelchau et al., 2009) indicate that pre-impact fractures and joint sets in the target lithologies may have caused a non-uniform distribution of energy from the center of the impact, resulting in the crater's square-like shape. To test this hypothesis, seismic and potential field data were acquired in the hopes of locating these fractures (activated as faults) to understand their role in the cratering process. The results of this work will aid in our comprehension of impact mechanics on Earth and beyond.

Unlike the Meteor Crater study, which is driven primarily by scientific understanding, the geophysical work at Jemez Pueblo is driven by resource potential. The Pueblo of Jemez is located atop a shallow geothermal reservoir that is part of the Valles Caldera volcanic terrain. Because of the presence of hot springs in the area, the region has the potential to be a geothermal energy resource. The Pueblo of Jemez Reservation, in partnership with the Department of Energy, are interested in exploring the geologic and economic feasibility of such an undertaking. To address this issue, a detailed structural study of the subsurface needs to be completed, which this project helps to achieve. To assess the area's geothermal capacity and gain an insight into potential hydrothermal circulation, seismic and gravity measurements were made. The hope is that this study will help in our understanding of the near-surface, which will lead to better-informed economic decisions.

1.2 Tools & Software

1.2.1. Acquisition

The Meteor Crater and Pueblo of Jemez geophysical data were acquired, processed, and interpreted using the same field equipment and software. The seismic data were acquired using an accelerated weight drop (AWD) source from the back of a pick-up truck (Fig. 1.1). This propelled energy generator (PEG) consisted of a 40 kg (88 lb.) metal cylinder that was mechanically lifted and then dropped onto a large metal plate on the ground with the assistance of a heavy-duty elastic band. When the weight drop struck

the base plate, an impulse trigger mounted on the base plate was used to begin recording seismic data. The receivers, consisting of 14 Hz single component (1-C) geophones, were connected to 24-bit Geometrics Geode analog-to-digital (A/D) converters. The data were acquired using Geometrics acquisition software on rugged field laptops.

Fig. 1.1. Photo of seismic acquisition crew (author on right) using the weight drop mechanism on the rear of a pick-up truck as the source of the seismic acquisition. (Photo courtesy of Eray Kocel).

Gravity data at Meteor Crater and Jemez Pueblo were acquired using a Scintrex CG-5 Autograv gravity meter (Fig. 1.2). The relative gravimeter is capable of 1 microgal resolution and an instrument drift of 0.02 mGal/day under favorable conditions. Although impressive, the actual resolution of the acquired field data is more likely 0.01 mGal because of processing limitations.

Fig. 1.2. Scintrex CG-5 Autograv gravity meter. (Photo courtesy of Scintrex Limited).

The magnetic data were acquired using a Geometrics G-856AX proton precession magnetometer. The magnetometer recorded the absolute total magnetic field at each station location. The magnetometer boasts a resolution of 0.1 nT and an accuracy of 0.5 nT, well within the range needed for the purposes of this study.

Ultrasonic measurements of rock samples were also collected at Meteor Crater to estimate outcrop velocities of the formations of interest. A V-Meter MK-III ultrasonic measurement system was utilized for this task. Although primarily used for concrete flaw detection, the system is ideal for any small-scale velocity measurements. To measure the distance between the transducer and the receiver, a digital caliper was used.

1.2.2. Processing

The seismic data were processed using Gedco's Vista and Paradigm Geophysical's FOCUS processing software. These software packages were used because the data sets were small, the processing workflows simple, and the interfaces user-friendly and intuitive. The purpose of using two software packages was to utilize each one's strengths in the processing workflow: Vista, often used as a quick QC of acquired data in the field, was used mainly in the preprocessing stage of the workflow such as header manipulation, geometry definition/binning, killing noisy traces, and refraction analysis; FOCUS, on the other hand, was used for the more intensive processing steps such as deconvolution, velocity analysis, NMO correction, and migration. The software packages were made available to all University of Houston geoscience students for free on laboratory workstations.

Gravity data were processed using Microsoft Excel. Specialized software was not necessary since the processing workflows consist of numeric data manipulation via simple equations. Like the gravity data, the magnetic data were also processed using Microsoft Excel. However, to obtain the diurnal variation and main field correction values, other software were used. The diurnal variation corrections were obtained from Intermagnet, a global network of magnetic observatories. The closest magnetic observatory to Meteor Crater was in Tucson, Arizona. The main field corrections at each station location were calculated using the 11^{th} generation of the International Geomagnetic Reference Field 11 via a calculator on the National Oceanic and Atmospheric Administration's (NOAA's) website.

1.2.3. Interpretation

Simple seismic interpretation was completed using VISTA and FOCUS software. Although the software packages are primarily used for data processing, they also contain basic seismic interpretation tools such as horizon picking. These interpretation tools were sufficient since the scope of this study was mainly concerned with gross structural interpretation.

The potential field data were interpreted using Microsoft Excel and Geosoft's GM-SYS extension of the Oasis software. Microsoft Excel was used to remove the regional field from the processed data sets to focus on the small-wavelength (near-surface) features within the residual field. Forward models of the geologic subsurface were created in GM-SYS to model the resulting potential fields and compare them to the acquired data.

1.3 Data

1.3.1. Meteor Crater, Arizona

The acquisition of acoustic, gravity, and magnetic data at Meteor Crater was undertaken from May 17th to May 20th, 2010. The main focus of this study, a 660 m 2-D single component seismic line (the first reflection seismic study at Meteor Crater), was acquired along the southern portion of the ejecta blanket just beyond the crater rim. Data were recorded for 3 seconds with a sampling rate of 0.5 ms. As a result, the Nyquist

frequency of the data is 1000 Hz, which is well above the highest frequency that the signal of interest is expected to contain. A total of 228 shots spaced 3 m apart were acquired during the survey, each shot gather consisting of 120 traces. This equals to a total number of 27,360 traces. The dominant frequency of the raw data is about 55 Hz, as is shown in Fig. 1.3 of a typical shot gather. Assuming an average near-surface velocity of 2000 m/s (typical of this study area), the expected wavelength is about 35 m, which corresponds to a vertical resolution limit of 9 m (Kallweit and Wood, 1982).

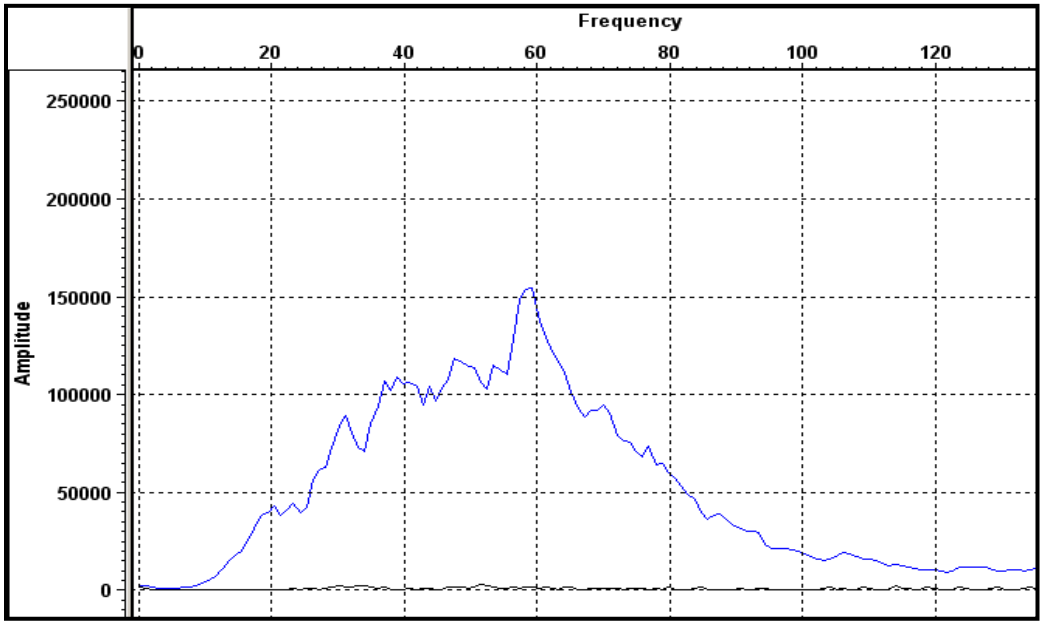

Fig. 1.3. Frequency spectrum of raw shot gather 59 from Meteor Crater seismic line.

In addition to the seismic data just described, ultrasonic measurements of several rock samples were also acquired in the field. The dominant frequency of the transducer was tested in the lab to be about 400 kHz. Assuming a near-surface velocity of 2000 m/s, the expected signal wavelength within the rock sample would be about 5 mm. Each rock sample was measured several times and the average velocity and standard deviation of

each sample was calculated. A list of the rock samples evaluated and their respective velocities is shown in Fig. 1.4 (R. Stewart, personal comm.). Note that the range of P-wave velocities of each formation varies considerably. This is likely due to differences in stratigraphy and distance from the crater rim of each hand sample.

Rock Formation	Range of P-wave velocity (m/s)
Moenkopi 1	815 ± 33
Moenkopi 2	1255 ± 106
Moenkopi 3	1570 ± 89
Kaibab 1	3705 ± 81
Kaibab 2	2560 ± 210

Fig. 1.4. Ultrasonic velocity measurement results of several hand samples from 2 rock formations at Meteor Crater.

The gravity and magnetic data were acquired at Meteor Crater in conjunction with the seismic data. A total of 79 unique gravity stations in the form of 5 lines and 72 unique magnetic stations in the form of 4 lines were acquired. The magnetic observations shared the same station locations as 4 of the gravity lines. The station spacing throughout the surveys remained constant at 30 m. For a complete overview of the seismic and potential field data acquisition parameters, the reader is referred to chapters 2 and 3, respectively. In addition, Tables 1 and 2 (Appendix C) include the raw gravity and magnetic data, respectively.

In addition, geodetic data in the form of light detection and ranging (LiDAR) data were included in this study to obtain accurate elevation data of the seismic line and the

gravity/magnetic stations. The data cover our survey area, namely the southern portion of the crater beyond the rim. The LiDAR data were processed to a spatial resolution of 25 cm and a vertical resolution of about 5 cm. For more details, the reader is referred to section 2.2.

Ground-penetrating Radar (GPR) and multi-component (3-C) hammer seismic data were also acquired at Meteor Crater. However, these data sets are beyond the scope of this project and are the foundation for other studies.

1.3.2. Pueblo of Jemez, New Mexico

The geophysical data at the Pueblo of Jemez were acquired in a similar fashion to Meteor Crater and were completed on May 22nd, 2010. The data consist of one 2-D seismic test line and a single gravity line. The 475 m single component 2-D near-surface seismic line was acquired for a period of 3 seconds with a sample rate of 0.5 ms, resulting in a Nyquist frequency of 1000 Hz and 6000 samples per trace. With a total of 86 shot gathers, each consisting of 72 traces, the total number of traces amounted to 6,192. Because the dominant frequency of the data is about 20 Hz (Fig. 1.5), which is lower than the Meteor Crater seismic data, the expected wavelength is about 100 m, which corresponds to a vertical resolution limit of 25 m (assuming a near-surface velocity of 2000 m/s, typical of the area). However, processing steps such as spiking deconvolution and band-pass filtering increased the vertical resolution of the seismic data.

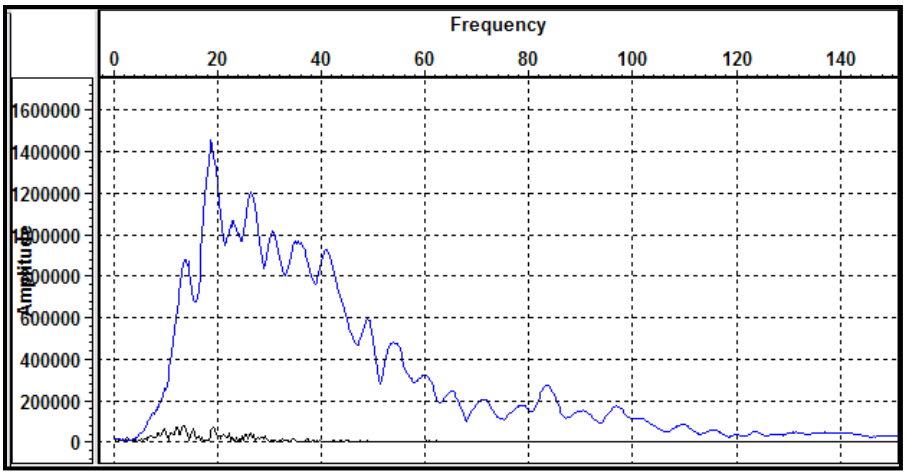

Fig. 1.5. Frequency spectrum of shot gather 51 from the Pueblo of Jemez seismic line. The dominant frequency is about 20 Hz.

The gravity survey acquired at the Pueblo of Jemez consists of 73 unique gravity stations with a constant spacing of 20 m along a crooked line, resulting in a length of 1440 m. The motivation in acquiring such a long line was to image the Indian Springs Fault Zone, a large known fault in the area. For an in-depth summary of the acquisition parameters, the reader is referred to chapter 4.

Unlike the Meteor Crater study, LiDAR data were not acquired at the Pueblo of Jemez. Since the topography along the seismic line was flat, elevation statics, and therefore elevation data, were not necessary in seismic processing. However, the topography along the gravity survey varied by as much as 15 m over the length of the line. To properly process the gravity data, elevations accurate to within several centimeters were necessary. Thus, spatial and elevation data were acquired using a handheld GPS device, accurate to within one meter spatially. Table 3 in Appendix C contains the raw gravity data acquired at the Pueblo of Jemez.

1.4 Overview

The bulk of this study is divided into 3 chapters, each dealing with a particular data set or area of study, as is outlined in the table of contents. The first data set, encompassing the Meteor Crater seismic study, is covered in chapter 2. The chapter outlines the study from beginning to end, namely acquisition, processing, and interpretation of the seismic data. Background information regarding the exact location of the study area, local geology, and elevation data concerning Meteor Crater are also covered in this section.

Chapter 3 deals with potential field data acquired at Meteor Crater. The chapter includes acquisition, processing, and interpretation of gravity and magnetic data at the study area. In addition, a joint interpretation of the potential field and seismic data is also included, where final conclusions regarding Meteor Crater are summarized.

The Jemez Pueblo geophysical study, comprising of seismic and gravity data, is covered in chapter 4. An overview of the study area and local geology is covered first. Then, seismic and gravity acquisition, processing, and interpretation portions of the study are described. Lastly, a joint interpretation of the area utilizing both geophysical methods is summarized.

In addition, a conclusion section and three Appendices (A, B, and C) are included at the end of the study. The conclusion reviews the study and highlights the most important results from this work. Possible future work at the study areas and recommendations are also included. Appendix A encompasses a geophysical study at

LaMarque, Texas, whereas Appendix B refers to a seismic study at the Energy research Park at the University of Houston in Houston, TX. Appendix C includes tables of raw gravity and magnetic data from Meteor Crater, AZ, and Jemez Pueblo, NM.

Chapter 2

Meteor Crater, AZ—Seismic Analysis

2.1 Introduction

2.1.1 Area of Study

Barringer Meteorite Crater (a.k.a. Meteor Crater) is an impact crater in northern central Arizona. It lies about 5 miles south of U.S. Interstate 40 between Flagstaff and Winslow, AZ. The crater, roughly 1.2 km across, was formed about 50,000 years ago by an iron asteroid whose relics are the Canyon Diablo meteorites, named after the canyon nearby (Kring, 2007). Because the crater is so well preserved (due to its young age and arid environment), it has been the site of great scientific interest since its discovery in the late 19th century.

2.1.2 Previous Investigations

Scientific inquiry into Meteor Crater dates back to the late 19th century (Foote, 1891). Debate about its origin began soon thereafter with competing views between then chief geologist at the United States Geological Survey, Grove Karl Gilbert (steam explosion), and Daniel Moreau Barringer (extraterrestrial impact). The debate raged for

many more decades until detailed studies by Shoemaker (1960) and Chao et al. (1960, 1962) concluded that the crater is of extraterrestrial origin.

Since then, numerous geological and geophysical studies were undertaken to better understand the complex structure. One of the first seismic studies at Meteor Crater was carried out by Ackermann et al. (1975), whose results from the seismic refraction technique were in agreement with results obtained through drilling (Shoemaker, 1963). Regan and Hinze (1975) completed the most comprehensive gravity and magnetic studies of the crater. Their results favor a symmetric bowl-shaped breccia lens beneath the crater floor and lack evidence of a meteoritic body, in agreement with Ackermann (1975) and Shoemaker (1963).

Work by Roddy et al. (1975) and Roddy (1978) focused on pre-impact geologic structure and mass-balance and energy calculations through an extensive rotary drilling program. The results have developed a more detailed understanding of the geologic structure of the crater and have been the basis for numerous scientific studies since then, including Pilon and Grieve (1991), Kumar and Kring (2008), and Poelchau et al. (2009), to name a few.

2.1.3 Geologic Setting

Meteor Crater lies roughly 1680 m above sea level in the southern portion of the Colorado Plateau (Kring, 2007). It is a simple bowl-shaped crater, which is characteristic of craters 2 km in diameter or less in sedimentary rocks (Pilkington and Grieve, 1992). It

has an average diameter of 1.2 km, is about 180 m deep from the crater rim to the floor (well below the surrounding plain), and rises 30-60 m above the surrounding flat erosional terrain (Kring, 2007).

There are roughly 1070 m of Paleozoic and Mesozoic sediments overlying the Pre-Cambrian crystalline basement rock in the vicinity of Meteor Crater; these are the same well-known sedimentary formations that are exposed at the Grand Canyon (Fig. 2.1). Nonetheless, only the four topmost formations are visible within the crater walls: the Coconino, Toroweap, Kaibab, and Moenkopi Formations. The topmost Moenkopi, consisting of the Moqui (fissile siltstone) and Wupatki (massive sandstone) Members, is most distinguishable because of its dark red color. Beneath the Moenkopi is the Kaibab, which consists of three members: Alpha, Beta, and Gamma. The Kaibab is a thick dolomite with inter-bedded white sandstone. Below the Kaibab is the Toroweap, a thin layer of sandstone and dolomite. Partially exposed at the bottom of the crater is the Coconino, a massive cross-bedded quartzose sandstone. The Coconino overlies the Supai, Naco, Molas, Redwall, and Martin Formations; although these remaining bottommost formations have not been excavated by the impact, evidence suggests that they have been extensively fractured (Ackermann et al., 1975). The stratigraphy of the target lithologies is explained in greater detail by Kring (2007).

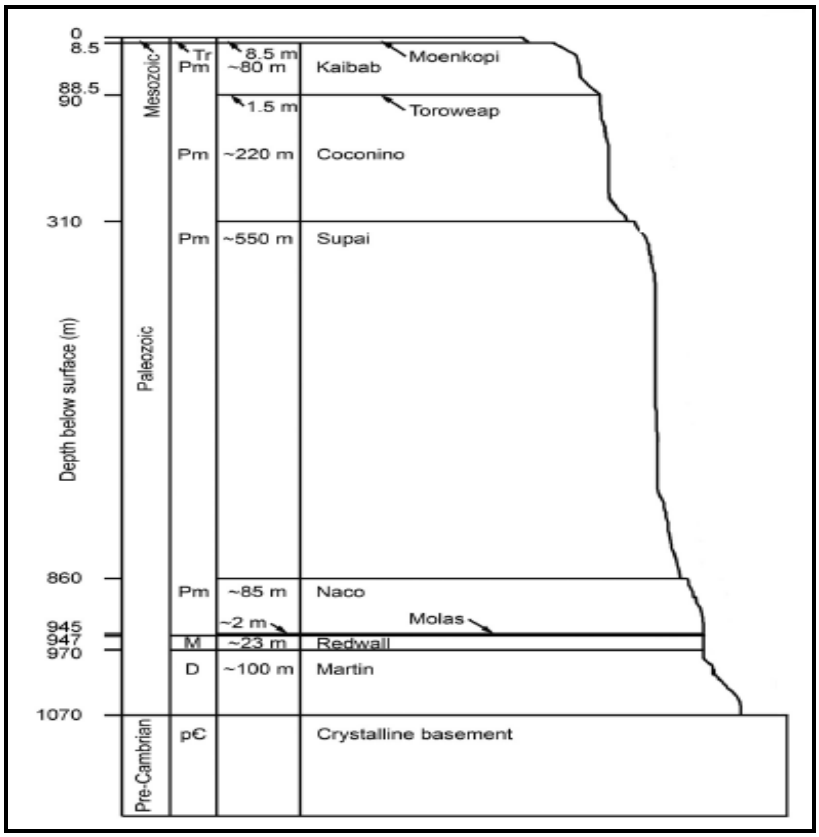

Fig. 2.1. Stratigraphy of target sediments and crystalline basement near Meteor Crater, properly scaled as a function of depth (Kring, 2007).

To understand the post-impact crater, pre-impact structural features must first be considered. Pre-impact topography of the area consisted of a flat terrain with a regional dip of about 0.5° to the northeast (Roddy, 1978). In addition, pre-impact structural features were similar to those seen today: impact occurred on a gentle monoclonal fold (Fig 2.2), NW-SE normal faults with offsets of a few meters to 30 m crosscut the target sediments, and two vertical joint sets extending for hundreds of meters to depths of about 100 m at orientations of 301-308° (NW-SE primary set) and 10-32° (NE-SW secondary set) also cross-cut the region (Fig. 2.3). It is these sets of joints, which are diagonal to the corners of the square crater, that Shoemaker (1960, 1987), Roddy (1978), and Poelchau et

al. (2009) attribute to the meteor's square-like shape in plan view. The hypothesis is that in the later stages of the cratering process, when induced stresses are on the same order of strength as the target lithologies, shear stresses exerted parallel to joints are less resolved than at a 45° angle to the joints, resulting in greater excavation towards the corners (Fig. 2.4).

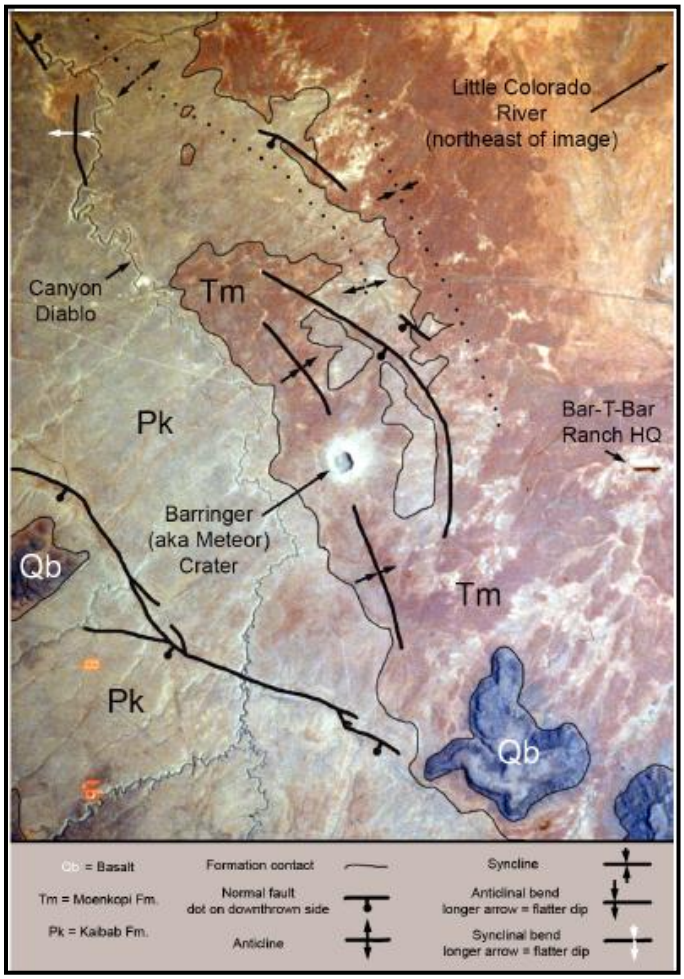

Fig. 2.2 Bedrock geologic map of area near Meteor Crater imprinted on an image taken from Space Shuttle Columbia (cropped image of #STS040-614-058). Moenkopi and Kaibab Formation contacts are approximate. Solid-line normal faults are mapped as seen in the image. Solid-line anticlines are consistent with the geologic map of Shoemaker (published in 1960). Anticlinal and synclinal bends are taken from Shoemaker (1960). Qb, Tm, and Pk refer to the contacts of the Quaternary basalt, Triassic Moenkopi, and Permian Kaibab formations, respectively (Kring, 2007).

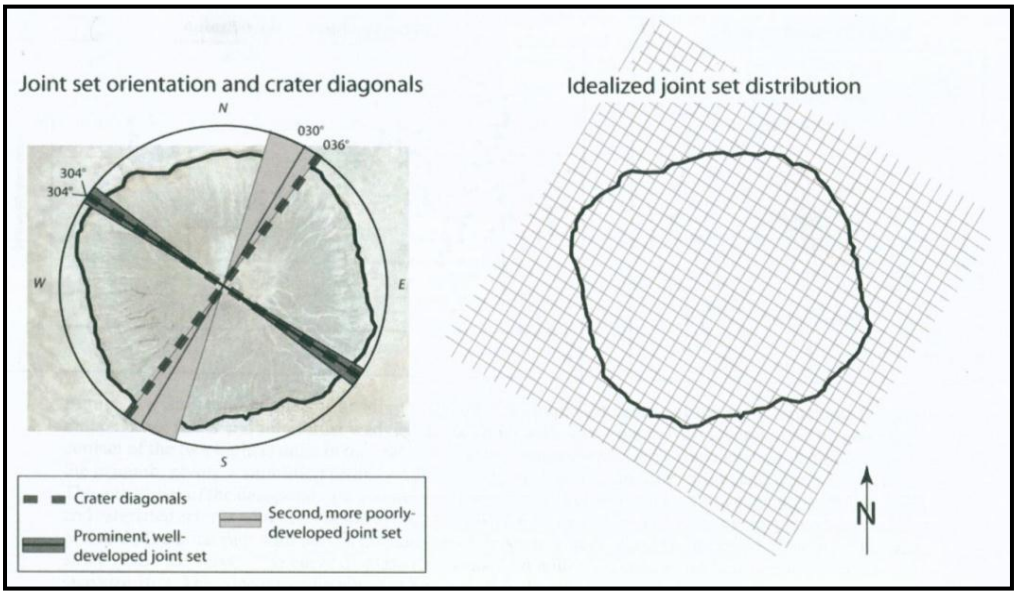

Fig. 2.3. Field data of joint set orientations (30 and 304) from Roddy (1978) correlate well with azimuths of crater diagonals (36 and 304). The joints have a spacing of 0.5 to 10 m and subdivide the crater into smaller square units (Poelchau et al., 2009).

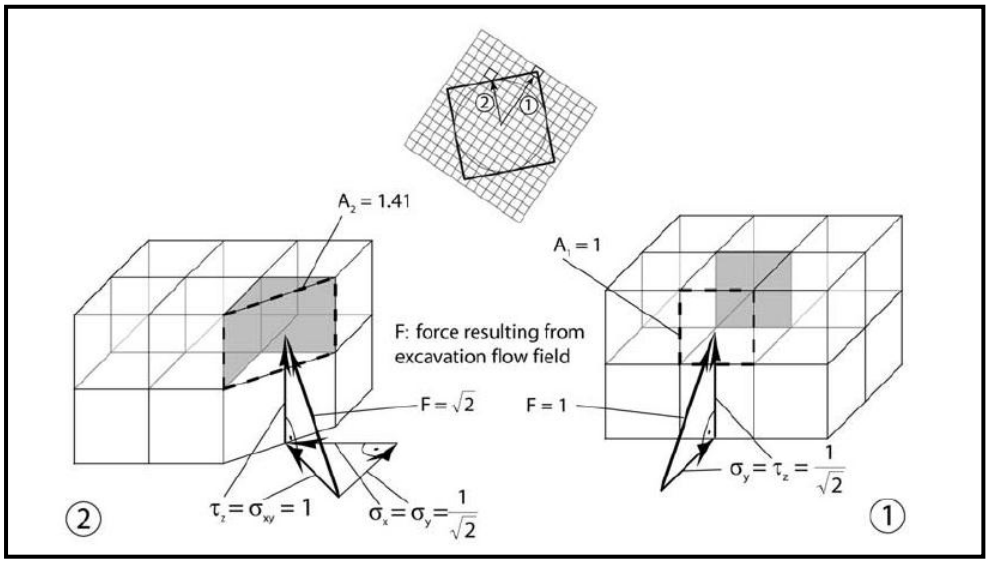

Fig. 2.4. Models show force needed to excavate blocks parallel (1) and at 45° (2) to joint sets. The force necessary to excavate the block in situation 2 is √2 times greater than in situation 1. Thus, crater excavation is more effective in situation 1, which forms a square-shaped crater (Poelchau et al., 2009).

In addition to joint sets, “radial corner faults” run vertically through the crater corners, which are thought to be the result of the reactivation of these joints at the time of the impact (Poelchau et al., 2009). These faults are characterized by vertical displacement with a rotational component, resulting in greatest rim uplift in the corners of the crater (Poelchau et al., 2009). The reactivation of these joints into faults is important in this study: if these joint sets reactivated into faults throughout the vicinity of the crater, then they will be easier to resolve and interpret with geophysical methods.

2.2 Topography/LiDAR

Spatial data were acquired in the field via a handheld GPS receiver along the seismic line at each of the gravity stations. The GPS’s latitude and longitude readings were accurate to within a foot; elevations to within a few meters. The poor elevation accuracy was due in large part to a lack of experience and knowledge in operating the GPS device. To obtain more accurate elevations, light detection and ranging (LiDAR) data were utilized to create a digital elevation model (DEM). The data were acquired over the entire crater as well as most of the ejecta blanket surrounding the crater. However, because this study is only concerned with the southern portion of the crater beyond the rim, only that portion of the data was used (Fig. 2.5).

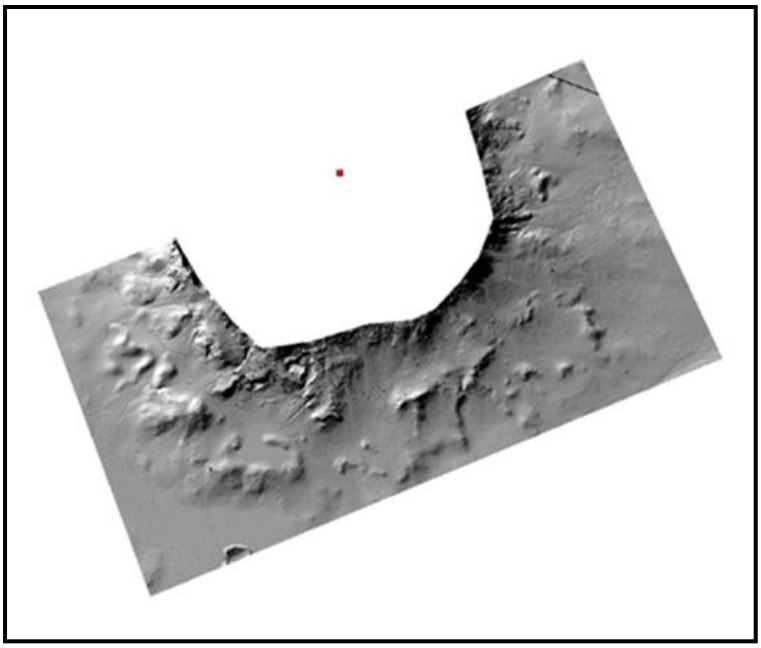

Fig. 2.5. Grayscale image of shaded LiDAR data showing southern portion of ejecta blanket at Meteor Crater. The red dot represents center of crater (longitude 111°01'19" W and latitude 35°01'40" N).

The LiDAR data, acquired by airplane over the crater by the National Center for Airborne Laser Mapping (NCALM), have a horizontal resolution of 25 cm and a vertical resolution of about 5 cm—accurate enough for the geophysical purposes of this study. The data are divided into squares 25 cm on a side; the elevation of each square is then averaged and is assigned that corresponding value.

The extent of the DEM includes all of the gravity stations, yet does not extend to the end of the seismic line. This lack of elevations was solved by fitting a 2^{nd} order polynomial to the last 100 meters of the LiDAR data set and extrapolating the results to the remainder of the seismic line. Although not perfect, the solution is valid for seismic purposes since the terrain far from the crater flattens considerably and variations of only a few meters have a negligible effect on the final result. Fig. 2.6 shows the extent of the

DEM along the length of the seismic line (red). Also included in the figure are the locations of the drill holes used in creating the geologic cross section of the South Line in Roddy et al. (1975), shown as yellow stars, and the location of the 1,376' drill hole (green square), which was drilled in 1922. The distance from the 1,376' drill hole to the beginning of the seismic line is 76 m (map scale is 1:4,000). Fig. 2.7 shows the elevation vs. distance plot of the seismic survey. As expected, the change in elevation is greatest near the beginning of the seismic line (near the crater rim) and is least towards the end (about 700 meters from the crater rim).

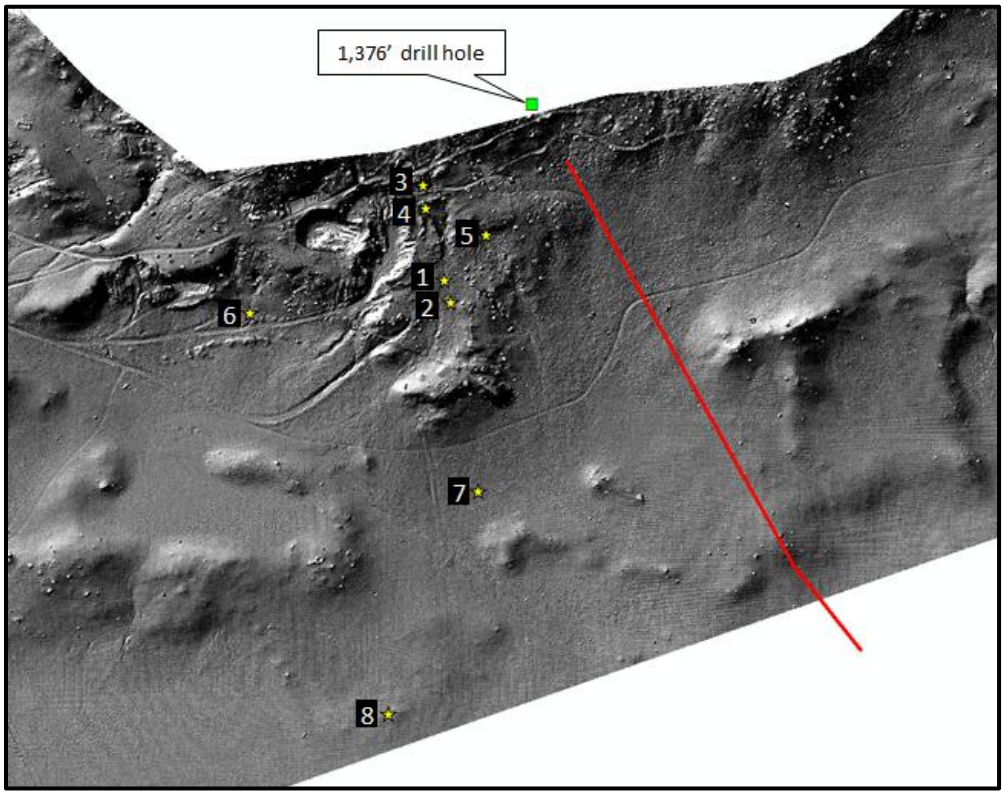

Fig. 2.6. Image of shaded LiDAR data of southern portion of ejecta blanket at Meteor Crater. Red line represents seismic survey (AWD line). Yellow stars represent locations of drill holes used in creating the South Line geologic cross section in Roddy et al. (1975). Green square is location of 1,376' drill hole, which is 75.5 m from the start of the AWD line.

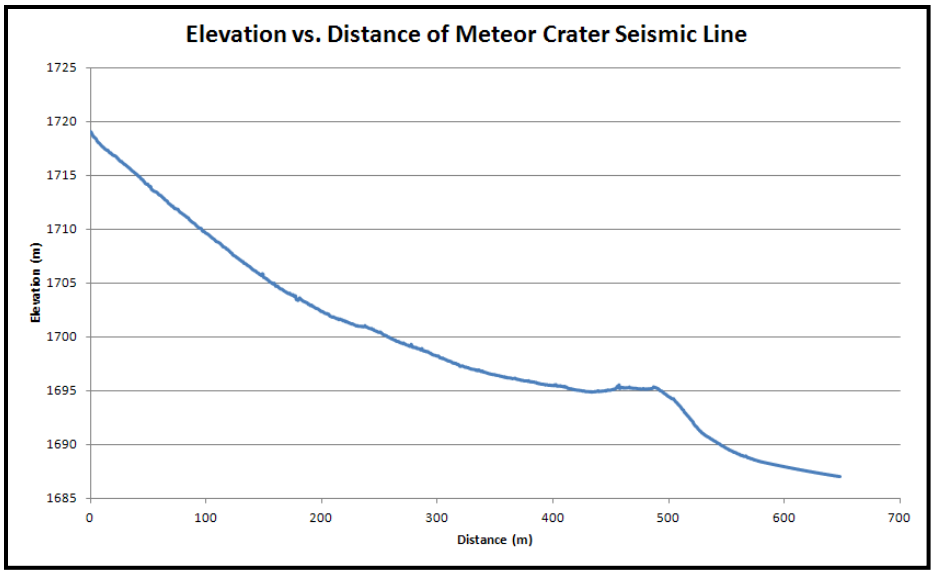

Fig. 2.7. Elevation vs. distance graph of Meteor Crater seismic line using LiDAR data.

2.3 Synthetic Modeling

Utilizing knowledge of the crater's subsurface from previous studies (Kring, 2007), a simple model was first created to estimate the expected seismic signal. The model, shown in Fig. 2.8, consists of 5 formations with varying P-wave velocities and densities, as depicted. The Toroweap is not included in this model because of its similar acoustic properties to the Coconino and its relatively insignificant thickness—it is not expected to be resolved by seismic data. Average values for the lithologic properties were obtained from a geophysical study of the crater by Roddy (1978). Only 5 layers were created within the model (reaching a depth of about 500 m below the surface) because the weight-drop source was not expected to propagate sufficient reflective energy beyond this depth and the deeper formations are not thought to be affected by the impact.

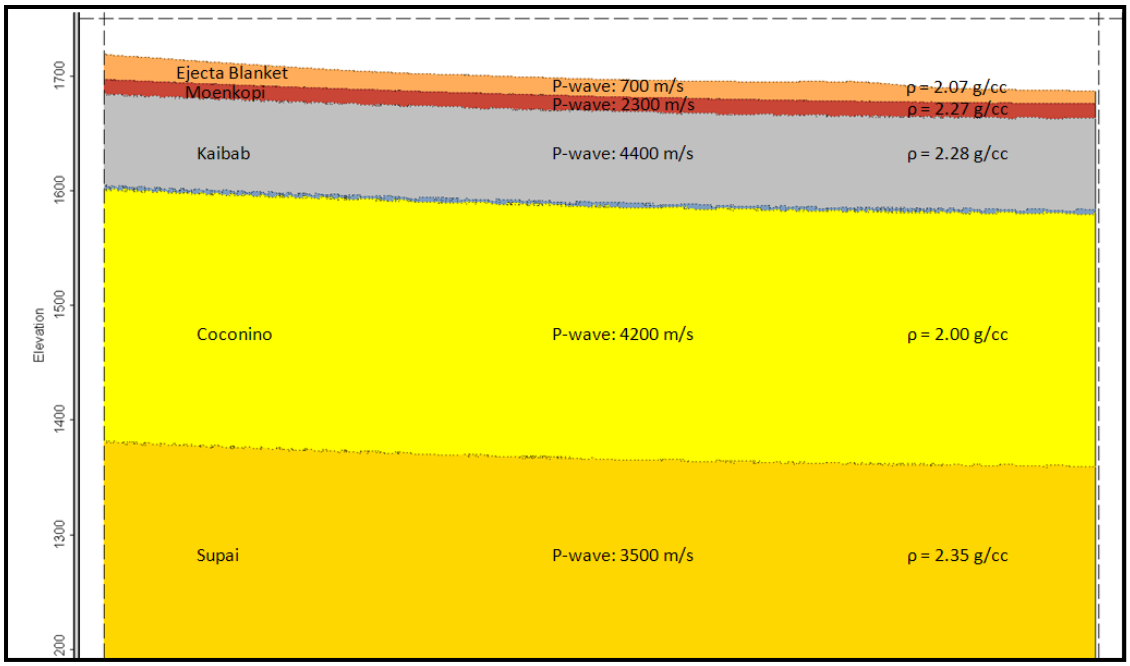

Fig. 2.8. A simple 2-D model of subsurface surrounding Meteor Crater.

A ray tracing simulation was then performed on the model to gain a sense of the reflection hyperbolae from the various reflectors and to estimate their time of arrival (Fig. 2.9). It is worth noting that the reflection hyperbola of the ejecta blanket/Moenkopi interface (red) is at a steep angle, indicating a long two-way propagation time from the source to the receiver. This is a result of the low velocity of the ejecta blanket above the Moenkopi. This sharp increase in velocity from the ejecta layer to the Moenkopi formation creates an imaging problem: far offset reflections from this contact can only be imaged by removing the deeper reflections via NMO correction. Miller and Xia (1998) propose segregation of shallow lower velocity reflections from higher velocity reflections during processing to maximize accuracy and resolution potential. Also, such a large change in velocity results in post-critical reflections at a small angle of incidence (Diogo et al., 2004). Indeed, a simple AVO model of the interface shows that the critical angle is

reached at about 18° (Fig. 2.10). Thus, imaging such shallow reflectors is a formidable task.

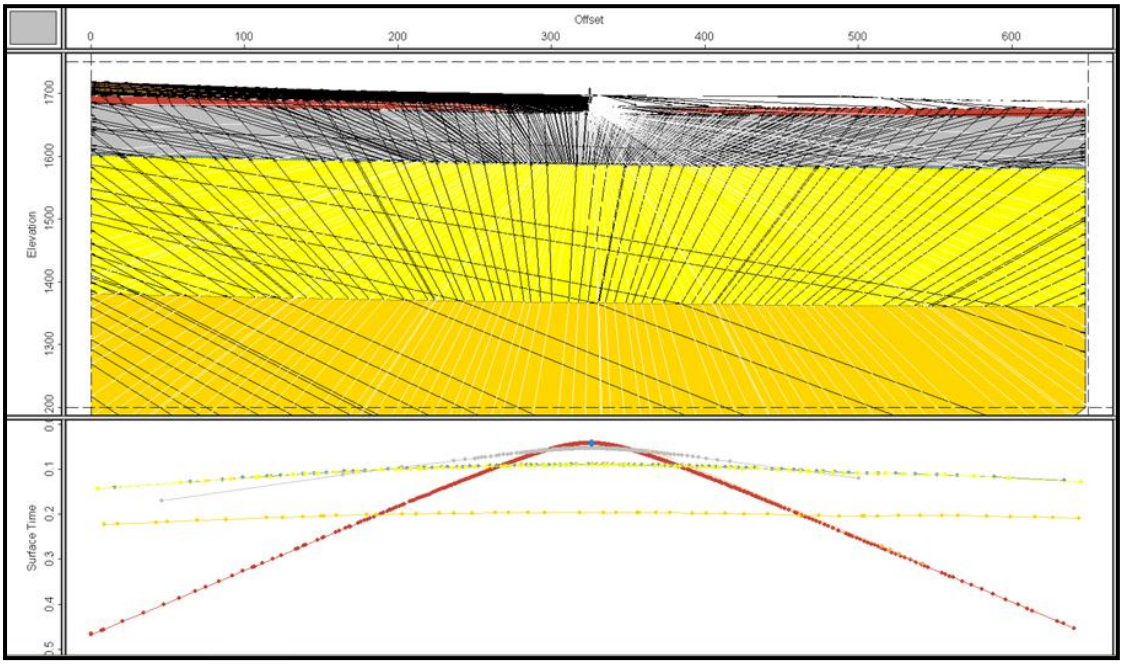

Fig. 2.9. Ray tracing results from 2-D model shown in Fig. 2.8.

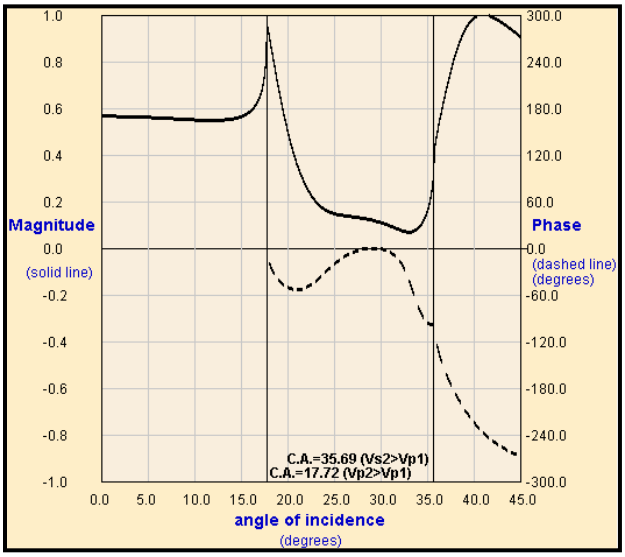

Fig. 2.10. An AVO reflectivity model of the expected ejecta blanket/Moenkopi contact using the property values shown in Fig. 2.8. The critical angle is 17.72°. Created using the Zoeppritz-Black equation of the CREWES Reflectivity Explorer 2.1.

In addition, a depth-to-time conversion of the 2-D model was performed to simulate what a final stacked seismic time section may look like (Fig. 2.11). The information gleaned from these models indicates that the reflections of interest are expected to be recorded no later than 300 ms, the majority of which are to be recorded before 150 ms. Although the modeling results are insightful, they are only meant to be a guide: the actual results will vary greatly because of structural inaccuracies of the model, noise contamination, etc.

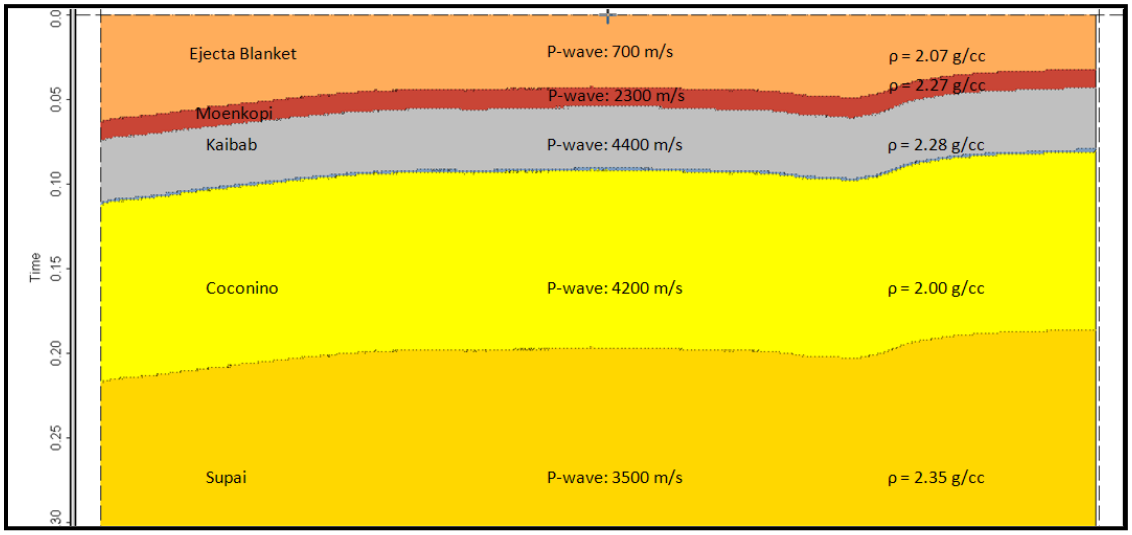

Fig. 2.11. Depth-to-time conversion of 2-D model shown in Fig. 2.8.

2.4 Acquisition

The main focus of this study is a 660 m 2-D single component seismic line that begins near the southern crater rim and extends in a SSE direction across the ejecta blanket (Fig. 2.12). The line consists of 216 field stations with a spacing of 3 m. Since there were only 120 geophones available, the line was rolled twice with 48 receivers being taken from the start of the line and placed at the end each time; the rolling thus

resulted in a 645 m receiver line. In addition, several 3-C seismic lines were acquired using a hammer source and twenty 3-C receivers on a land streamer to investigate the ejecta layer; work on these 3-C data sets has already begun and preliminary results have been published (Roy et al., 2010).

Fig. 2.12. Satellite image of Meteor Crater using Google Earth. SSE red line extending from the crater rim represents the survey of the 645 m seismic receiver line.

The main SSE seismic line was acquired with 3 shots at each location, which were stacked automatically in the field. The shots, or accelerated weight drops from the back of a pick-up truck, were placed halfway between each pair of geophones and about 1 m to one side of the entire line. This type of geometry yielded a shot spacing of 3m. Because of several initial bad shots, the first recorded shot location was between receiver stations 2 and 3 (i.e. 4.5 m) and the last off-end shot was located at 676.5 m, which

marked the end of the seismic line. This geometry yielded 214 split-spread shots and another 10 off-end shots at the end of the line. In addition, several shots had repeated shot locations, increasing the total number of shots to 230. The total length of the final seismic image resulted in a 660 m line. The geometry of the entire line is shown in Fig. 2.13.

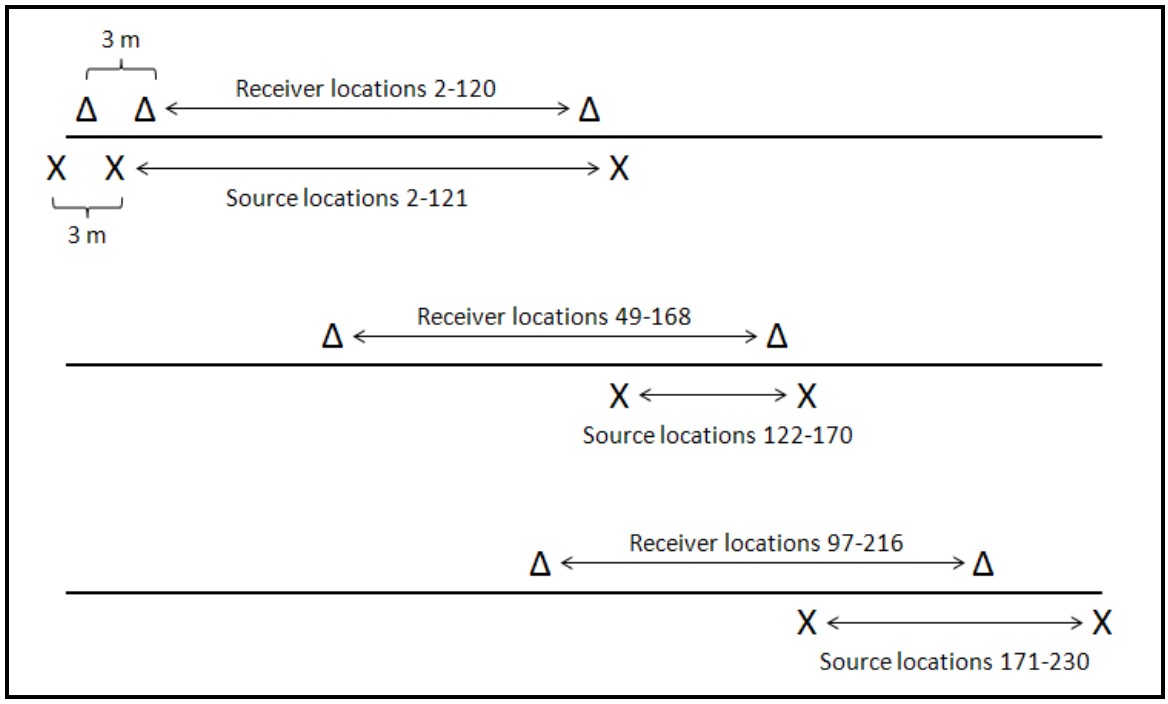

Fig. 2.13. Geometry of the Meteor Crater seismic survey. Three separate lines are shown to emphasize how the line was rolled twice during acquisition. Both source and receiver spacing remained constant at 3 m.

2.5 Processing

To make the raw seismic data reflect the structure of the subsurface, a processing workflow was established (Fig. 2.14). These data processing techniques differ from most hydrocarbon exploration-scale seismic processing methods because the targets of interest

vary considerably. Near-surface seismic reflection methods are often interested in the topmost 500 ms or less, whereas exploration-scale seismic data are usually concerned with 3-4 seconds of data or more (Baker et al., 1998). The processing workflow in Fig. 2.14 is a modification of several other near-surface processing workflows that have been successful in imaging the shallow subsurface (Baker, 1999; Kaiser et al., 2009). This particular workflow focuses much energy on attenuating noise; in particular, ground roll due to a thick unconsolidated ejecta blanket. To process the data, two different processing software packages were utilized: Gedco's Vista and Paradigm Geophysical's Focus software.

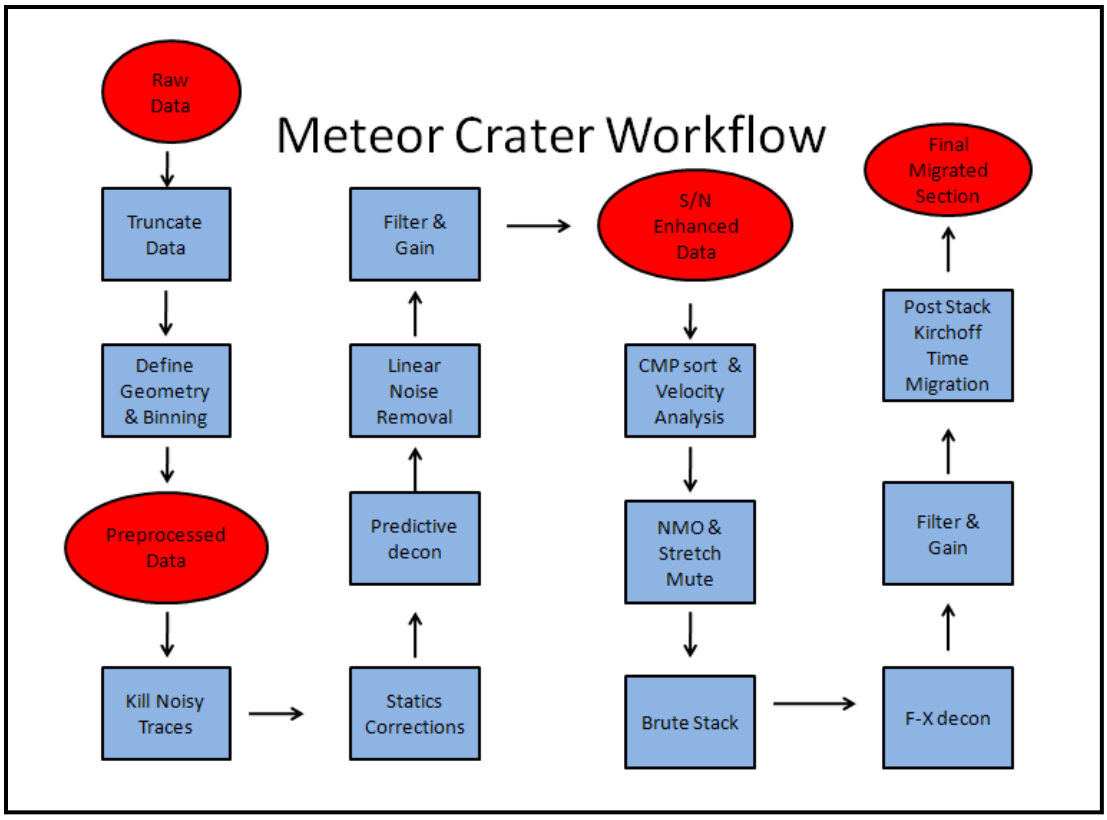

Fig. 2.14. Seismic processing workflow applied to Meteor Crater seismic data.

The initial step in the processing workflow was to input and truncate any unused data. Although data in the field were gathered for 3 seconds, the object of the survey was to characterize the near-surface. Thus, data beyond 1000 ms were truncated. Fig. 2.15 shows shot gather 61 before and after data truncation. The main purpose of removing the tail-end of the data was to decrease the computing time of later processing steps and to divert the processor's attention away from extraneous data since reflective energy from a weight drop is not expected to be recorded beyond that time.

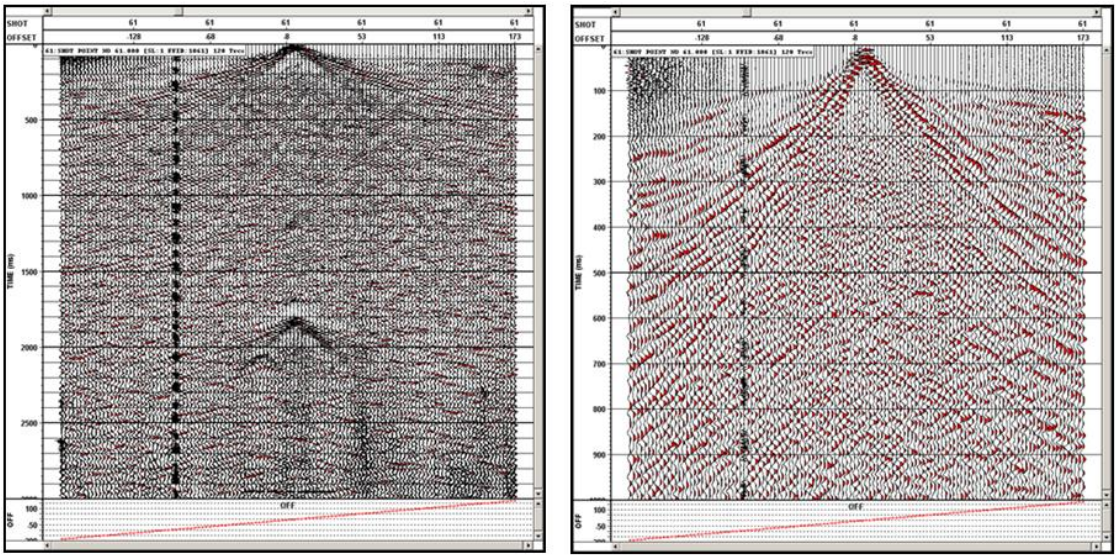

Fig. 2.15. Raw shot gather 61 before data truncation (left) and after truncating data to 1 second (right). An AGC window of 200 ms was applied to both shot gathers.

Next, the source and receiver geometries of the survey were defined according to the acquisition parameters mentioned in section 2.4 (Fig. 2.16). This step required complex header manipulation because a portion of the receiver line was rolled twice during acquisition. In addition, the variable topography along the line necessitated the

inclusion of elevations at each shot and receiver location, which were input at this time from LiDAR data gathered prior to this study.

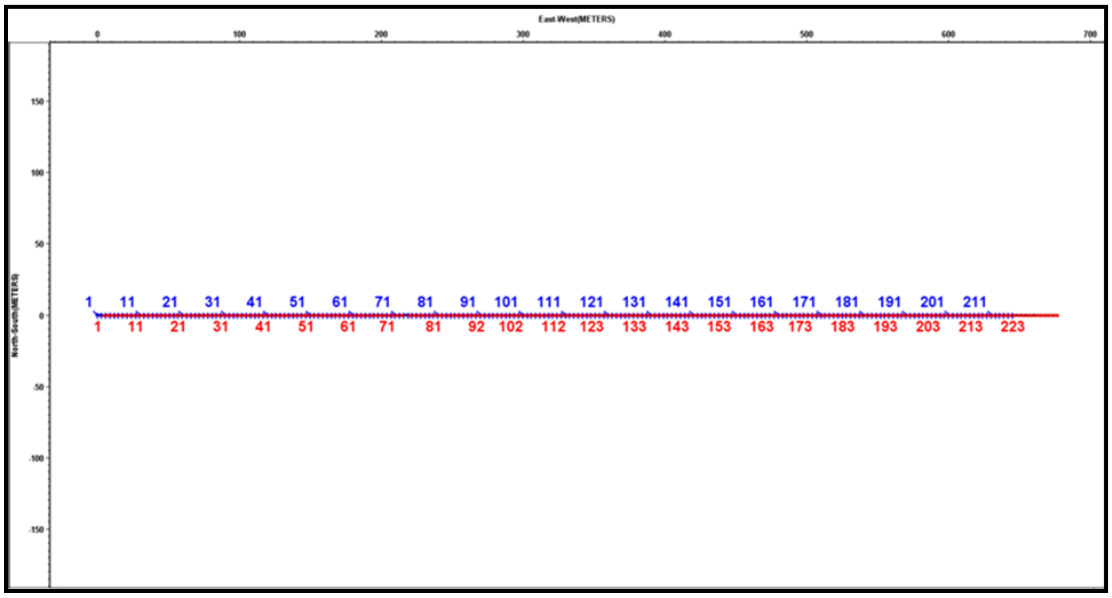

Fig. 2.16. Source and receiver geometry of the seismic line at Meteor Crater. Red squares and blue crosses represent shot and receiver locations, respectively.

Common mid-point (CMP) bins were then created along the line to sort the data by CMP in later processing steps. The geometry of the line resulted in CMP bins of 1.5 meters. The CMP fold of the line was calculated based on the acquisition parameters (Fig. 2.17). The CMP fold is non-uniform because all of the geophones were live during each shot and the shooting scheme was a combination of both off-end and split-spread shots. In addition, the line was rolled twice, which further complicated the sub-surface CMP fold results.

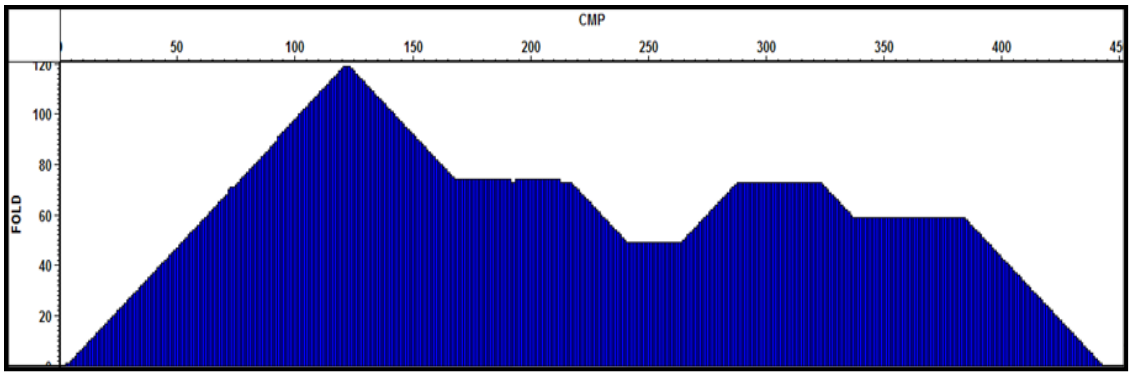

Fig. 2.17. Subsurface CMP fold of entire Meteor Crater seismic line. Maximum fold is 119.

A first examination of the raw data was conducted to identify major features and check the quality of the data. Fig. 2.18 shows the results of this examination from shot gather 61. From this first pass, it was evident that the airwave and ground roll would pose a challenge in imaging the subsurface because their high amplitude and low velocities mask most of the signal of interest. Fig. 2.18 also shows the refractions and possible reflections within the shot gather. The area where most reflections within this survey are expected to be properly imaged is called the optimum window (Hunter et al., 1984). This area is known as such because it is an area of minimal interference from ground roll on the near offsets and from refractions on the far offsets. Thus, it is bounded by refractions at the far offsets and by the noise cone at the near offsets. Although the optimum window is an area where most reflections can be seen, valuable reflection data also exist within the noise cone, which is why noise attenuation is so important in the processing efforts of this data set.

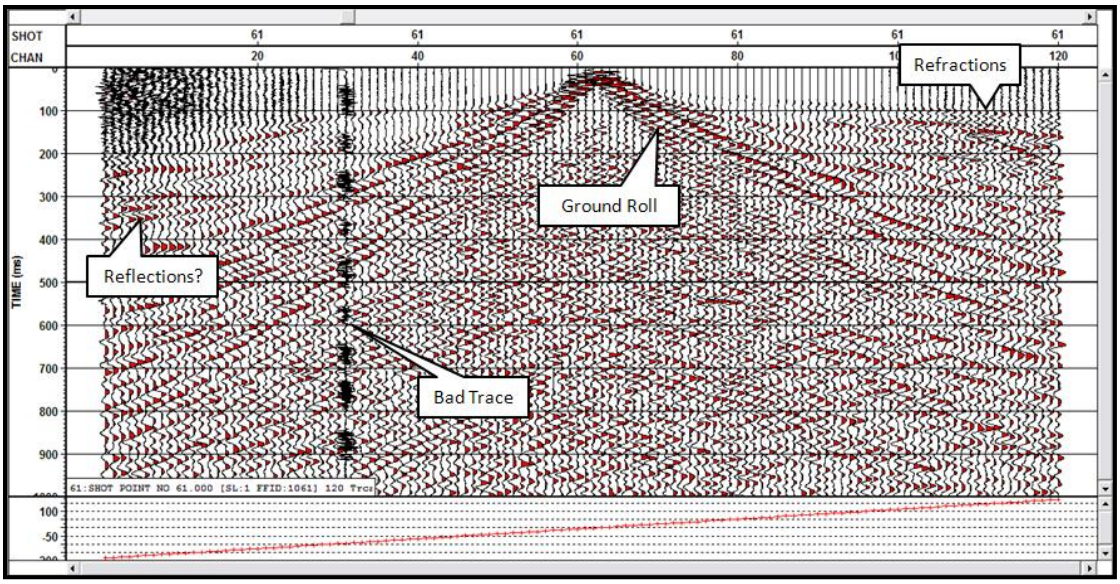

Fig. 2.18. Truncated raw seismic shot gather 61 with a 200 ms AGC window applied. Major features are indicated by call-out symbols.

Although possible reflections in the near surface have been identified in Fig. 2.18, it is not clear whether they are reflections or refractions. Properly separating the reflections from the refractions will be a difficult step in creating an image of the subsurface. The data were also passed through numerous band-pass filters in an attempt to identify and separate desired signals from noise based upon their frequency spectra. Fig. 2.19 shows several of these filter and gain applications. It is clear from the figure that desired reflections within the optimum window contain frequencies similar to data residing in the noise cone. Hence a simple band-pass filter will not suffice in separating ground roll from reflections. A more precise spectral analysis of the data indicates that the reflected signals lie in the 20-120 Hz band, or in the typical seismic frequency bandwidth.

A.

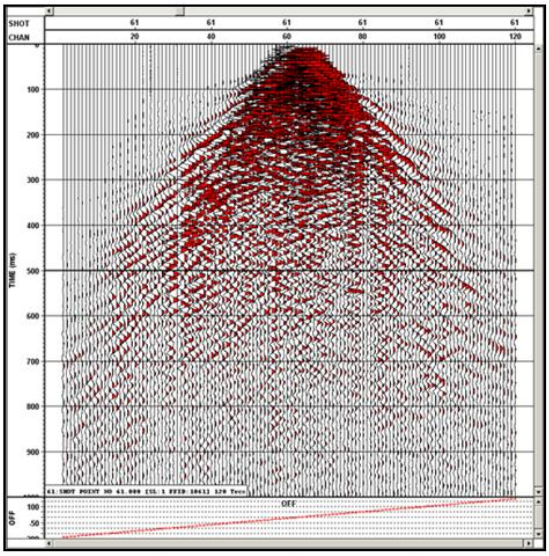
SHOT
CHAN
TIME (ms)
OFF

B.

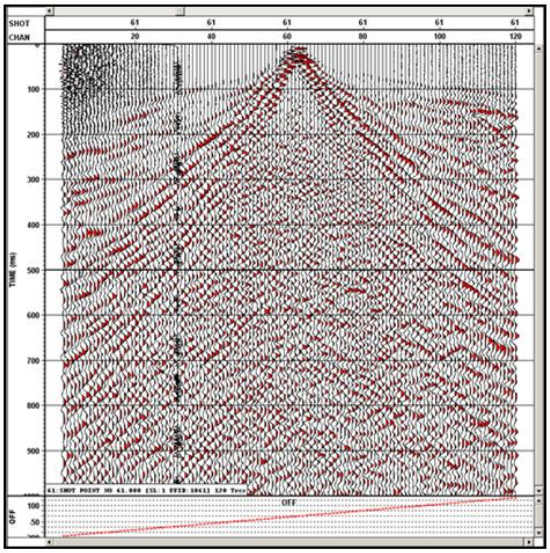
SHOT
CHAN
TIME (ms)
OFF

C.

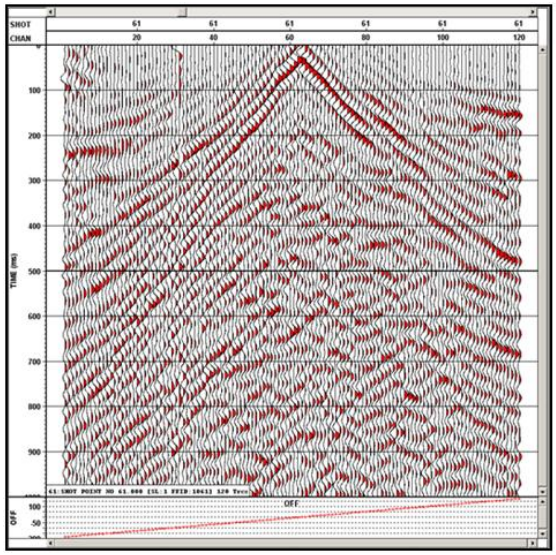
SHOT
CHAN
TIME (ms)
OFF

D.

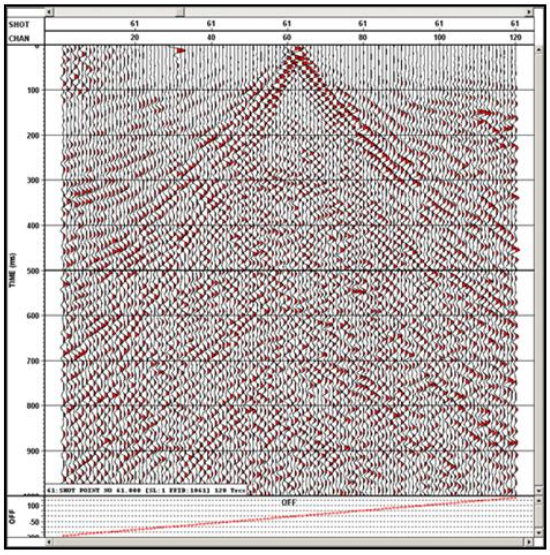
SHOT
CHAN
TIME (ms)
OFF

E. F.

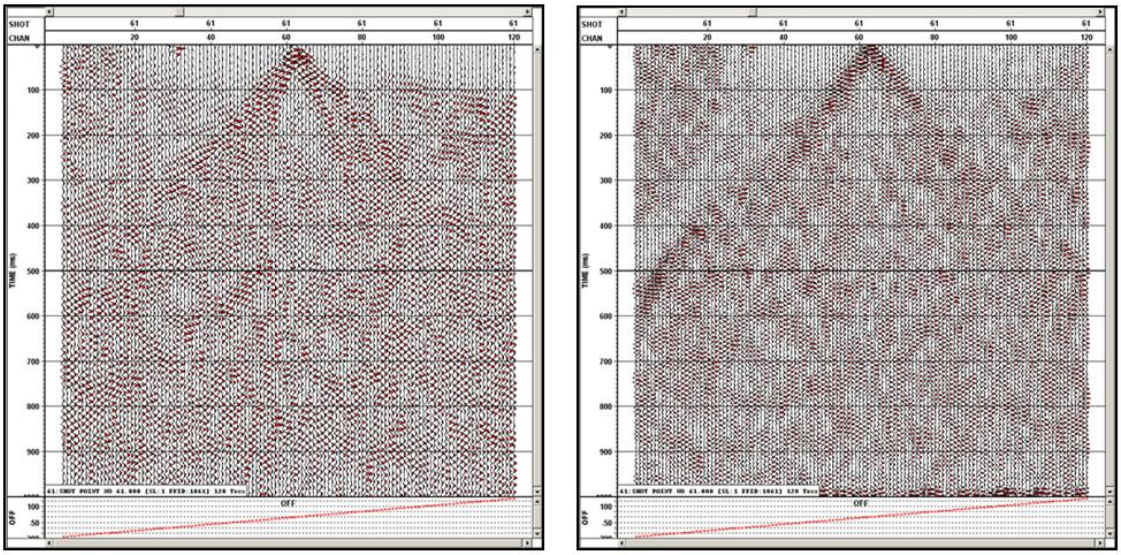

Fig. 2.19. Shot gather 38 with several filters and gains applied to the Meteor Crater seismic data. A is a raw shot gather. B is the same shot gather with a 200 ms AGC window applied. The remaining windows have the same AGC windows applied with varying band-pass filters: 0-30 Hz, 30-60 Hz, 60-90 Hz, and 90-120 Hz for C, D, E, and F, respectively.

The next step in the workflow involved killing all noisy traces that could contaminate a stacked section with spiked amplitude data. This step served to improve the signal-to-noise ratio (S/N) of the data and ultimately produce a clearer image of the reflections. Because of broken geophones, windy conditions, and human activity along the receiver line during acquisition, great care was taken in removing all noisy traces. Fig. 2.20 is an example of a shot gather containing numerous noisy traces that were removed.

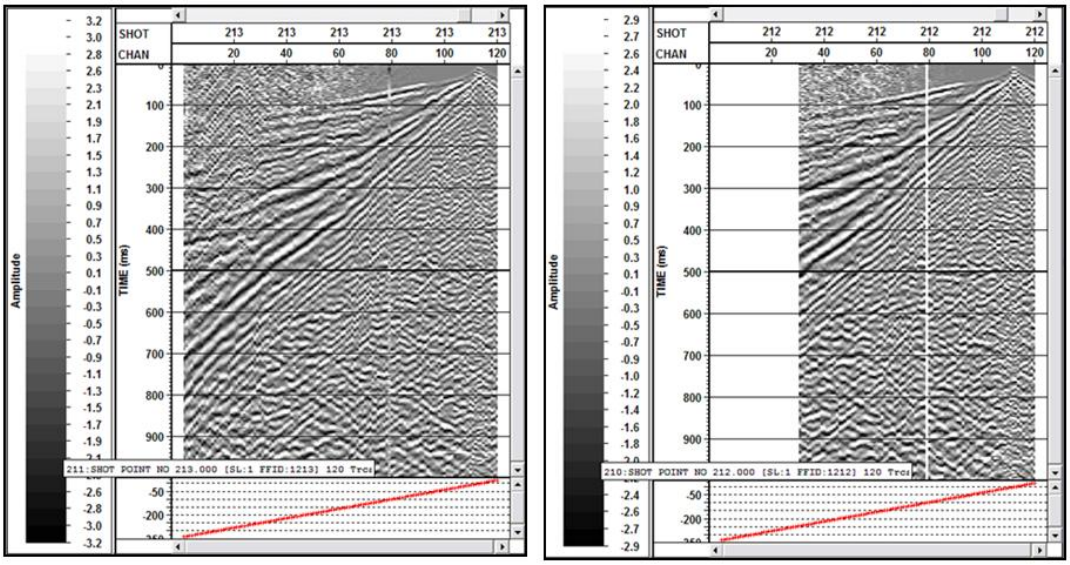

Fig. 2.20. Shot gather 213 with a 100 ms AGC window applied (left). Same shot gather with noisy traces removed (right).

Next, elevation and refraction statics were calculated and applied to the data to compensate for changes in topography and ejecta layer heterogeneities throughout the seismic line. To accomplish this goal, a refraction analysis of the first breaks was completed. The first step involved picking the first breaks within each shot gather. Because the data were so noisy, the process was carried out manually. Fig. 2.21 shows shot gather 130 with first break picks shown in green and an inset of the time-distance plot of these picks. It is evident from Fig. 2.21 that 2 layers are imaged by the refractions: an upper low-velocity unconsolidated ejecta layer (including a thin veneer of recent eolian sand at the surface) and a higher-velocity consolidated layer beneath (most likely Moenkopi or overturned sequence).

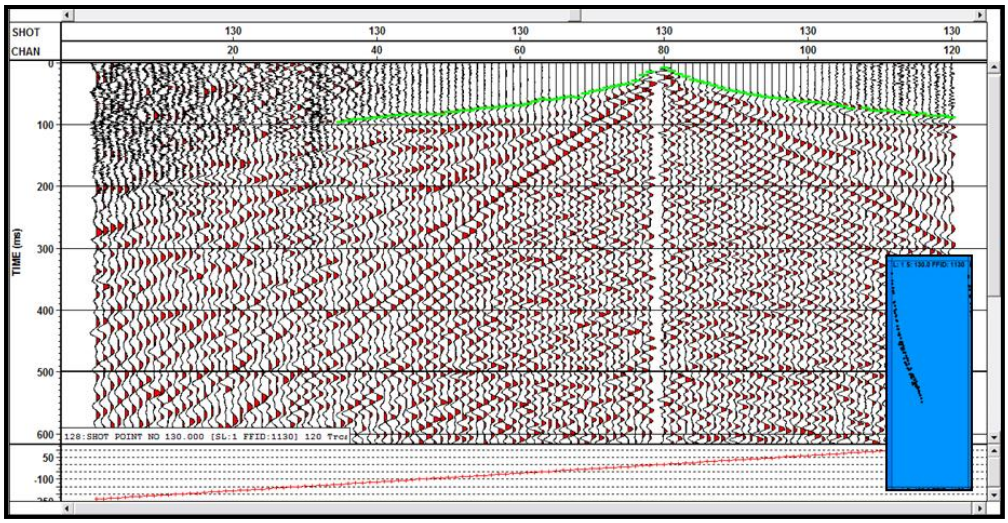

Fig. 2.21. Shot gather 130 with a 100 ms AGC window applied. Green dashes indicate first break picks. Blue inset is a time-distance plot of first-break picks (distance is x-axis; time is y-axis).

Using these first breaks, a two layer model was constructed in Vista (Fig. 2.22). The model consists of an upper unconsolidated layer (ejecta blanket) and a lower consolidated layer. The ejecta layer has a variable velocity ranging from 375 m/s to about 650 m/s. The lower layer shows a varying velocity structure, increasing from 1500 m/s near the crater rim to roughly 2500 m/s farthest from the crater. This velocity profile is expected: slower velocities near the fractured and brecciated crater rim and faster velocities as you move away, where the rock is less affected by the shock of the impact. Due to software limitations, a constant velocity of 2000 m/s was used as the replacement velocity for refraction statics based upon this analysis. In addition to velocity changes, the refraction analysis shows a variable thickness of the ejecta blanket, adding to the complexity of the subsurface.

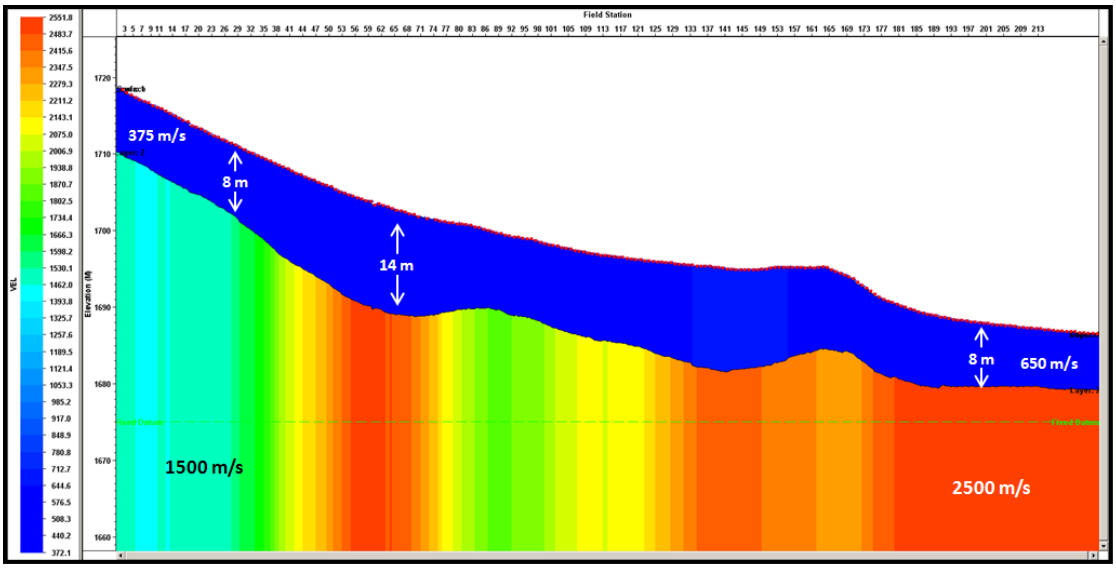

Fig. 2.22. A 2 layer model of the very near-surface based upon refraction data analysis. Velocities and thicknesses are shown at various locations.

Assuming that the higher-velocity refractions result from the Moenkopi bedrock, drill-hole data in the area are not in total agreement with Fig. 2.22 (Roddy et al., 1975). Drill-hole data indicate a 20 m thick ejecta blanket on top of the Moenkopi near the beginning of the seismic line, which tends to thin with radial distance. The approximate depths of the Moenkopi and Kaibab formations along the south line drill hole data from Roddy et al. (1975) are shown via dashed lines in Fig. 2.24. This disparity may be due to a thicker ejecta blanket close to the rim that includes overturned Kaibab and Moenkopi formations. However, the refractions could also be the result of a more competent breccia above the Moenkopi bedrock. More ground truth drill-hole data are needed to solve this problem.

Evidence for such possible lithologic/structural change in the near-surface resides in the refractions themselves. A close inspection of the first break picks within shot

gather 72 shows a structural anomaly near field station 60 (Fig. 2.23). This type of seismic response is typical of diffractions resulting from faulting in the subsurface (Cox, 1999). Several other such diffraction-like anomalies are evident throughout the seismic line, which may be indicative of highly faulted bedrock underlying the ejecta.

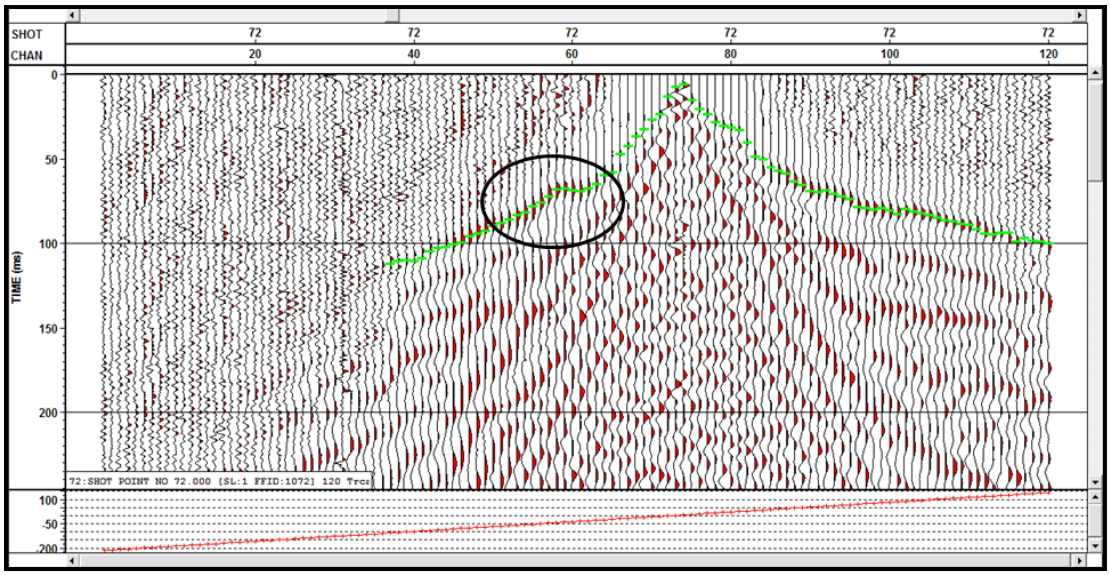

Fig. 2.23. Shot gather 72 with a 50 ms AGC window applied. Green dashes indicate first break picks along the refraction and black circle shows location of a diffraction-like anomaly.

Since the Vista software is intended mainly for processing reflection seismic data, and therefore limited in refraction data analysis, Geometrics' Plotrefa software was used to create a more robust image of the very-near-surface (roughly 60 m) based on first-arrival refractions. The latest results of the tomographic inversion method are shown in Fig. 2.24 (S. Roy, personal comm.). Approximate depths of the Moenkopi and Kaibab formations from drill hole data of the south line by Roddy et al. (1975) are overlaid on the image and are shown in Fig. 2.25. The locations of these drill holes are shown in Fig. 2.6. Because these drill holes are sparse and about 100 m to the west of the seismic line,

they may not accurately represent the subsurface along the study area and are therefore only used as a guide. However, the southeast line drill hole data from Roddy et al. (1975) show a similar trend in the subsurface, implying that the depths of the formation tops are fairly uniform in the area. The results in Fig. 2.24 clearly show a lateral increase in the velocity of the subsurface away from the crater, especially at 250 m. However, the velocity profile does not correspond to the variable ejecta blanket thickness, as was expected. Hence, the velocity gradient may be controlled by other factors such as fracture density or porosity (i.e. bedrock brecciation decreases with distance from the crater rim). The velocity profile may aid in the interpretation of the gravity survey through known velocity-density relationships such as the Gardner equation (Gardner et al., 1974).

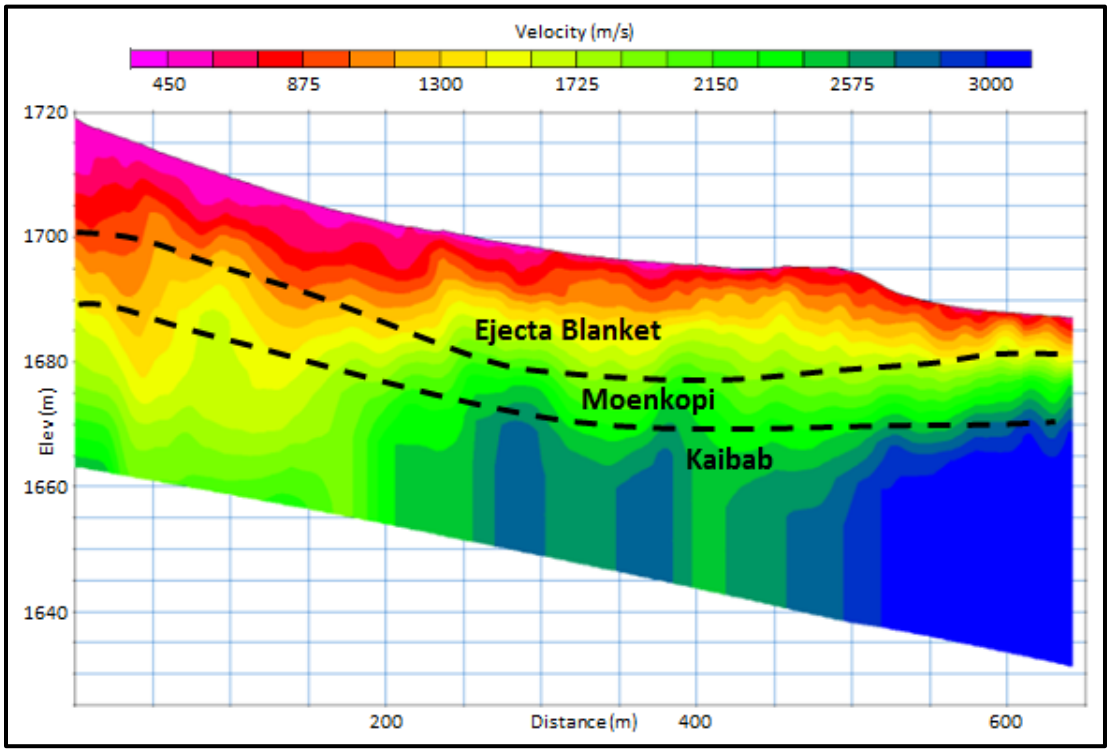

Fig. 2.24. Results obtained from tomographic inversion of the P-wave first-break picks (S. Roy, personal comm.). Approximate depths of the Moenkopi and Kaibab formations from the south line drill hole data by Roddy et al. (1975) are overlaid (dashed line).

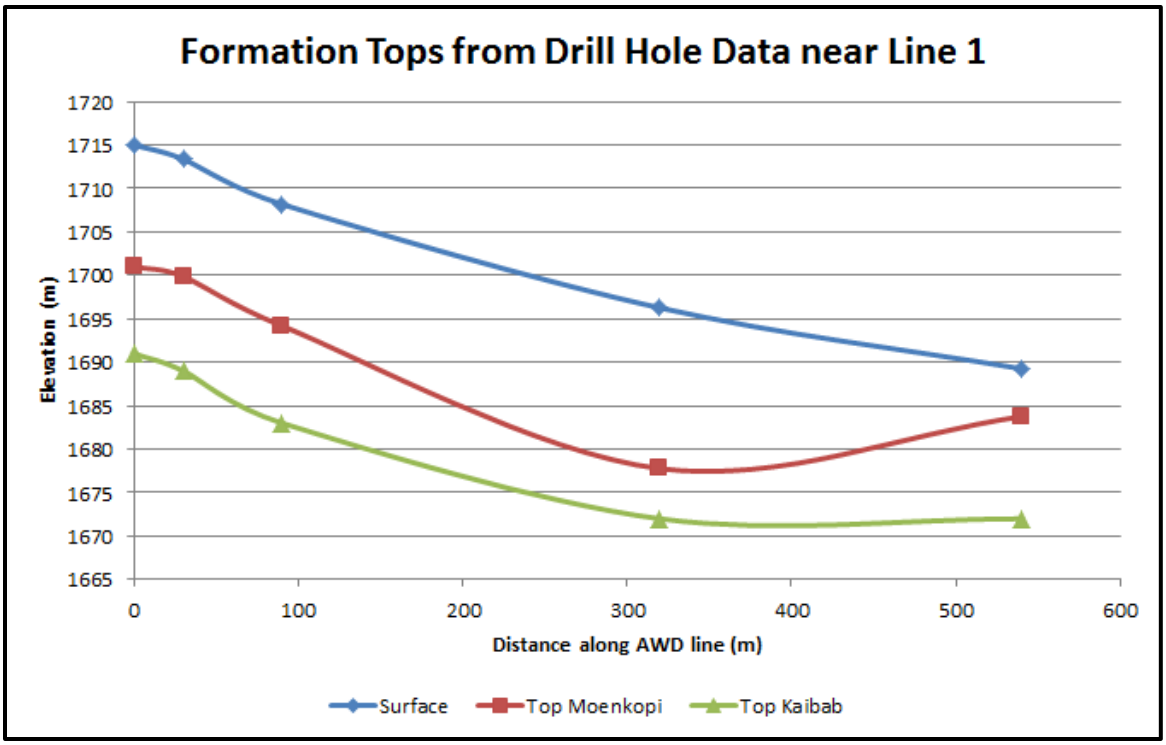

Fig. 2.25. Approximate depths of the Moenkopi and Kaibab formations from drill hole data of the south line by Roddy et al. (1975). Drill holes 4, 5, 2, 7, and 8, respectively, (shown in Fig. 2.6) were used as data points.

Once the refraction analysis was completed, smoothed refraction statics were applied to the seismic data, shown in Fig. 2.26. In addition, since the topography at Meteor Crater varied greatly, elevation statics were deemed necessary to correct for these changes. Using a replacement velocity of 2000m/s, a smoothed floating datum to fixed datum elevation static shown in Fig. 2.27 was applied.

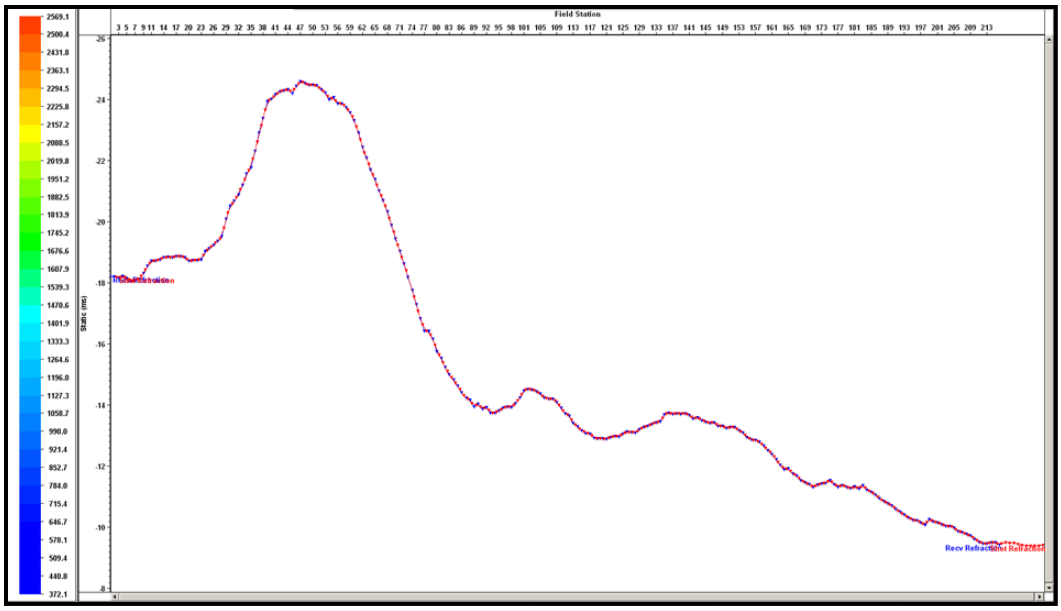

Fig. 2.26. Smoothed long-wavelength refraction statics applied to the Meteor Crater seismic data. Velocity along the y-axis ranges from 372 m/s to 2,569 m/s. The x-axis represents field stations from 3 to 213 (each field station is 3 m apart).

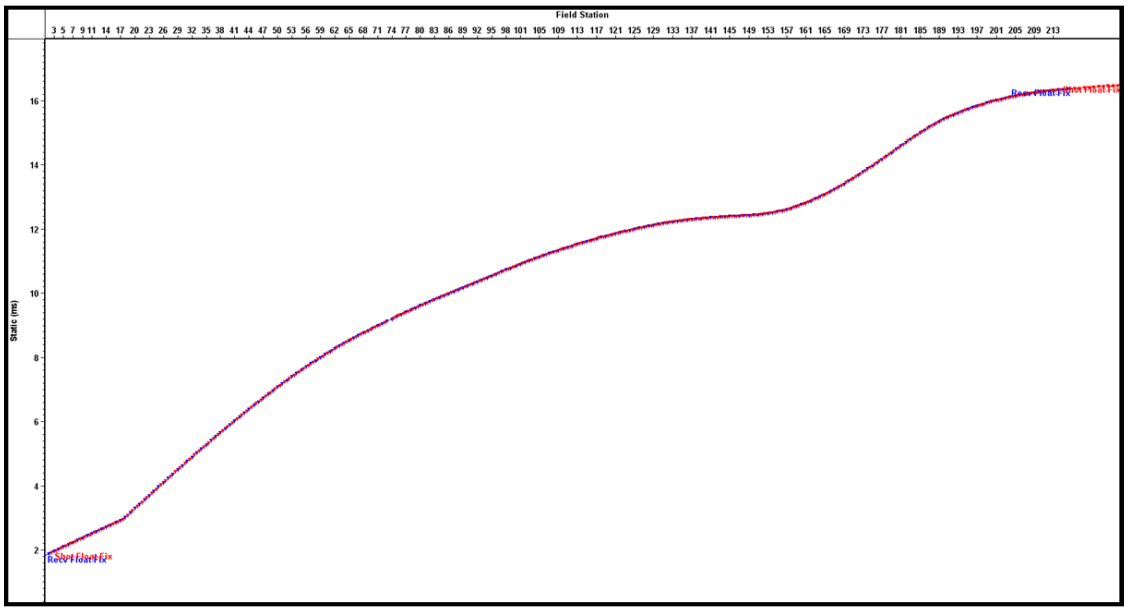

Fig. 2.27. Time vs. field station diagram of floating to fixed datum (elevation) statics applied to the Meteor Crater seismic data. The elevation static along the y-axis ranges from 2 ms to 16 ms. The x-axis represents field stations from 3 to 213 (each field station is 3 m apart).

Like most hydrocarbon exploration-scale seismic processing workflows, deconvolution (decon) was applied next. Although numerous near-surface seismic reflection processing workflows do not include decon (Baker, 1999; Baker et al., 1998; Buker et al., 1998; Shtivelman et al., 1998), Kaiser et al. (2009) propose the process to increase the resolution of shallow reflections within the optimum reflection window. The necessity for implementing decon in this study is multifold. Firstly, many other near-surface studies utilized a rifle as a source instead of an accelerated weight drop—a rifle source more closely resembles an impulse than a weight drop. Also, this study was acquired using 14 Hz geophones as opposed to 40 Hz or even 100 Hz receivers and the data were acquired with 3 stacks. As a result, the dominant frequency of the signal was much lower than in other studies. Lastly, other studies were interested in the very near-surface (topmost 50 m or even 10 m) while this study is interested in imaging 200 m or more. Thus, decon was applied to increase the resolution of the seismic data in the time domain by attempting to create a reflection series.

In this case, predictive decon was used instead of spiking decon to avoid boosting high-frequency noise in the data, which is abundant in this study. The predictive decon operator length and prediction lag used were 100 ms and 10 ms, respectively. The predictive decon had the effect of suppressing the high-frequency end of the spectrum while preserving the overall spectral shape of the input data as well as predicting and attenuating multiples (Yilmaz, 2001). In addition, a 20-160 Hz band-pass filter was applied to the deconvolved data set to remove any high frequency artifacts and noise.

Fig. 2.28 and Fig. 2.29 show shot gather 60 before and after decon and filtering and their respective normalized frequency spectra.

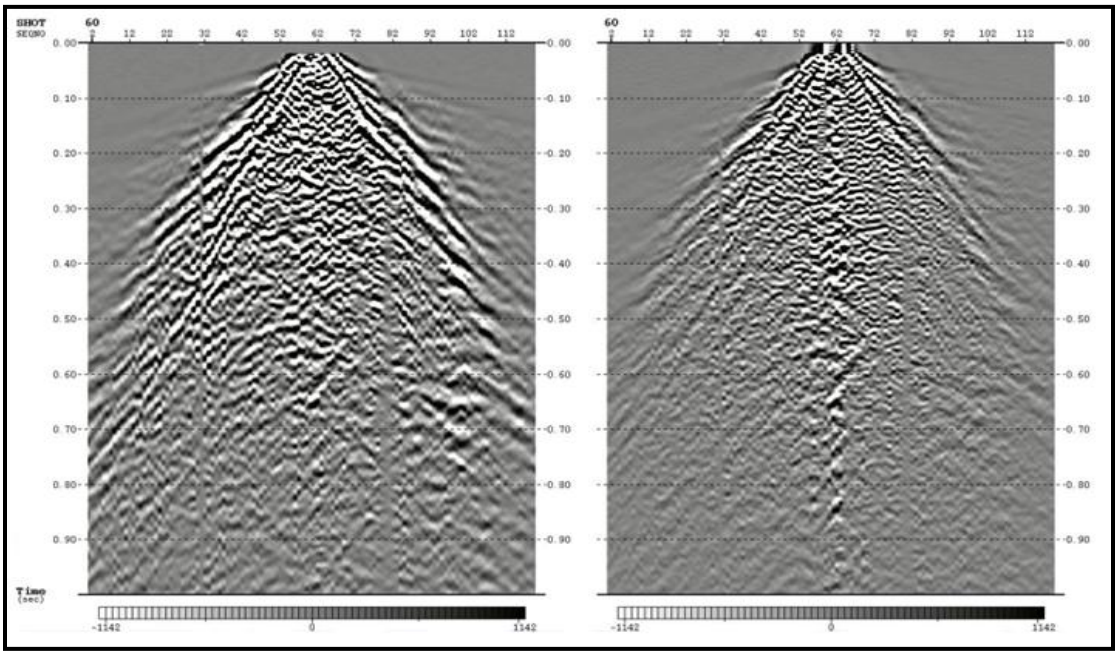

Fig. 2.28. Shot gather 60 before (left) and after (right) predictive decon was applied. X-axis represents traces from 1 to 120 and the y-axis denotes time from 0 to 1 s. Amplitude spectrum at bottom ranges from -1142 to 1142.

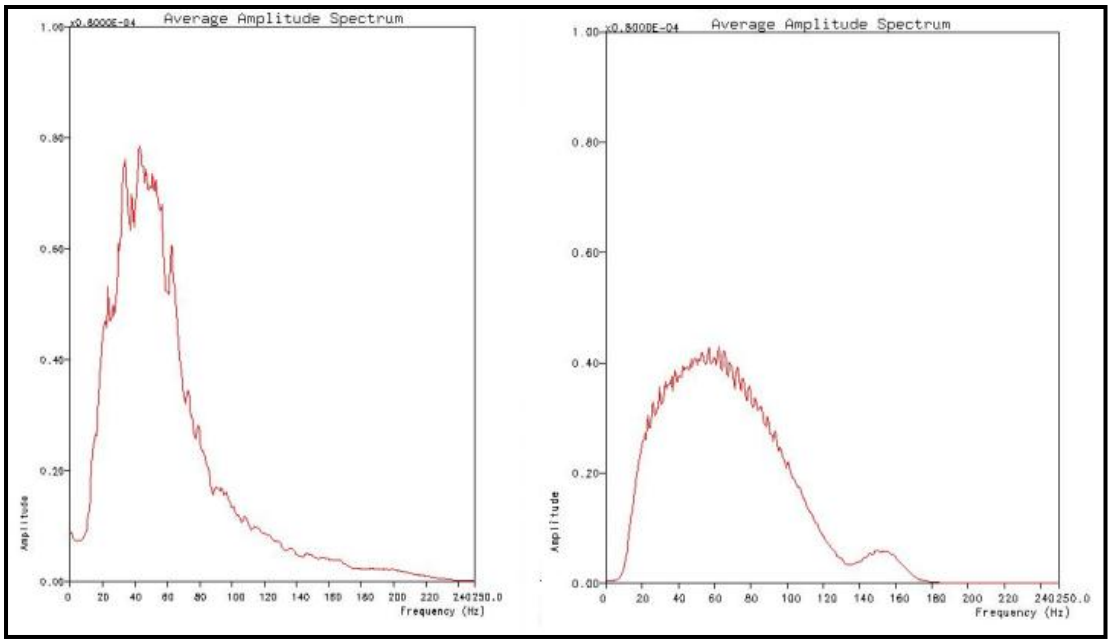

Fig. 2.29. Normalized frequency spectra of shot gather 60 before (left) and after (right) predictive decon was applied. Frequency is alon the x-axis from 0 to 250 Hz. The y-axis represents normalized frequency time 0 to 1.

Next, linear coherent noise was attenuated within the data set. This step was completed in two phases: first, a suite of linear moveout (LMO) filters was applied to remove low velocity and low frequency ground roll and then a top mute was applied to separate the refractions from the reflections (Fig. 2.30). Several LMO filters were applied, each increasing in velocity from 100 m/s to 900 m/s and containing a bandwidth of 0-20 Hz. Since a quick inspection of the ground roll revealed velocities of no more than 700 m/s, a 900 m/s filter was deemed sufficient. In addition, to refrain from removing higher frequency signals of interest that may reside in the noise cone, a 0-20 Hz low-cut filter was utilized.

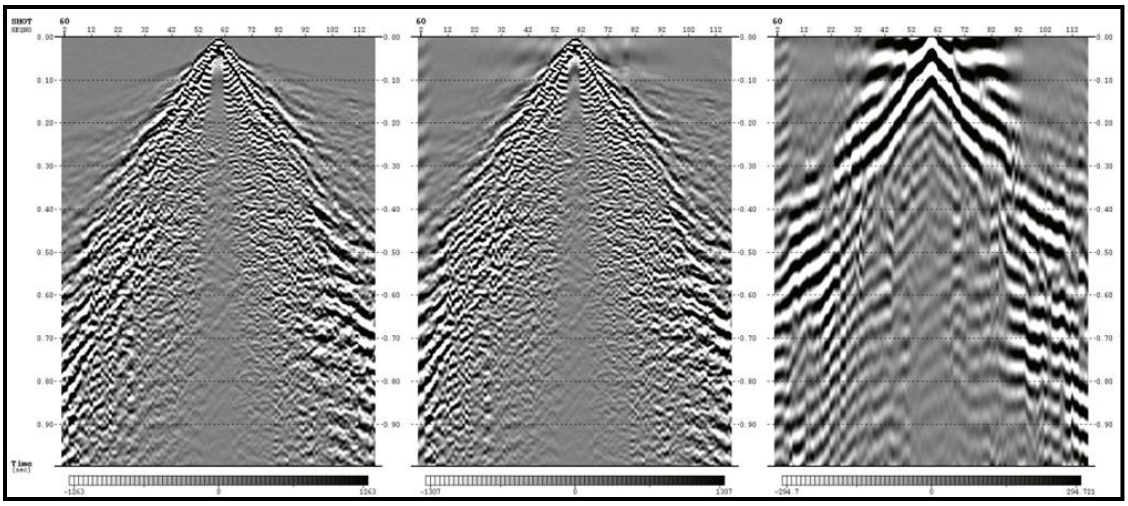

Fig. 2.30. Shot gather 60 before (left) and after (middle) LMO filtering. Figure at right shows the difference between the two, or the effect of the LMO filters. X-axis represents traces from 1 to 120 and the y-axis denotes time from 0 to 1 s. Amplitude spectrum at bottom varies in range.

To minimize imaging refractions as reflections in the final stacked section, a top mute was implemented (Fig. 2.31). This mute removed the topmost coherent signal within the data set, which most likely consists of refraction data. Although simple and effective, it is not certain whether all of the refractions were removed—coherent events just below the mute could also contain refraction events. Nonetheless, to refrain from removing possible reflection data, the remaining coherent signals were left intact. The possibility of these events consisting of refractions will be kept in mind during interpretation.

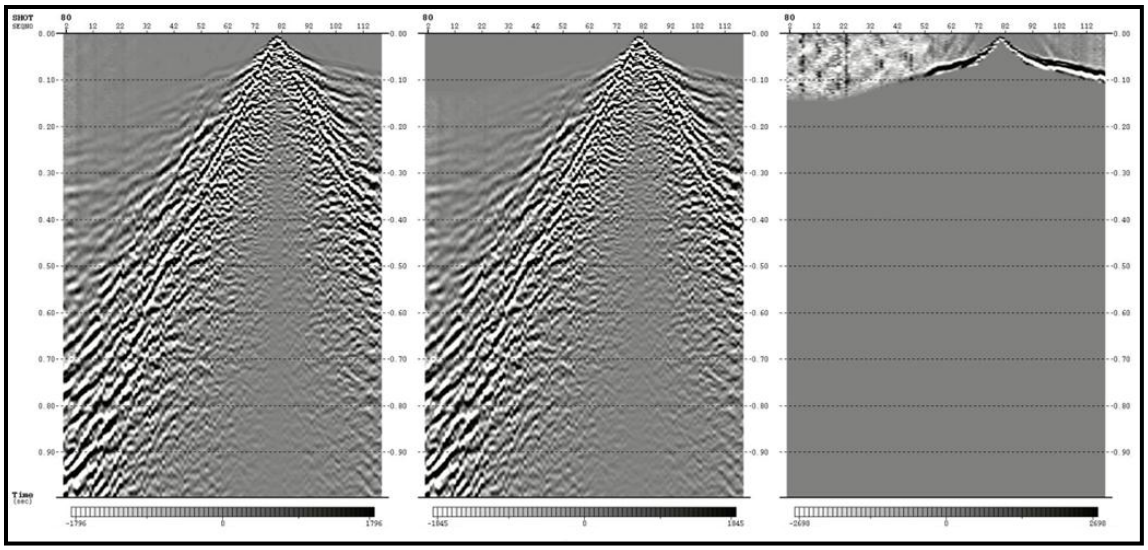

Fig. 2.31. Shot gather 80 with a 200 ms AGC window applied (left). Same shot gather with the top mute applied (middle). Effect of tope mute is shown at right. X-axis represents traces from 1 to 120 and the y-axis denotes time from 0 to 1 s. Amplitude spectrum at bottom varies in range.

To further increase the S/N, a frequency-wave number (f-k) filter was applied. The f-k filter was designed to remove coherent signals up to about 500 m/s, as the f-k mute region in Fig. 2.32 shows. This particular velocity was chosen because most of the ground roll resides in this range, whereas reflection signals are at a much higher velocity. Although f-k filters may generate linear coherent signals, an f-k filter was applicable in this study because very little noise existed in the same spatial orientation as the reflections and the ground roll was fairly coherent. Also, the f-k filter was designed to be fairly gentle to refrain from causing the data to look "wormy." The filter was effective in removing much of the linear coherent noise residing in the noise cone due to ground roll and air blast, as Fig. 2.33 demonstrates.

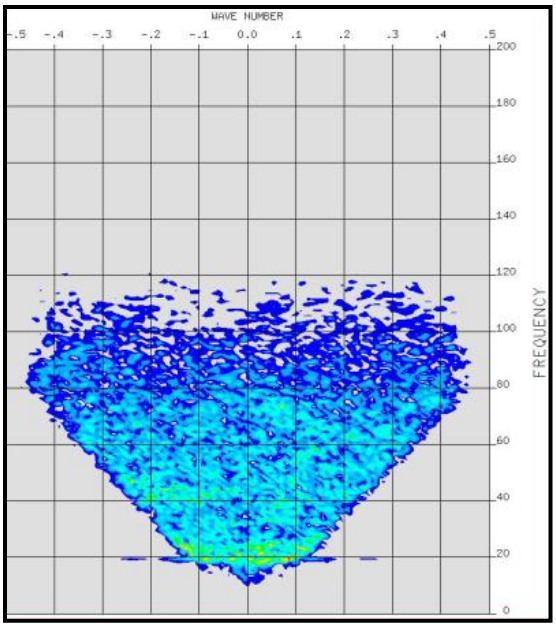

Fig. 2.32. F-k spectrum of shot gather 60 from Meteor Crater seismic line. F-k mute region is symmetrical about the origin and is limited to about 500 m/s.

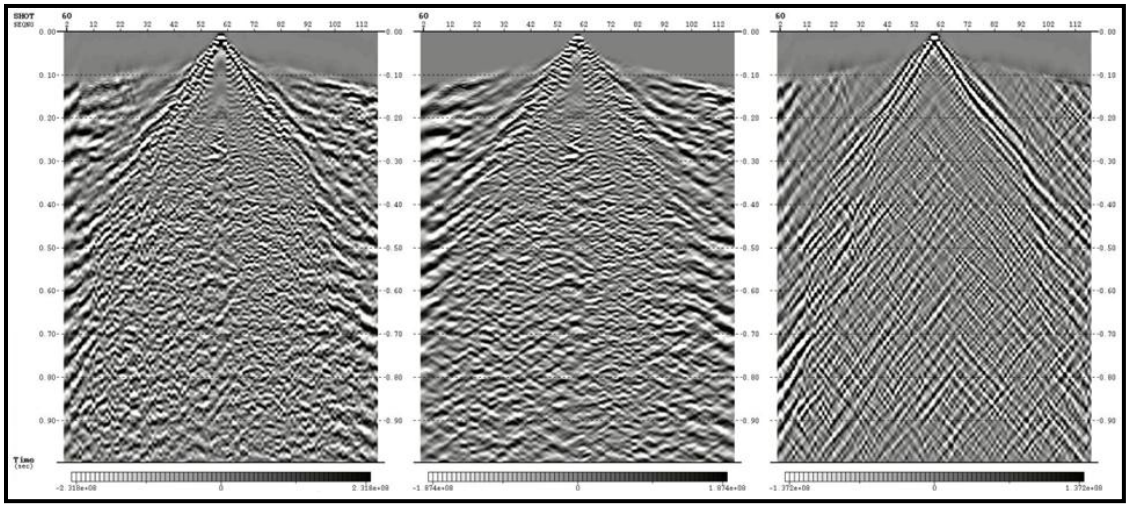

Fig. 2.33. Shot gather 60 with a 200 ms AGC window (left). Same shot gather with the f-k filter applied (middle). Data removed by the f-k filter is shown at right. X-axis represents traces from 1 to 120 and the y-axis denotes time from 0 to 1 s. Amplitude spectrum at bottom varies in range.

After increasing the S/N with the various aforementioned filters, the data were then CMP sorted and analyzed for subsurface normal move-out (NMO) velocities. To do

so, numerous constant velocity stacks (CVSs) were first created to gain a sense of appropriate velocities to image reflectors in the subsurface. Fig. 2.34 shows CVSs at 1500, 2000, and 2500 m/s; it is clear from the figure that a 2000 m/s CVS shows several possible reflectors in the near-surface best. Next, a semblance plot and common offset stacks were created. Velocities were then picked utilizing the information obtained from the refraction analysis, the CVS stacks, and previous published works (Kring, 2007; Roddy, 1978). After picking NMO velocities every 20 CMPs, an initial velocity structure of the subsurface along the length of the seismic line emerged (Fig. 2.35). An initial examination of the NMO velocity structure shows an increase in velocity from left to right, in agreement with Ackermann and Godson (1975). A 30% stretch mute was then applied to the NMO-corrected CMP gathers and they were then CMP-stacked. To increase the coherency of the stacked section, an 80 ms frequency-distance (f-x) deconvolution operator was applied. Next, a 30-120 Hz band-pass filter was implemented to remove any final low and high frequency noise and artifacts residing in the section. Fig. 2.36 shows the stacked section after f-x decon and band-pass filtering.

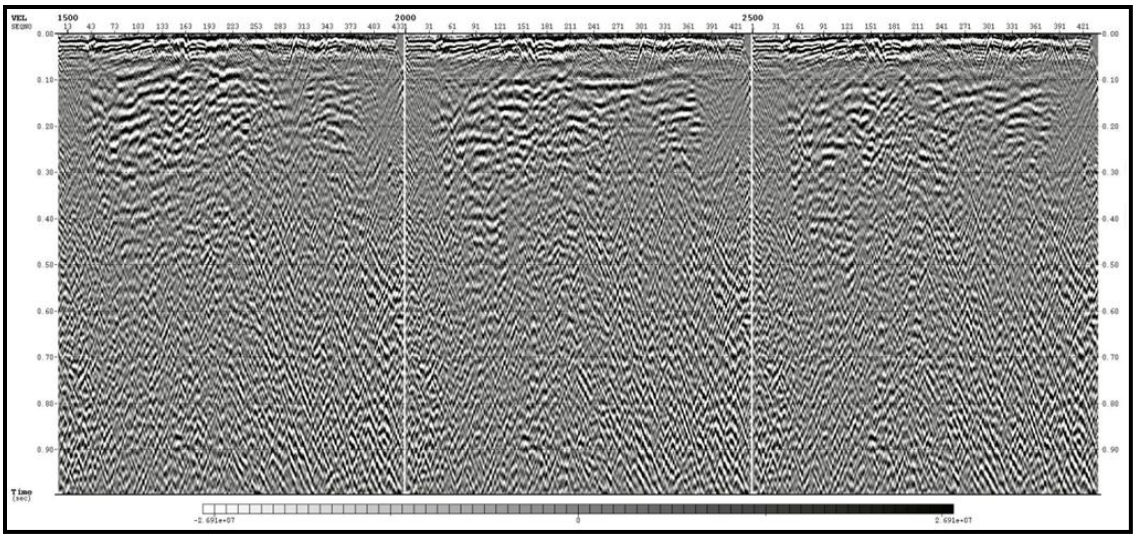

Fig. 2.34. Constant velocity stacks: 1500 m/s (left), 2000 m/s (middle), and 2500 m/s (right). X-axis represents CMPs 1-430 and time is along the y-axis from 0 to 1 s.

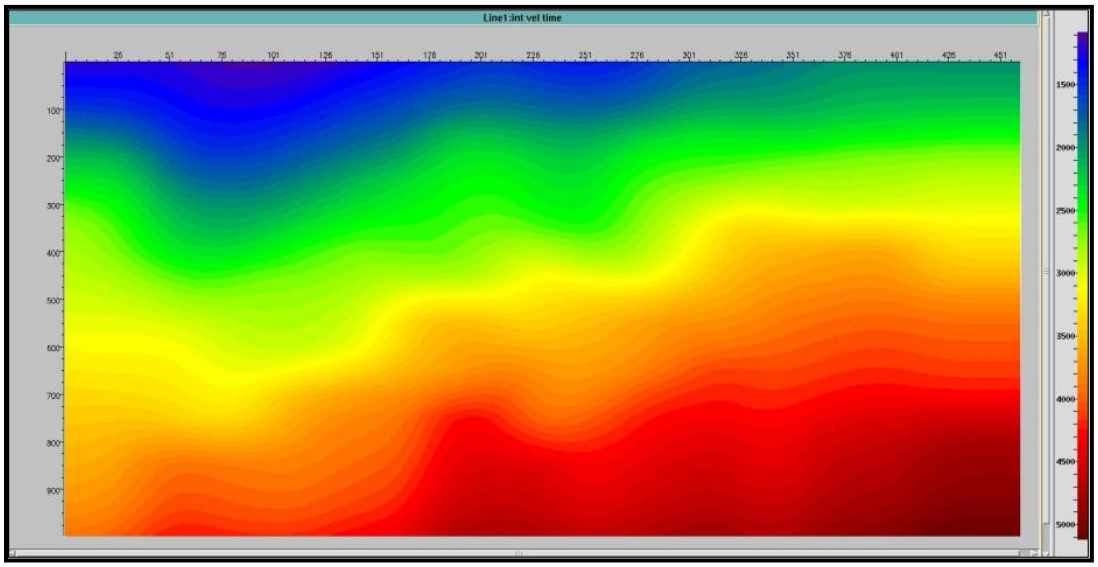

Fig. 2.35. NMO velocity structure of the Meteor Crater seismic line based on velocity anlysis. Velocity along the y-axis ranges from 1000 to 5000 m/s. CMPs along the x-axis range from 1 to 451.

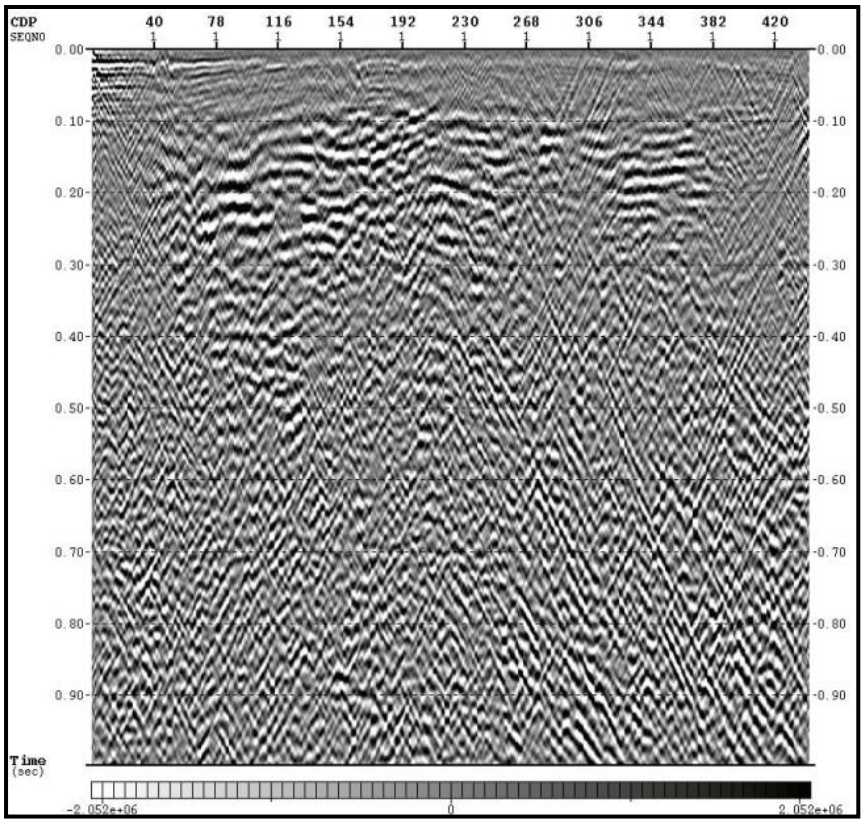

Fig. 2.36. Brute stack of Meteor Crater seismic data after f-x decon and band-pass filtering. The lateral distance is 658 m (67 CMPs roughly equal 100 m).

To collapse diffractions and increase lateral resolution, a post-stack Kirchoff time migration was applied. After trial and error, a migration aperture of 15 m was utilitzed over the entire section and the same velocity structure that is shown in Fig. 2.35 was used. Finally, the data were truncated to 500 ms to focus on the discernible reflectors. The final migrated and truncated time section is shown in Fig. 2.37. An interpretation of the seismic data is carried out in the following section.

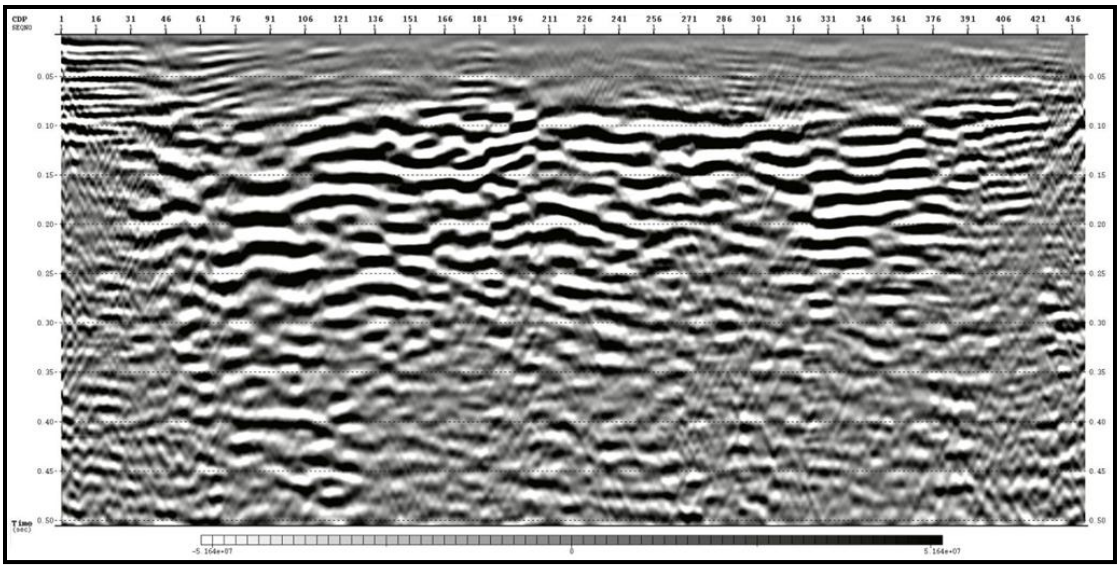

Fig. 2.37. Post-stack Kirchoff time migrated section of Meteor Crater seismic survey.

2.6. Interpretation

Since the migrated seismic section shown in Fig. 2.37 is more poorly imaged than the CMP stacked section shown in Fig. 2.36, the simple stacked section was used for interpretation. It is not surprising that migration has reduced the quality of the seismic data—a very complex subsurface such as at Meteor Crater needs a respectively complex velocity structure to migrate the image properly. In this case, only a simple velocity model as the one shown in Fig. 2.35 could be obtained. Fig. 2.38 shows the CMP stacked section after applying a median filter to attenuate noise. The red-black amplitude color palette is used to better resolve the reflections, which are numerous between 100 ms and 300 ms, although possible coherent reflectors are visible up to 500 ms.

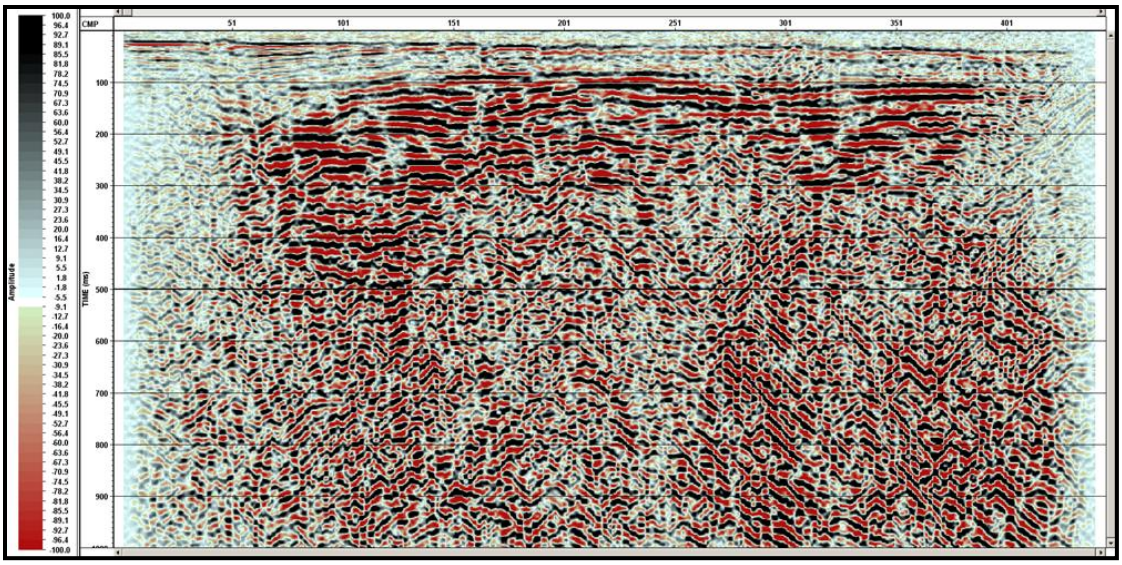

Fig. 2.38. CMP stack of Meteor Crater seismic data after noise attenuation. The y-axis ranges from 0 to 1000 ms and the x-axis ranges from 0 to 440 CMPs (or 660 m).

Before any interpretation of the data can take place, however, it must first be mentioned that the seismic section shown in Fig. 2.38 may contain refractions along with reflections. Although certain steps have been taken to mitigate this problem (top mute, low-cut frequency filter, LMO filtering, etc), the possibility remains that several of the top "reflections" are in fact refractions. Nonetheless, the interpretation of the seismic section was made under the assumption that all coherent signals below 100 ms are reflections. With that in mind, the seismic data were analyzed and interpreted.

The seismic section shows several sub-horizontal reflections around 100-200 ms, which seem to be dipping slightly to the north (left, towards the crater), in agreement with the depth-to-time converted simple synthetic model of the crater shown in Fig. 2.11. Thus, the dip of the beds is not real, but rather a result of the subsurface velocity structure. The lower reflections also have a similar character, although they seem to be

more fragmented and disjointed, possibly implying a more complex subsurface. However, it must be remembered that deeper reflectors tend to be more poorly imaged because of energy losses associated with transmission, absorption, and reflection. In addition, the area between CMPs 230 and 300 at 200 ms and beyond seems to have very low resolution. Although this phenomenon could be due to some complex structure, it may likely be the result of low CMP fold (Fig. 2.17) due to acquisition design.

The depth of penetration seems to be greatest around CMP 100, where reflections up to 400 ms are well imaged. Further along the line, reflections can only be made out to about 300 ms. The results are counterintuitive since the ejecta layer is thickest and the formations are expected to be most brecciated and disturbed near the crater rim, and therefore most poorly imaged. Thus, it is likely that the depth of penetration is also due to the CMP fold as a result of the acquisition design. Indeed, the greatest subsurface fold is at CMP 120, where reflectors are imaged to 400 ms, and least at CMP 250, where the deepest reflection can be seen only at about 250 ms (Fig. 2.17).

A structural interpretation of the stacked seismic section is shown in Fig. 2.39. Four prominent horizons were picked along the peaks of 4 reflections. The horizons were picked based upon their high amplitude, coherency, and extent. It is uncertain what lithologic contacts they represent without a synthetic tie from a nearby offset well, although horizon 1 could represent the Kaibab/Coconino, horizon 4 the Coconino/Supai, and horizons 2 and 3 intra-formational heterogeneities within the Coconino. Faults were also interpreted on the seismic section. The solid black lines represent faults interpreted from anomalies within the refraction analysis and discontinuous reflections within the

stacked seismic section. The dotted black lines represent faults interpreted only on the stacked seismic section where discontinuities seem present. It is uncertain whether the faults are reverse, as one would expect in a compressional environment, or normal, due to slumping—the resolution of the seismic data is simply too low.

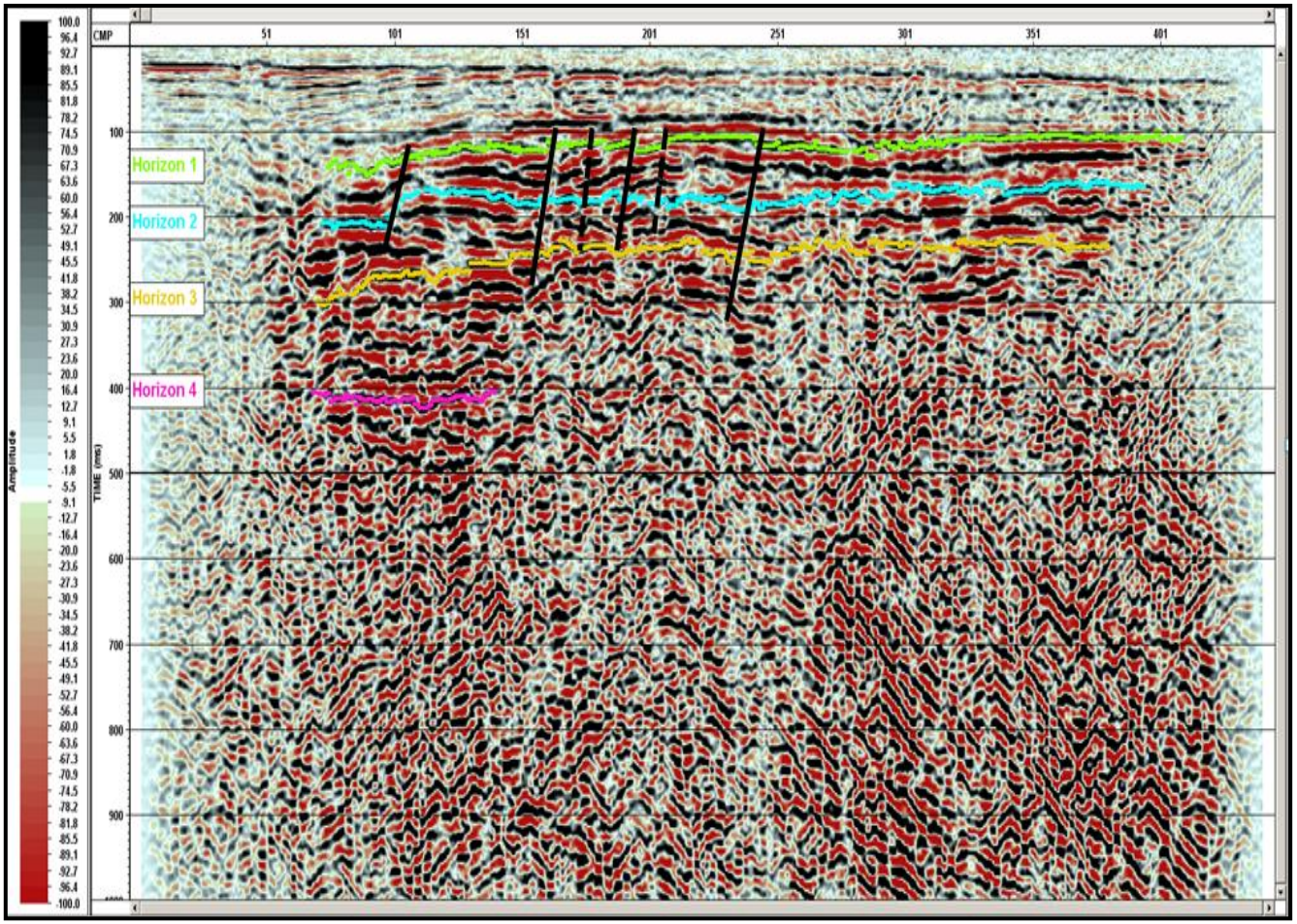

Fig. 2.39. An interpretation of the Meteor Crater seismic section shown in Fig. 2.37. The y-axis ranges from 0 to 1000 ms and the x-axis ranges from 0 to 440 CMPs (or 660 m).

2.7 Discussion/Conclusions

The results of the first reflection seismic study at Meteor Crater indicate numerous nearly flat-lying reflectors, intersected by a number of faults—not unlike previous geologic and geophysical work of the astrobleme (Kring, 2007). Although the beds surrounding Meteor Crater are actually dipping away from the crater, the reflections seem to be dipping towards it (north), an indication of lower velocities and greater thickness of fractured/brecciated rock near the crater rim, as expected. Low coherency of reflections was taken as a sign of possible complex deformation, although inconsistent CMP fold coverage could have also been a factor. Since the expected faults in the near-surface are at, or below, the limit of the resolution of the seismic data, seismic refraction analysis was used in conjunction with the reflection results to better define them.

Although useful information regarding the astrobleme's structure was had from this study, it has also served as a learning experience for future seismic investigations at Meteor Crater and elsewhere. The extreme structural complexity and thick ejecta blanket in the near-surface have created an unfavorable environment for seismic acquisition, resulting in low quality (low S/N and low frequency) data. To mitigate these problems in future seismic surveys, several recommendations have been proposed.

Lowest quality seismic data are often obtained in areas where the weathering zone (or ejecta layer) is low in moisture, thick, and coarse-grained (Hunter et al., 1984). Since the near-surface at Meteor Crater accommodates these criteria, it should not be surprising that the data quality of this survey is also low. The reason for the lack of high frequencies is mainly due to a low Q-factor of the ejecta blanket, which causes high frequency waves

to attenuate more quickly. However, other reasons that may have contributed to the poor quality of the data include poor geophone coupling, windy conditions, surface noise, ground roll, a weak source, a complex subsurface, out-of-plane reflections, low fold, and low-frequency geophones.

Numerous authors have recommended the use of high-frequency geophones over their lower frequency counterparts (Doornenball and Helbig, 1983; Steeples and Miller, 1998; Hunter et al., 1984). Many of these near-surface studies have typically used 40-100 Hz geophones to strongly discriminate against surface waves and allow near-offsets to properly record near-surface reflections, such as the ejecta blanket/Moenkopi reflector. Although theoretically there should be no difference in data quality between frequency-filtered low-frequency geophone data and unfiltered higher frequency geophone data, Doornenball and Helbig (1983) have concluded that the former are significantly inferior to the latter. Thus, it may be worthwhile to acquire future seismic data at Meteor Crater with higher frequency receivers if understanding the very near-surface is an objective.

Although using high-frequency geophones may sound counterintuitive since higher frequencies are attenuated more quickly in such an environment, a more powerful source, such as a vibroseis truck (vibe), may be the answer to recording deeper reflections. A recent study conducted at the University of Houston has shown a dramatic improvement in data quality and depth of penetration when a vibe source is used over the AWD system (Appendix B). Since the vibe, like the AWD, is a non-destructive source, it can be easily applied in future seismic studies at Meteor Crater. If the depth of

investigation is the very near-surface, an impulse source such as a shotgun may prove to be useful.

In addition to a more powerful source, burying geophones several feet underground could also increase the quality of the acquired data. Although time- and labor-intensive, the increase in geophone coupling, decrease in travel-time of seismic waves through the attenuative ejecta blanket, and reduction in exposure to the elements could well be worth the extra effort.

Lastly, the complexity of the near-surface may also be partly responsible for the poor data quality. If the geology were layer-cake-like, out-of-plane reflections would be nonexistent and reflections would be more coherent. However, since the object of this study is to image a complex near-surface, it is recommended that 3-D data be acquired in the future. Although more expensive and difficult to acquire and process, wide- or full-azimuth 3-D data would create a true image of the subsurface, allowing for proper interpretation. Such data would also be useful in analyzing fracture-induced anisotropy, which would broaden our understanding of the role of pre-impact joint sets on the shape of the astrobleme.

Chapter 3

Meteor Crater, AZ—Potential Field Methods

3.1 The Gravity Method

3.1.1 Acquisition

The gravity survey at Meteor Crater consists of 5 separate lines in the southern portion of the crater rim, including a line along the main SSE seismic line (Fig. 3.1). It is important to note here that Line 1 of the gravity survey (along the SSE seismic line) begins 90 m before the start of the AWD seismic line. Thus, 0 m along the seismic line is actually 90 m along the gravity line. This conversion must be kept in mind when comparing the two data sets. Each line consists of a variable number of gravity stations. The station spacing, measured via a tape measure, remained constant throughout the survey at 30 m. At each station, 3 (or 2) readings of 60 sec duration were recorded. Two readings were obtained at each station after Line 1 in order to save acquisition time. Because of time constraints, a base reading was taken only at the beginning and end of each day to account for instrument drift. Spatial measurements at each station were obtained from GPS and LiDAR data as discussed earlier. The reader is referred to Table 1 in Appendix C for a complete list of station locations, time/date of acquisition, gravity readings, etc. Fig. 3.2 shows a gravity measurement at a station along Line 1 of the survey.

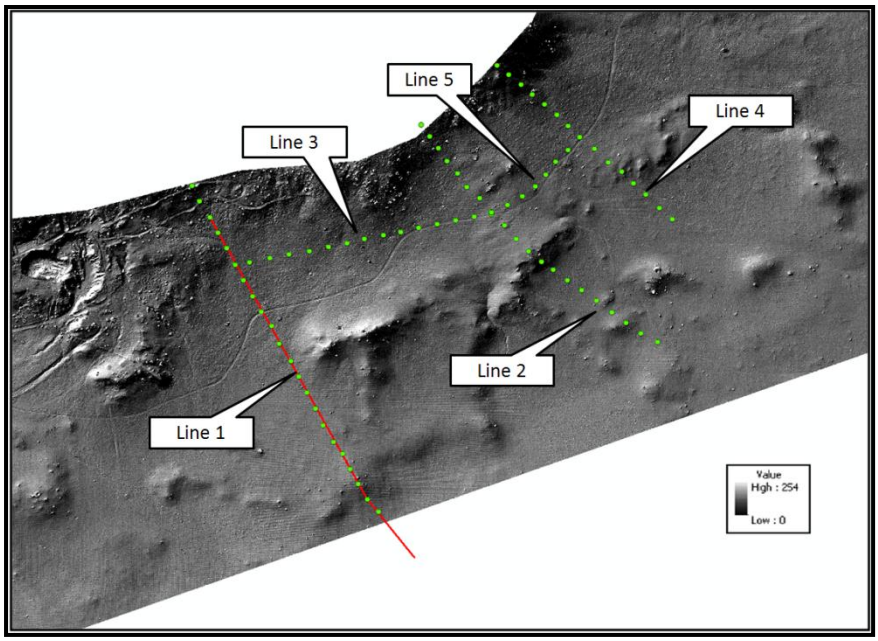

Fig. 3.1. Shaded LiDAR data image of southeastern portion of Meteor Crater. Green dots represent gravity station locations, which are separated into 5 individual lines (as annotated). Red line represents extent of AWD seismic line. Units are arbitrary and relate to amount of shading. Not that the gravity line starts 90 m before the beginning of the seismic line.

Fig. 3.2. Photo of Scintrex CG-5 relative gravimeter (gray box in foreground) at a gravity station at Meteor Crater. Rim of crater is in background (Photo courtesy of Eray Kocel).

3.1.2 Processing

To isolate the gravitational signals from the near-surface, a standard processing workflow was undertaken (Fig. 3.3). Before any of the processing steps in Fig. 3.3 could be undertaken, however, several preprocessing steps were first implemented. The standard deviation of the three readings at each station was calculated as a quality check to make sure that the readings were precise. Next, the three separate readings at each station were averaged into a single reading and output for that particular station. At this point, the latitude, longitude, and elevation of each station were also entered into the spreadsheet for later processing.

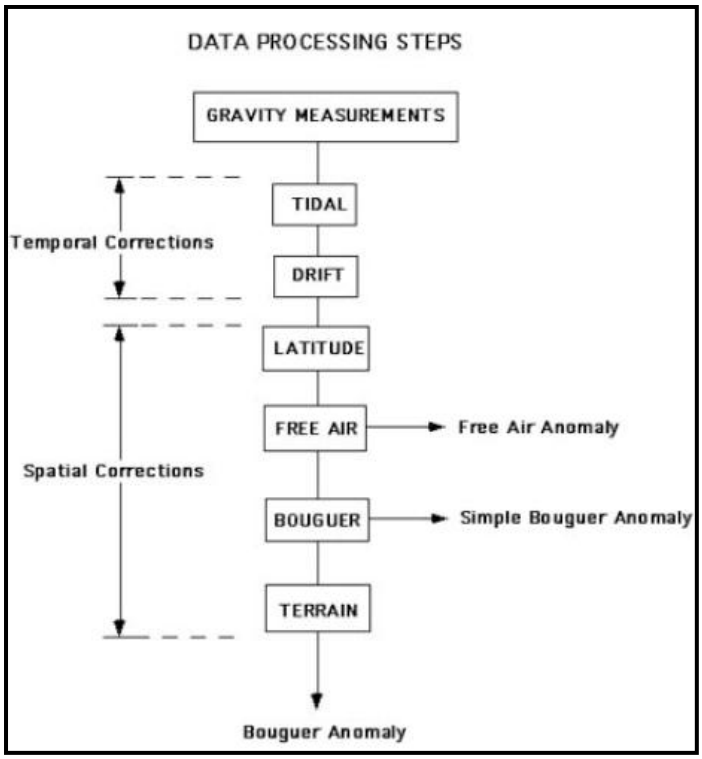

Fig. 3.3. Workflow used in processing Meteor Crater gravity data (Dr. Stuart Hall's Spring '10 Geol 7330 course, University of Houston).

Although the first step in the workflow is the tidal correction, this processing step was automatically calculated by the gravimeter at the time the data were collected. Next, the instrument drift was compensated through a linear drift correction since daily base stations were only occupied at the beginning and end of each day. Each station's gravity reading was then modified appropriately based on the time of measurement and drift rate. Although the maximum drift correction was about 0.09 mGal for a single station, the average absolute drift correction for the entire survey was 0.025 mGal, which is near the resolution of the field data (see section 1.2). Also, because the drift corrections were linear, the character of the gravity field along the lines was essentially preserved.

The remaining processing steps in the workflow, known as spatial corrections, relate to the position of each gravity station. The first, the latitude correction, was calculated by simply using the station's latitude in the International Gravity Formula (IGF):

$$g_0 = 9.7803267714\left(\frac{1+0.001931851386\sin^2\lambda}{\sqrt{1-0.006694379990\sin^2\lambda}}\right)$$

Where g_0 = latitude correction and λ = geographic latitude in decimal degrees. The IGF latitude correction was then subtracted from the observed value at each station to correct for differences in latitude. Since the intended accuracy of the survey is 0.01 mGal, the latitude accuracy needed to be within 20 m, which is well within the accuracy of the GPS unit.

After the latitude correction, the gravity data were then corrected for changes in elevation, known as the free air correction. On average, the gravitational field of the Earth decreases by 0.3086 mGal for every meter above sea level. Thus, to maintain an accuracy of 0.01 mGal, the elevation of each station needed to be known to within ± 3 cm. Since the LiDAR data has an accuracy of about ± 5 cm, the free air correction itself is then only accurate to within 0.01-0.02 mGal. Nonetheless, the accuracy is still well below the expected changes in the gravity field that may result from geologic structures in the subsurface. Thus, with the datum fixed at mean sea level, the data were compensated for the free air corrections accordingly. Although most of the gravity stations were covered by the LiDAR data, several stations near the rim crest were not, namely station 1 of Line 1 and station 8 of Line 2. These stations were not corrected for elevation variations, and were thus not included in further processing steps.

The next step in the processing workflow was the Bouguer correction, which took into account the additional gravitational attraction of material between the stations and mean sea level. For the Bouguer correction to be effective, an average density of the material between the highest and lowest stations had to be known. A density of 2.3 g/cc was chosen based on average dry bulk densities of 2.28 g/cc and 2.29 g/cc obtained from shallow drill core holes MCC-3 and MCC-4, respectively, in the vicinity of Meteor Crater (Kring, 2007). The gravitational attraction that was subtracted from the free air anomaly was based on an infinite planar slab of thickness h (in meters) and density ρ (g/cc):

$$g_{Bouguer} = 2\pi\gamma\rho h = 0.04193\rho h \text{ (mGal)}$$

Although most surveys with little topographic relief end as simple Bouguer anomalies, an additional step, known as the terrain correction, was included in this study. This was done because the topography along the survey was highly variable and the gravitational effects of the surrounding terrain do not conform to a uniform slab. Indeed, previous gravity studies of Meteor Crater have also included terrain corrections (Regan and Hinze, 1975; Harding, 1954). Although several methods, such as the Hammer method, have been developed for such purposes, their time-consuming nature and the fact that these corrections have already been calculated for Meteor Crater in a previous study (Regan and Hinze, 1975) has made their utility unnecessary. Instead, an interpolation from Regan and Hinze's 1975 study of previously calculated terrain corrections was used to save time and effort (to do so, the same Bouguer correction was used as in Regan and Hinze, 1975). This terrain correction is a modification of Kane's (1962) method which employs prisms of a segment of an annular ring to approximate the gravitational attraction (Regan and Hinze, 1975). The reader is referred to Regan and Hinze (1975) for a more complete description.

Fig. 3.4 shows a 30% transparent spline-interpolated terrain correction map of Meteor Crater from Regan and Hinze's (1975) terrain corrections overlaid on top of the LiDAR elevation data map. Station locations from Regan's study and those from this study are in green and yellow, respectively. Because the interpolated terrain correction decreases in a concentric manner from the center of the crater (as expected) and is similar to the results obtained by Regan and Hinze, the author is confident that these interpolated values are fairly accurate and representative of the true terrain corrections. After the

appropriate terrain corrections were added to the simple Bouguer anomaly, the complete Bouguer anomaly was obtained and the gravity processing was complete. Fig. 3.5 shows the complete Bouguer anomaly of Line 1.

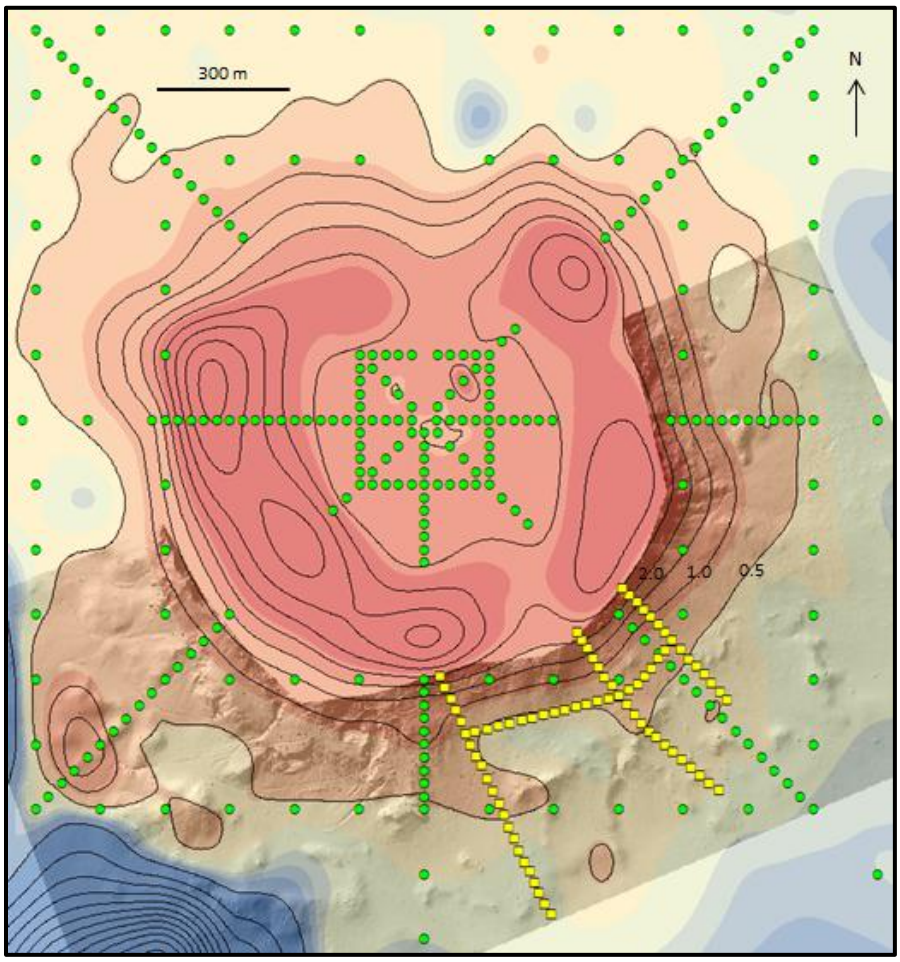

Fig. 3.4. A transparent spline-interpolated terrain correction map of Meteor Crater overlaid on top of the LiDAR data map. Station locations from Regan's study and those from this study are shown in green and yellow, respectively. The contour interval is 0.5 mGal.

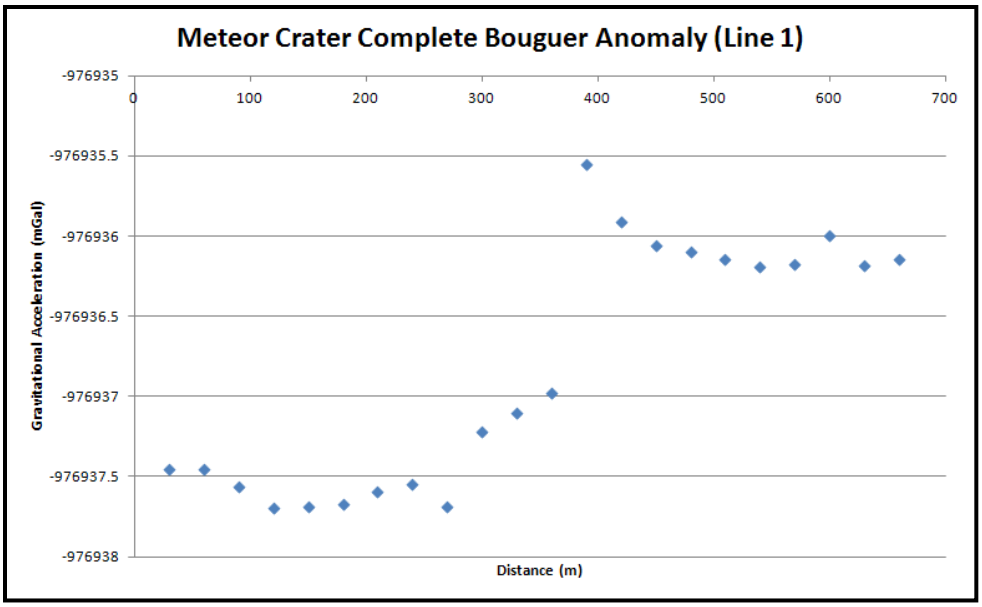

Fig. 3.5. Complete Bouguer Anomaly of Meteor Crater gravity Line 1.

It is clear from Fig. 3.5 that a mis-tie is present at 390 m along Line 1 and is not representative of the true subsurface geology. This anomaly is the result of a gravimeter malfunction at the beginning of the second day of acquisition along the same line. As a result, gravity measurements at stations 15 and 16 of Line 1 were very variable and contain large standard deviations, meaning that the data are neither precise nor accurate. This problem is resolved in the next section after anomaly separation.

3.1.3 Interpretation

The purpose of interpreting gravity data from a survey is to isolate only the signals related to density changes in the subsurface that are of interest, while removing all other frequencies from the composite signal. Because this gravity study is only interested

in the near-surface, the goal was to remove all long-wavelength signals, or the regional gradient, while preserving the shorter wavelengths (residual signal). This process is known as anomaly separation.

To calculate the regional gradient, a best-fit 2nd order polynomial was calculated using data obtained from Regan and Hinze's 1975 study; the 1975 data set was used because of the study's large extent. Second order polynomials were calculated from stations along the N-S and E-W lines that were far from the crater rim (Fig. 3.6). These regional latitudinal and longitudinal trends were then subtracted from stations along this survey to obtain a residual anomaly pertaining to shallow density changes. Fig. 3.7 shows the residual anomaly of Line 1.

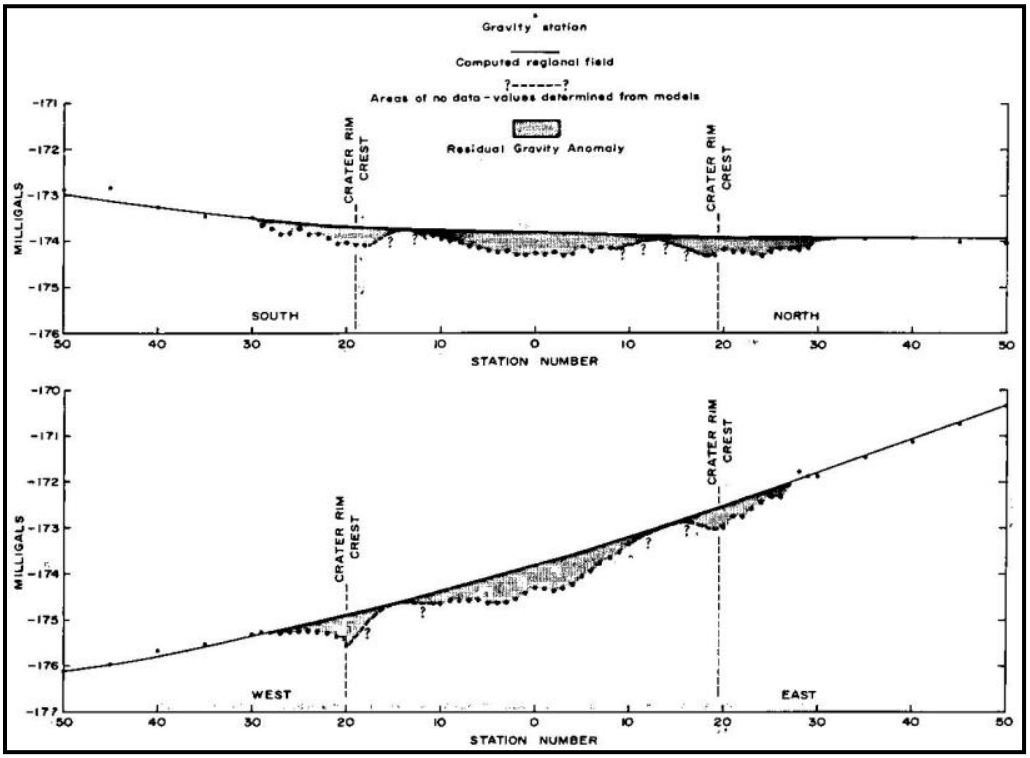

Fig. 3.6. North-south (top) and east-west (bottom) regional gradients at Meteor Crater, Arizona (from Regan and Hinze,1975).

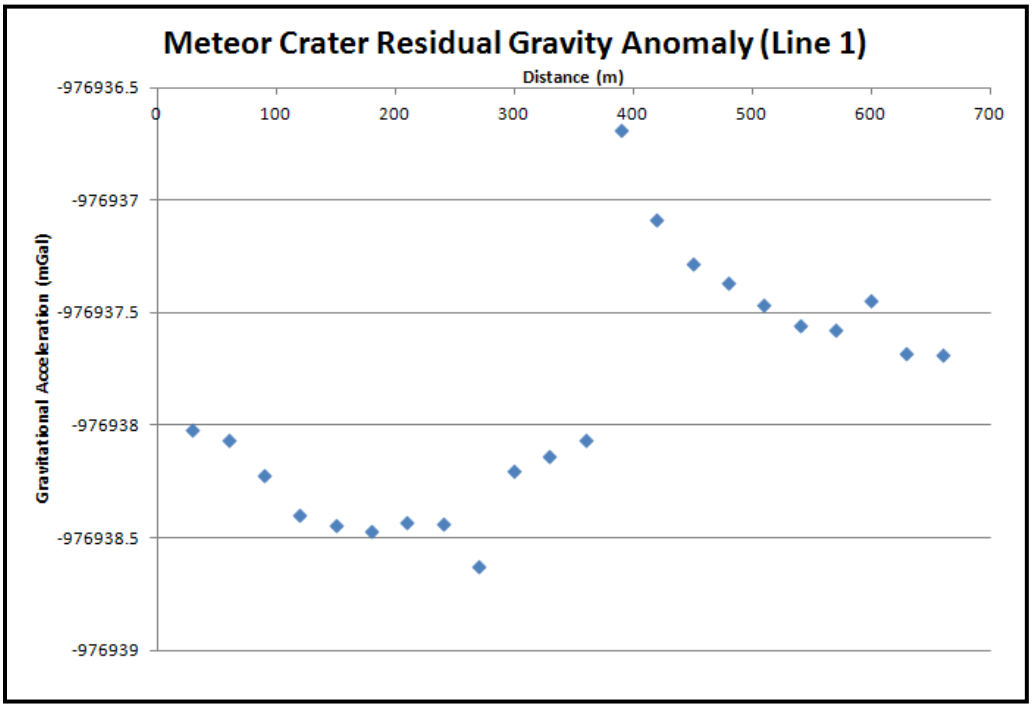

Fig. 3.7. Meteor Crater residual gravity anomaly of Line 1.

After obtaining the residual gravity anomaly, the mis-tie problem was then resolved. Since the processed seismic line does not show any indication of a large fault or other structural anomalies at the location of the mis-tie, the two data sets were merged by simply decreasing the gravity field of the latter half of the line via a datum shift of 1 mGal and then interpolating the spurious gravity reading at station location 390 m. Although the method is not very precise nor scientific, it is the best that can be done to salvage the entire line. The results of this simple data manipulation are shown in Fig. 3.8.

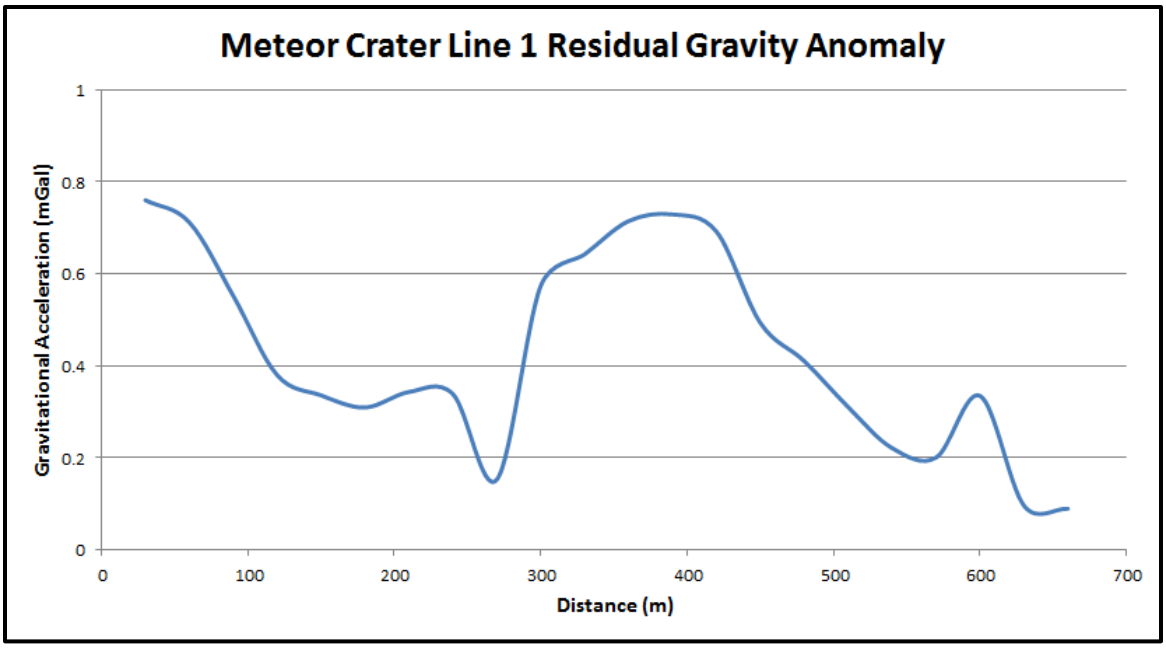

Fig. 3.8. Meteor Crater residual gravity anomaly of Line 1 after resolving the mis-tie problem.

The overall trend of the gravity line seems to decrease at first, then increase, and finally decrease at the tail end. To test for an extensive density anomaly that could be responsible for such a gravity response, the other two radial lines (2 and 4) were tied to Line 1 via common stations along Lines 3 and 4. All three lines were then graphed alongside each other with respect to distance from the center of the crater as defined in Fig. 2.5 (Fig. 3.9). The results show a depression and then rise in the gravity field along the other two lines as well, similar to Line 1 (Line 4 was shorter and no data exist beyond 420 m). This may be indicative of a concentric structure present along the southern rim, such as a graben-like depression due to faulting. In fact, the residual gravity anomaly of the southeast line from Regan and Hinze's 1975 study supports the trend seen in Fig. 3.9 (Fig. 3.10).

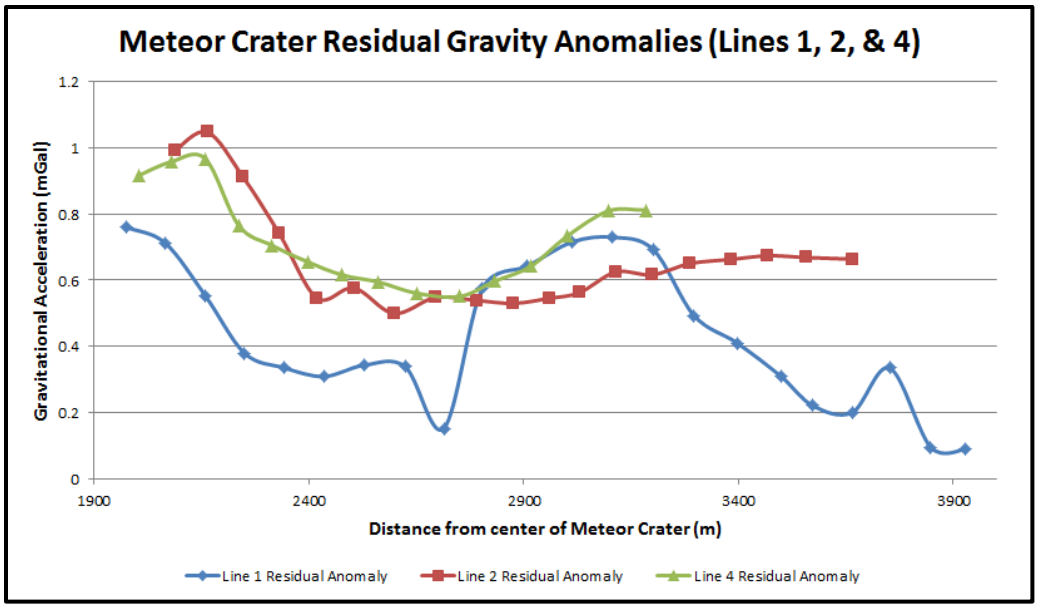

Fig. 3.9. Gravity vs. distance plot of residual gravity anomalies of radial Lines 1, 2, and 4.

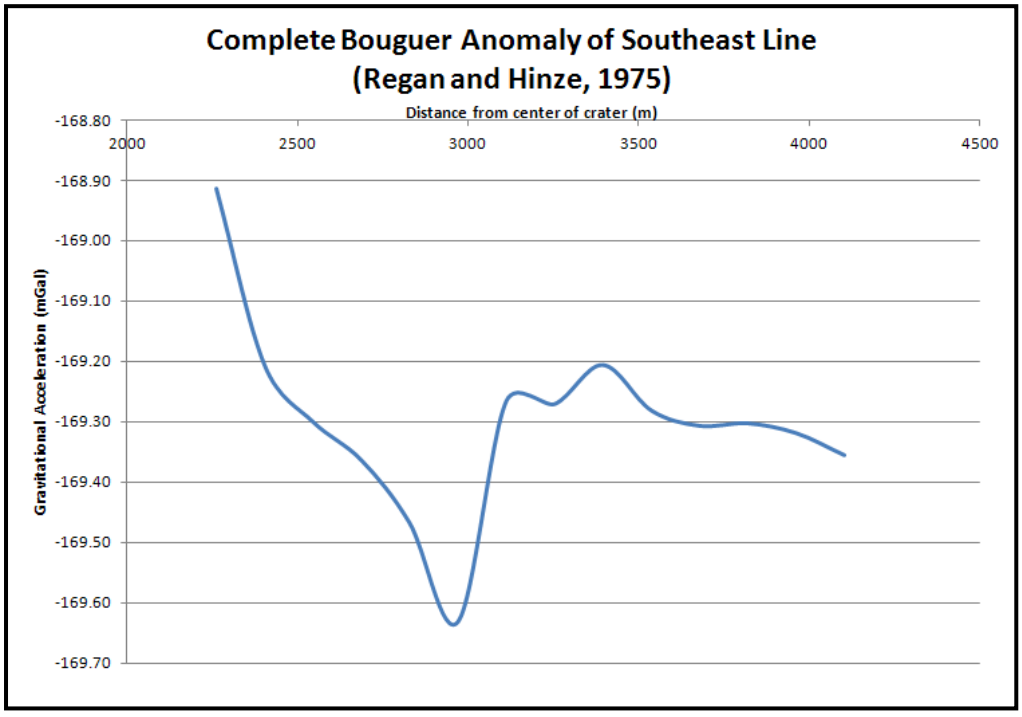

Fig. 3.10. Residual gravity anomaly of southeast line from Regan and Hinze's 1975 gravity study.

Fig 3.11 shows a transparent natural neighbor interpolation of the three gravity lines superimposed on the DEM. Apparent lows and highs are denoted. The figure shows a relative low at about 200 m from the crater rim along the three lines. The low then becomes a high where the topography increases and outcrops are seen at the surface. This concentric change in the gravity field could either be the result of the topography itself (through an inaccurate Bouguer or terrain correction) or could be a function of subsurface structure that has also had an effect on the surface topography. To better test this hypothesis, more radial gravity lines around the crater and a more accurate terrain correction are needed.

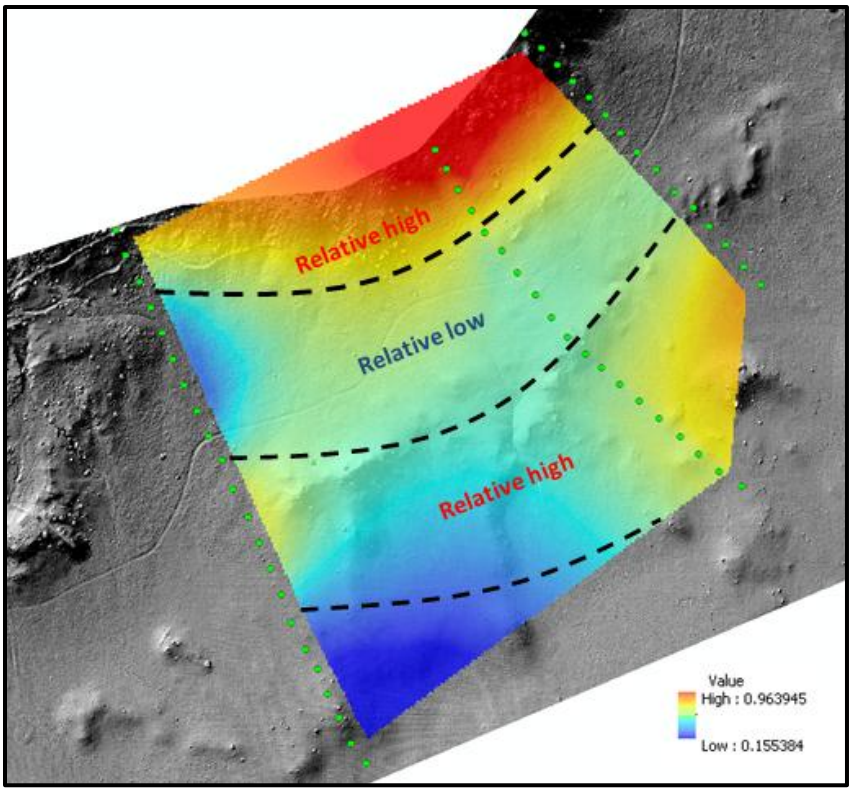

Fig. 3.11. Transparent natural neighbor gravity interpolation of radial lines 1, 2, and 4 superimposed on the DEM of the southern rim at Meteor Crater.

After anomaly separation and data manipulation, knowledge of the surrounding geology was utilized in creating a simple forward model of the subsurface (Fig. 3.12). The figure consists of the model (bottom), the gravitational field resulting from the model (solid black line), and the actual acquired gravity data (black dots). The model was constructed from previous geologic studies of the crater (Kring, 2007; Roddy et al., 1975). From top to bottom, the layers consist of the ejecta blanket, the Moenkopi, and the Kaibab formations. The model densities of these respective layers, obtained from Roddy (1978), are 2.07, 2.27, and 2.28 g/cc. The deeper layers are not modeled because of their insignificant effect on the short wavelength gravity field.

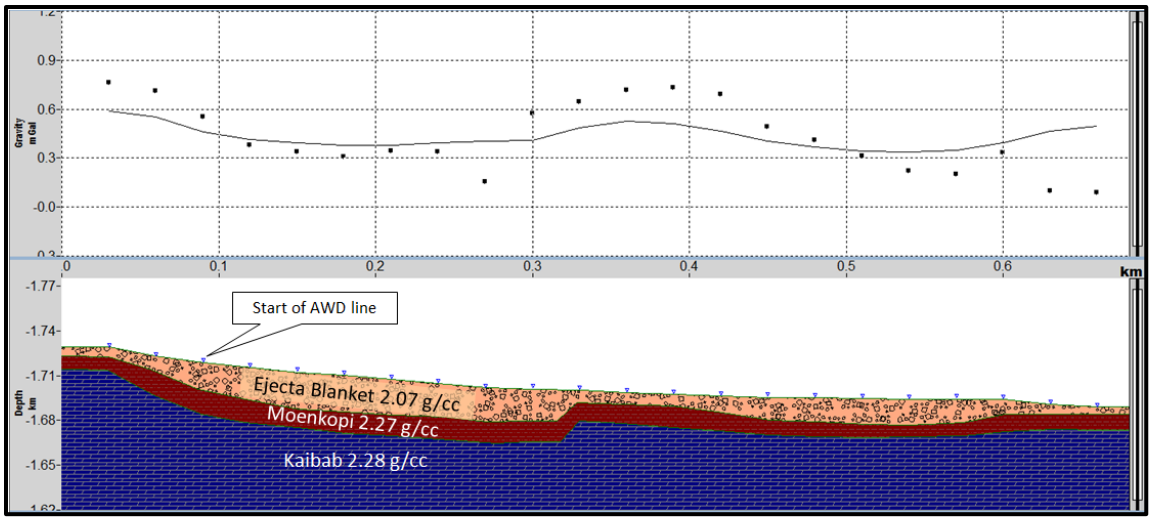

Fig. 3.12. Simple forward gravity model of the subsurface, similar to the model in Fig.2.8. Solid black and dotted lines represent the gravity response from the model and actual acquired gravity data from the field, respectively.

The character of the gravitational field resulting from the model (solid black line) is in close agreement with the acquired field data (black dots). Although the gravity misfit between the acquired data and model is 0.175 mGal, or a quarter of the total

change in the gravity, the disparities occur mainly at the beginning and end of the gravity line. These differences could be the result of a variety of factors, including inaccurate subsurface structure, poor density control, improper terrain or Bouguer corrections, and 3-D changes in the subsurface structure that are unable to be captured by the 2-D model. Indeed, since the survey is a single 2-D line, the model is created under the assumption that the subsurface along strike (perpendicular to the survey line) is unchanging. This assumption, of course, is flawed.

Evidence from seismic data in Sections 2.5 and 2.6 suggest that a fault may be present at 340 m along the gravity survey. The refraction data indicate that it may be a normal fault with a large velocity (and therefore density) contrast across it. The modeled gravity response best fits the actual gravity data at 340 m with a normal fault of 10 m throw, as is shown in Fig. 3.12. However, the density contrast may be too small to properly resolve the feature using the gravity method.

There are several other areas where the modeled gravitational response does not fit the acquired data, such as at 270 m, where a decrease of almost 0.2 mGal is recorded. This anomaly could be due to a more complex structure associated with the fault at 340 m. There is also disagreement between the modeled and acquired gravity data between 300 m and 450 m—the actual gravity field is about 0.2 mGal greater. This disparity is most likely the result of an improper terrain correction that does not take into consideration the structural high in the vicinity of the 300-450 m stations. A similar premise could explain the disparities at the beginning and end of the survey, where large elevation changes occur.

Fig. 3.13 shows the same model as Fig. 3.12 except with the surrounding topographical high at 370 m included as if the survey crossed over it. It also includes a higher topography at the beginning of survey to simulate the surrounding crater rim. The large disparity between the model and actual gravity field at the end of the line is also likely due to topography, although it could not be modeled properly. The figure shows that there is a strong relationship between the surface topography and resultant gravitational field—a possible indication of an improper terrain or Bouguer correction. The differences between the modeled and acquired gravity data in Fig. 3.12 could also be due to structural changes in the subsurface in the orthogonal direction that are not captured in a 2-D model. Regardless, the limitations of a single 2-D gravity survey are quite obvious.

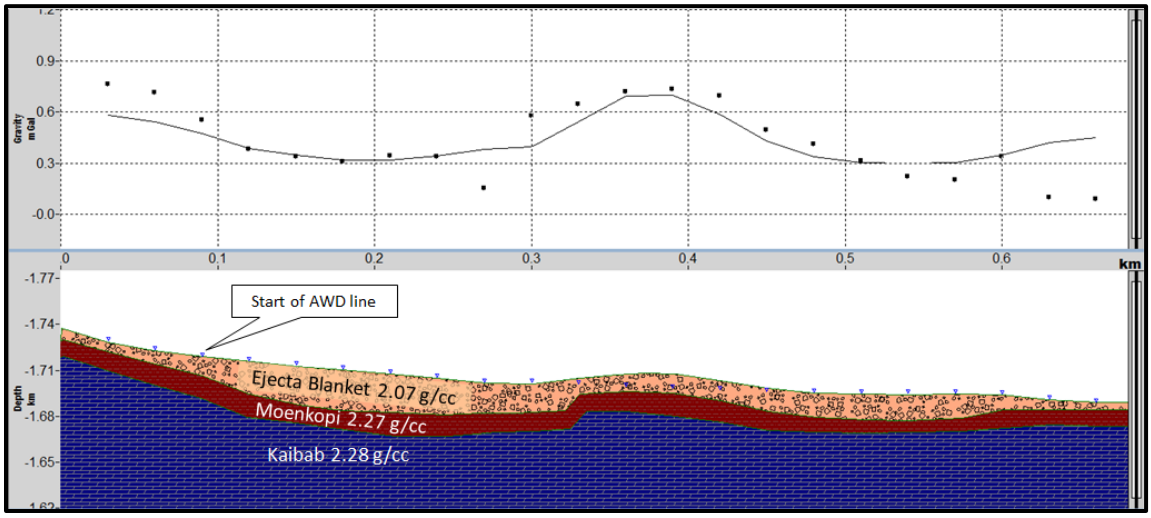

Fig. 3.13. Simple forward gravity model of the subsurface, similar to the model in Fig.3.12. Solid and dotted black lines represent the gravity response from the model and actual acquired gravity data from the field, respectively. The misfit between the two is 0.14 mGal. The model differs from Fig. 3.12 through a higher topography at the crater rim and at 370 m.

One way to eliminate the processing problems associated with the Bouguer and terrain corrections is to simply end data processing and interpretation with the free air anomaly. Fig. 3.14 shows the free air gravity response of the forward model in Fig. 3.12—the background density of air is 0 g/cc. Excluding the beginning of the line, the character of the gravity response of the model (solid black line) is in good agreement with the acquired free air anomaly data. The difference between the actual and modeled free air gravity data is 0.31 mGal, or about one-tenth of the gravity change along the length of the survey. Although the initial results seem encouraging, it quickly becomes obvious that the modeled and actual free air anomaly are directly related to the topography of the survey—the greatest density change, and therefore gravitational effect, occurs at the interface between the surface and air. Because the topographical effects overwhelm the smaller-scale mass perturbations, the free air anomaly is ineffective in accurately characterizing small scale subsurface features, as was expected.

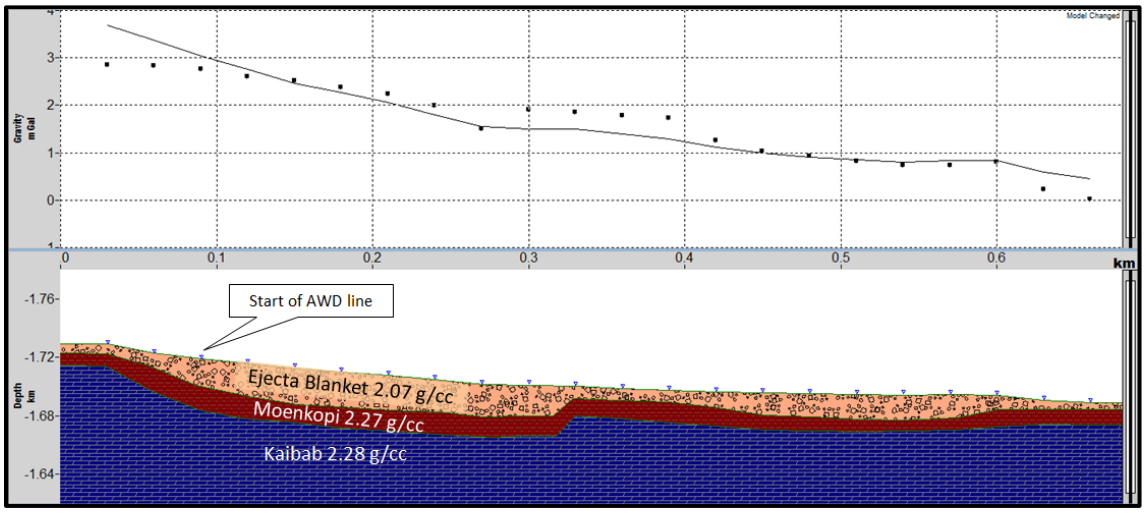

Fig. 3.14. Simple forward free air gravity model of the subsurface, similar to the model in Fig.3.12. Solid and dotted black lines represent the free air gravity response from the model and acquired gravity data, respectively. The gravity misfit is 0.31 mGal.

Although the character of the modeled gravity response in Fig. 3.12 matches the acquired gravity field fairly well, the model may still be incorrect because of the non-unique nature of gravity data. In fact, the model in Fig. 3.12 differs from the subsurface velocity model shown in Fig. 2.24, even though a relation between density and velocity is known (Gardner, 1974). Using the Gardner equation as a guide, a separate forward model was created using the velocity model in Fig. 2.24 (Fig. 3.15). The assumption behind the model is that brecciation of the bedrock decreases with distance from the crater rim, leading to grater velocities, and therefore densities. As is clearly evident, the gravity misfit between the model response and the acquired data is quite large at 0.28 mGal—the greatest disparity occurs at the beginning of the line, where the elevation change is most abrupt. Because of numerous flaws that could have affected the acquired gravity line (improper Bouguer density, terrain correction, and line tie) and the difficulty in building an accurate model (structurally complex subsurface, lack of density well logs, a 3-D environment, etc.), it is not certain whether the gravity misfit in Fig. 3.15 is the result of improper data processing (i.e. the residual gravity anomaly is inaccurate) or the model is an inaccurate representation of the subsurface (i.e. density is not closely associated with velocity in this area), or both. As is often the case, more data are needed to better constrain the rock properties and model the subsurface.

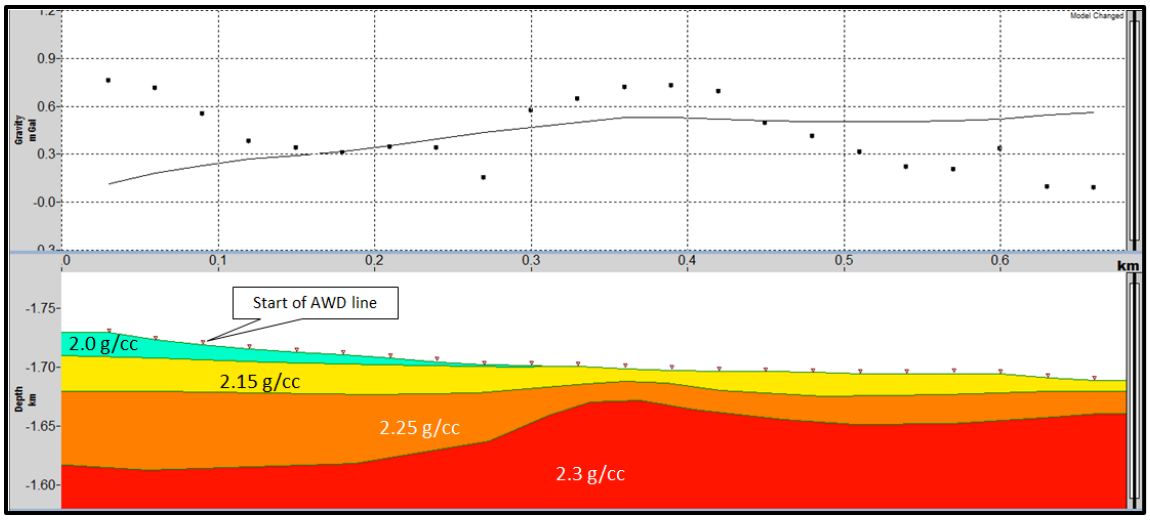

Fig. 3.15. A simple subsurface density model based on the velocity model shown in Fig. 2.24. Solid black and dotted lines represent the gravity response from the model and the acquired gravity data, respectively. The gravity misfit is 0.28 mGal.

3.2 The Magnetic Method

3.2.1 Acquisition

The magnetic survey was conducted in conjunction with the gravity survey at Meteor Crater. The magnetic survey consists of 4 lines with stations at identical locations to 4 of the gravity lines (Fig. 3.16). The fifth line was not acquired because of time constraints. The magnetometer used in acquiring the data was a Geometrics G-856AX proton procession magnetometer, mounted on a 2 meter pole to avoid any magnetic distortions related to metallic debris on the surface. The station spacing, like in the gravity survey, was 30 m and 3 separate magnetic field readings were also taken at each station. The latitude, longitude, and elevation of each station remained the same as from the gravity survey. The date and time of each observation were also recorded for

processing purposes. Table 2 (Appendix C) includes all of the raw data from the magnetic survey that may be of interest to the reader.

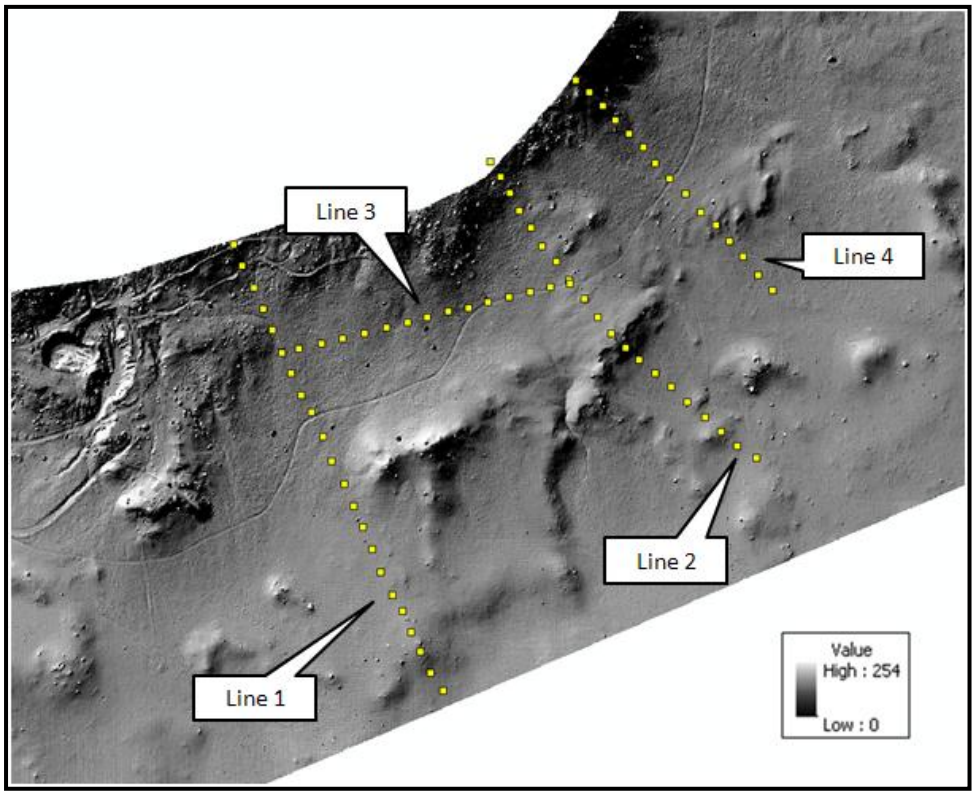

Fig. 3.16. Shaded LiDAR data image of southeastern portion Meteor Crater. Yellow squares represent magnetic station locations, which are partitioned into 4 individual lines, as annotated. Units are arbitrary and relate to amount of shading.

3.2.2 Processing

The workflow for processing the magnetic field data is twofold: a temporal (diurnal variation) correction followed by a spatial (main field) correction (Fig. 3.17). These steps are included in the workflow to isolate the geologic signal of interest and remove other known effects that are unwanted. Before any processing could occur,

however, several preprocessing steps were undertaken. First, the standard deviation of each station was calculated to inspect the data for any erroneous observations. This QC step uncovered several problematic stations: 1 and 2 of Line 1 and station 1 of Line 2. The variability of the readings at the stations pertaining to Line 1 was most likely due to old drilling equipment lying on the ground near the rim of the crater. The cause of the variability in the magnetic field at station 1 of Line 2 is less known, although anthropogenic material in the subsurface could have been the cause as well. Next, the three separate readings at each station were averaged and were output as the final single value for that station.

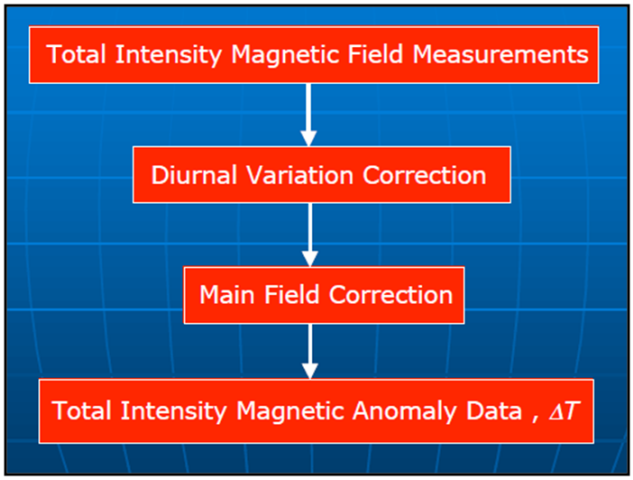

Fig. 3.17. Magnetic data processing workflow (Dr. Hall's Spring '10 Geol 7330 course, University of Houston).

As mentioned earlier, the first step in the processing workflow involves correcting the data for temporal variations. These corrections are meant to remove external magnetic components related to the interaction of the solar wind with the magnetic field of the Earth. Although these variations have cycles that vary in time, the most important cycle

to remove in this survey is the diurnal, or daily, correction since the survey was only conducted over a period of three days. To correct the data, continuous readings from a base station nearby had to be used. The closest station, in Tucson, Arizona (200 miles south of Meteor Crater) acted as the base station. The station is part of a global network of magnetic stations known as INTERMAGNET, or International Real-Time Magnetic Observatory Network. Since the data recorded at the Tucson observatory are recorded in universal time (UT), the Meteor Crater magnetic observations were converted to UT time. The difference between an arbitrary datum of 48,000 nT and the actual observations at Tucson were then calculated. These values (on the order of -5 to +20 nT) were then subtracted from the Meteor Crater observations to compensate the data for diurnal variations in the Earth's magnetic field (Fig. 3.18). The large disparity between the two curves at the beginning of the line is a result of the magnetic station at 90 m being reacquired at the end of the survey, resulting in the largest diurnal change.

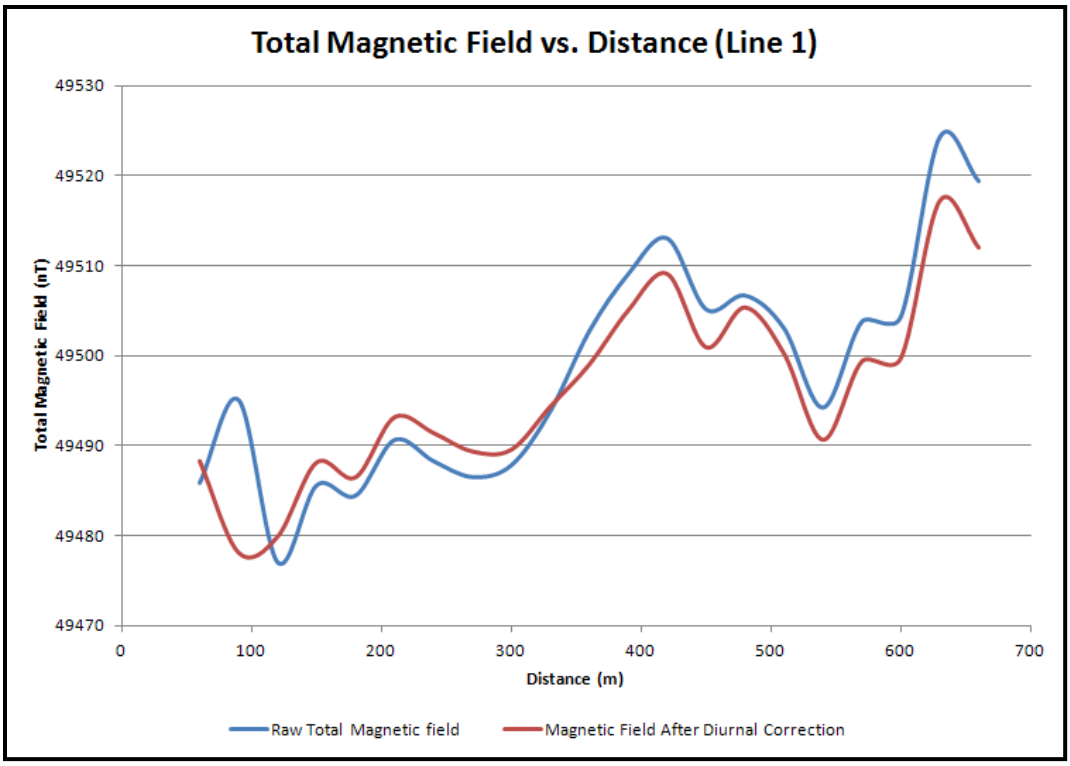

Fig. 3.18. Total magnetic field intensity vs. distance of Meteor Crater Line 1 magnetic survey. Blue and red lines represent unprocessed data and data after diurnal correction, respectively.

The second step in the processing workflow, the main field correction, was then applied to the data. This correction removes the magnetic effect of the Earth's core to isolate the magnetic effects within the crust. The International Geomagnetic Reference Field (IGRF) was calculated at each of the stations and then subtracted from the data to remove the effects of long wavelength signals from deep sources. The most recent IGRF model (IGRF 11) with the most updated coefficients was used to calculate the main field. The IGRF calculation at each station was calculated by software on NOAA's national geophysical data center website. The inputs necessary were latitude, longitude, elevation, and date of acquisition. As expected, the main field correction did not vary by more than several nT's per survey line because of the short extent of the surveys. The main field

corrections (negative values) were then added to the diurnal correction data to produce the final processed magnetic data. A -110 nT datum shift was then applied to make the values smaller and the data more manageable (Fig. 3.19).

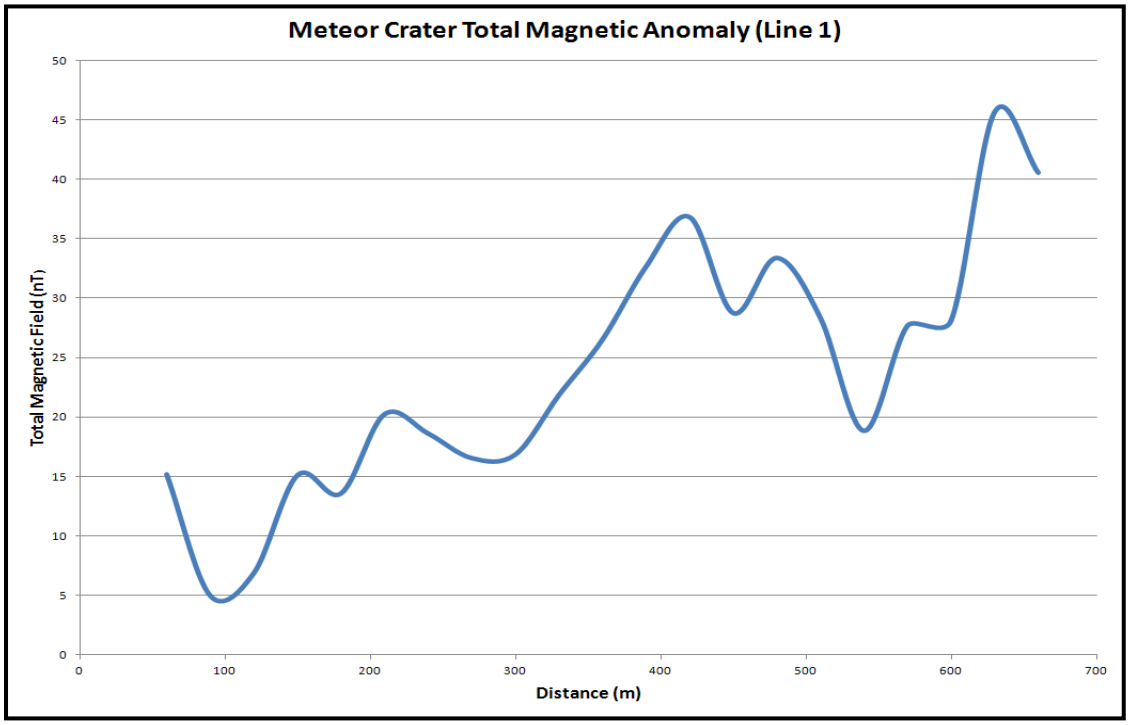

Fig. 3.19. Total magnetic field intensity vs. distance of processsed Meteor Crater Line 1 magnetic survey. Note, since this is a relative magnetic survey, 110 nT were subtracted from the initial data to improve scaling.

3.2.3 Interpretation

Like composite gravity data, total intensity magnetic anomaly data also include regional long-wavelength signals from deep sources. Again, this survey was not intended for regional magnetic anomalies associated with basement rocks, so those signals were removed. The regional magnetic field at Meteor Crater was estimated from Regan and

Hinze's 1975 study by fitting 2nd order polynomials to the N-S and E-W lines. These regional N-S and E-W trends were then subtracted from the processed total magnetic field data based on the latitude and longitude, respectively, of the stations. The result of this interpretation is a residual magnetic field map that only includes short-wavelength signals pertaining to the near surface. Fig. 3.20 shows the residual magnetic field of survey Line 1.

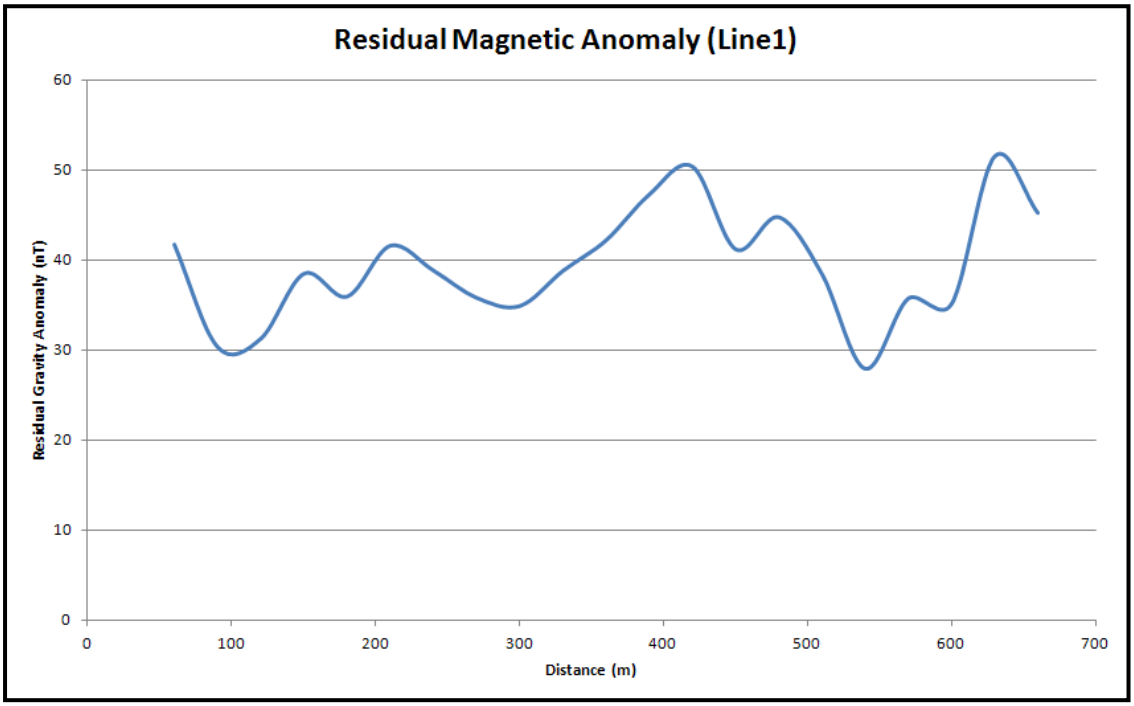

Fig. 3.20. Residual magnetic anomaly of Meteor Crater Line 1.

The residual magnetic anomaly of Line 1 appears to have several prominent highs and lows, most notably at 420 and 540 m. As with the gravity survey, the radial lines of the magnetic survey (Lines 1, 2, and 4) were graphed alongside each other to determine if they contain similar trends, an indication of possible large-scale subsurface structural features. To do so, Lines 1 and 2 were tied via common stations along Line 3. Line 4 was

unable to be tied to the other radial lines since Line 5 was missing from the magnetic survey. Thus, an arbitrary datum shift of 30 nT was applied to Line 4 to make all of the radial lines contain similar values to simplify the comparison. Fig. 3.21 shows the residual magnetic anomaly of the 3 radial lines at Meteor Crater with respect to the center of the crater as defined in Fig. 2.5.

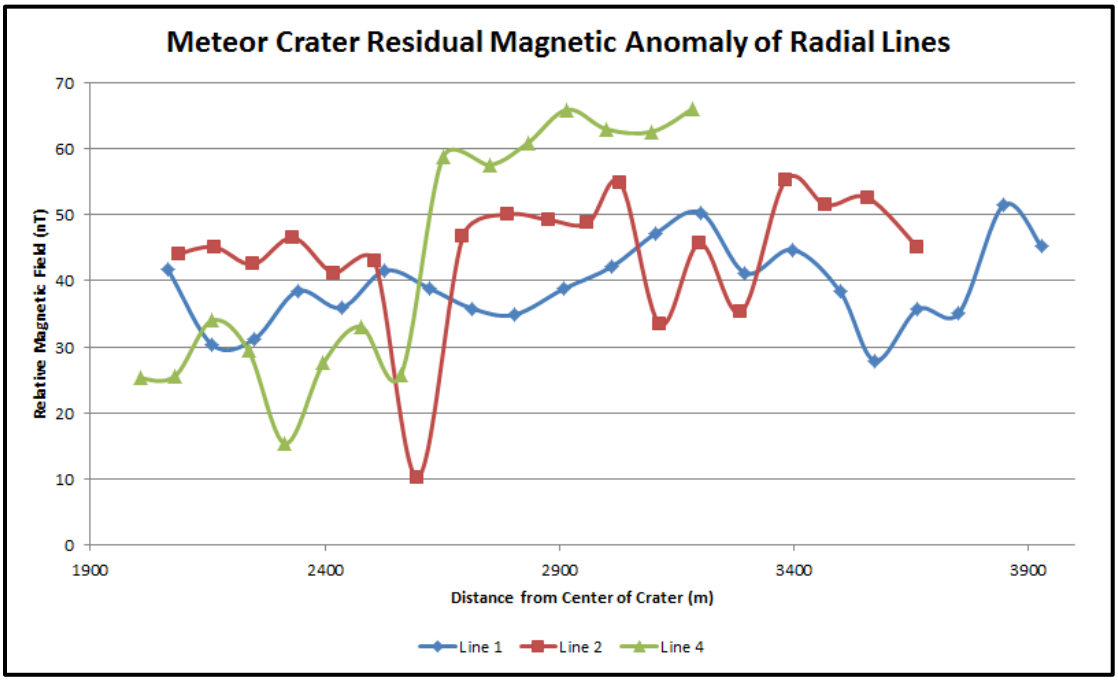

Fig. 3.21. Residual magnetic anomalies of Lines 1, 2, and 4.

An inspection of the residual anomalies of the 3 radial lines does not indicate any clear evidence of a large concentric subsurface structure that was cross-cut by the three lines. However, Line 4 shows a a rapid increase in the magnetic field of almost 40 nT, possibly the result of a subsurface fault. The large increase also roughly coincides with an increase in the gravity field along Line 4, as is shown in Fig. 3.9 . Line 2 also indicates a large change in the magnetic field at a similar distance from the center of the crater,

although it may be the result of acquisition error or an anthropogenic metallic object on the surface since it is not a longer wavelength feature. Indeed, the 30 m station spacing, or data sampling, of the survey does not allow for detailed high-resolution interpretation: the highest frequency component of the survey is twice the sampling rate, or 60 m. Thus, higher frequency data from very shallow or small sources may not be resolved properly although they may still be detected. This is discouraging since most of the magnetic anomalies are expected to result from the ejecta blanket (in the form of meteoritic material and ejected Moenkopi formation) and the iron-rich Moenkopi formation.

Next, the magnetic field response of the model shown in Fig. 3.12 was generated (Fig. 3.22). To do so, the Earth's magnetic field parameters (magnitude, inclination, and declination) at the time and location of the survey were input into GM-SYS. These values were obtained from the IGRF 11 model. Next, the magnetic susceptibility and remanent magnetization of each formation were input. Unfortunately, no hand samples were collected from the field for magnetic testing. However, the magnetic properties of the Moenkopi red beds, known for their iron content, have been studied extensively (Purucker et al., 1980; Baag and Helsley, 1974). From these studies, the magnetic susceptibility and remanence of the Moenkopi formation were estimated to be 0.00025 cm^3/mol and 0.00055 emu/cc (15° inclination and -15° declination), respectively. The magnetic susceptibility and remanence of the ejecta blanket and Kaibab formation were set at zero since neither is known to have strong magnetic properties and samples were not collected for testing. Fig. 3.22 shows the simple forward model (at bottom) along

with the actual magnetic field (dotted line) and magnetic response from the model (solid black line).

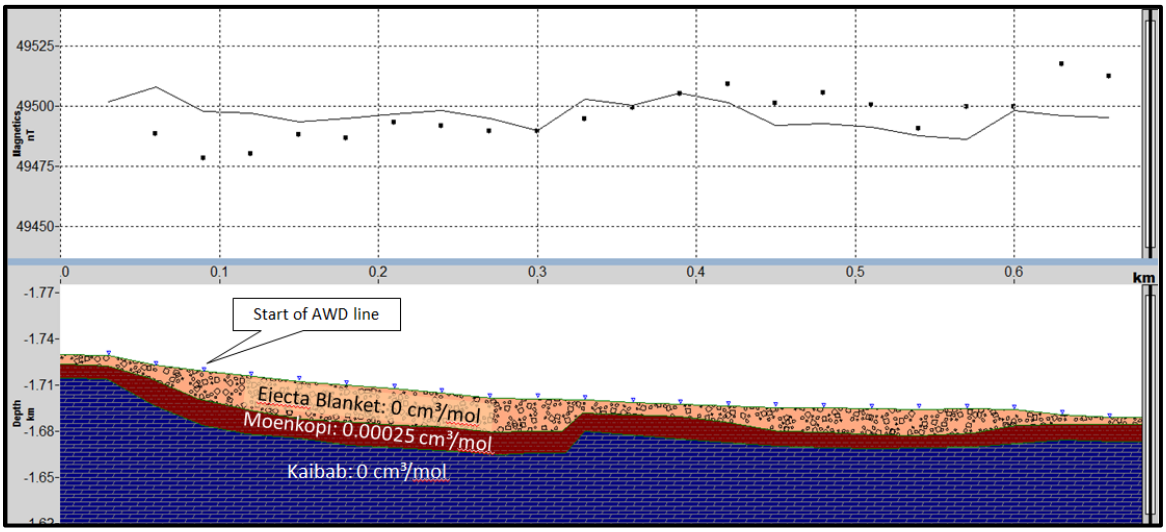

Fig. 3.22. Simple forward magnetic model of the subsurface along Line 1. Solid black and dotted lines represent the magnetic field response of the model and the actual magnetic field acquired at Meteor Crater, respectively. The magnetic misfit between the two is 11.5 nT.

According to Fig. 3.22, the magnetic misfit between the modeled and actual magnetic field is 11.2 nT. This disparity, about a quarter of the difference between the maximum and minimum value of the actual magnetic field, is quite large. However, such a disparity does not come as a surprise since the model constraints are poor: the magnetic susceptibility and remanent magnetization of each formation are not known accurately, the near-surface structure is not imaged well, numerous small meteoritic fragments that litter the near-surface are not considered, and the model is a 2-D solution to a 3-D problem. As a result, large disparities between the modeled and actual magnetic field exist. Nonetheless, the character of the modeled magnetic response does show some agreement with the actual magnetic field along the survey, albeit crudely.

In addition to modeling the magnetic field, a simple depth-to-source study was conducted using the half-slope (a.k.a. Peters) method to estimate the depth of the magnetic perturbations. The reader is referred to Blakely (1996) for a more detailed explanation of the methodology. Although many simplifying assumptions are required, the method is a valid rough estimate (Blakely, 1996). Using a proportionality constant of 1.6, the depths of the sources were determined to be between 10 m and 70 m with an average of 25 m. Since the sampling rate of the survey is likely too low to characterize magnetic sources within the ejecta layer, the majority of the perturbations are likely to be attributed to the Moenkopi formation, whose top is 20 m deep on average along the survey (Roddy et. al., 1975). The method also indicates that several deep sources (40-70 m deep) are likely responsible for the magnetic field between 200 m and 400 m along the magnetic survey. Although such deep sources are unanticipated, these larger-scale anomalies could be the result of the fault that is thought to be at 340 m along the gravity/magnetic surveys (250 m along the seismic line).

3.3 Joint Interpretation/Conclusions

The three data sets—seismic, gravity, and magnetic—were integrated to create a more meaningful picture of the subsurface and determine if the geophysical methods are in agreement. The results of the reflection seismic data indicate numerous sub-horizontal reflections, cross-cut by several possible faults. The dips of the reflections are not their true dip, but rather the result of the velocity structure of the subsurface. A simple model

was created to represent the subsurface and is in good agreement with the reflection seismic data. The refraction data suggest a low velocity near-surface closest to the rim associated with the ejecta blanket, Moenkopi, and Kaibab formations. The refraction data also indicate a thinning of this low velocity layer away from the crater rim, although the ejecta layer itself does not follow this trend. This disconnect could be indicative of the low velocity layer being highly dependent upon fracture density instead of lithology (i.e. ejecta layer).

Faults were interpreted on the final stacked seismic section where discontinuities seem present and large changes in velocity occur within the refraction analysis. The throw of these faults is not exactly known since they are near the resolution of the seismic data. Several of the interpreted faults on the reflection seismic section seem to coincide with velocity changes in the refraction analysis. Of particular interest is an interpreted fault at CMP 160 (240 m): there are noticeable discontinuities on the reflection seismic section at this location, which corresponds to a large velocity contrast on the refraction section. Faults from the reflection seismic section were overlaid on the velocity profile from the refraction data in Fig 3.23, which compares all three data sets on a common scale.

Gravity and magnetic surveys were acquired alongside, and in conjunction with, the seismic survey. The residual gravity anomaly along Line 1 was compared to the gravitational response of a near-surface model based on drill-hole data (Roddy et al., 1975), geologic studies (Kring, 2007), and the seismic surveys contained in this work. The model, with a gravity misfit of 0.175 mGal, supports the existence of a fault near 250

m along the seismic line, as seismic data suggest. The model also indicates possible thinning and thickening of the ejecta blanket away from the crater, as Roddy et al. (1975) indicates. However, because the gravity model in Fig. 3.12 is non-unique and suffers from acquisition and processing pitfalls, the model should be regarded as one of many possible solutions.

The magnetic field response from the near-surface model along Line 1 is in poor agreement (11.5 nT magnetic difference) with the actual magnetic field (Fig. 3.22). This poor correlation is likely due to poor subsurface constraints and limited data: hand samples were not collected for testing the magnetic properties of the formations, highly magnetic meteoritic material within the ejecta blanket cannot be properly characterized with a sampling rate of 30 m, the 2-D model is a solution to a 3-D problem, which may not be valid if the structure is not perpendicular to the survey, and the subsurface structure is not well imaged by the 2-D seismic line. Nonetheless, the character and amplitude of the modeled magnetic response is similar to that of the acquired magnetic field, implying that the data were acquired and processed appropriately. A simple depth-to-source study indicates that the majority of the sources responsible for the magnetic field are likely to be at a depth of 20-30 m below the surface, in agreement with Roddy et al.'s 1975 drill hole results for the top of the Moenkopi. In addition, the depth-to-source analysis indicates a deeper-than-expected source between 200 m and 400 m (100-300 m along the seismic survey), in the vicinity of the interpreted fault on the gravity and seismic surveys. Hence, the magnetic data complement the seismic and gravity surveys in suggesting that a fault or other complex structure exists in that area. Although the

residual magnetic anomalies of the radial lines in Fig. 3.21 do not indicate an extensive magnetic anomaly like the gravity lines in Fig. 3.9 indicate a concentric gravity anomaly, it is not proof that one does not exist. It may simply indicate that the magnetic field is highly sensitive to ferrous meteoritic material in the ejecta blanket and is therefore less robust in this application.

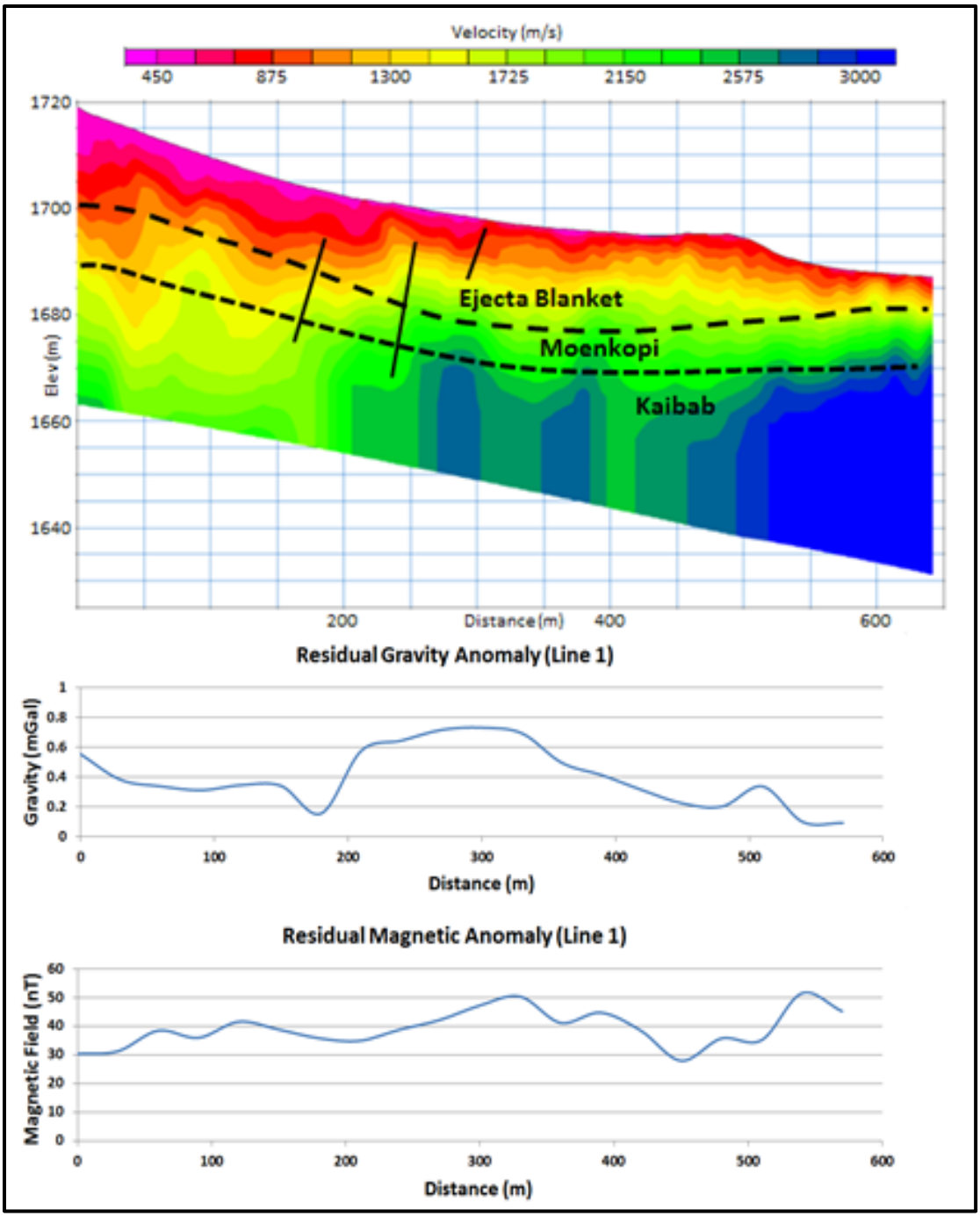

Fig. 3.23. A comparison of the velocity profile from the tomographic refraction analysis (top), residual gravity anomaly of Line 1 (middle), and residual magnetic anomaly of Line 1(bottom). The gravity and magnetic lines are truncated in order to simplify the comparison between the seismic and potential field data.

This study has not only served as a stepping stone for future geophysical surveys at Meteor Crater , but has also served as a test of the capability of modern geophysical techniques and tools in understanding cratering processes. Although much has been learned through the acquisition, processing, and interpretation of these data sets, this study has also shed light on the limitations of these techniques: to obtain a more complete picture of the near-surface at Meteor Crater, more sophisticated and comprehensive data will be needed, namely, 3-D seismic, gravity, and magnetic data. Depending on the objective of future surveys, gravity and magnetic gradiometry surveys as well as other geophysical tools such as GPR may be needed to image shallow complex structures in the subsurface of craters. As is often the case, more data would lead to a clearer picture.

Chapter 4

Pueblo of Jemez, NM

4.1 Introduction

4.1.1 Area of Study

The Jemez Pueblo geophysical survey was conducted on the Pueblo of Jemez Indian reservation in northern central New Mexico. More precisely, the study area is located just west of U.S. highway 4 and east of the Jemez River near the Indian Springs well on Day School Road, about 1 mile south of the main reservation (Fig. 4.1). The area is in the southwestern region of the volcanic Jemez Mountains, 23 miles southwest of the Valles Caldera.

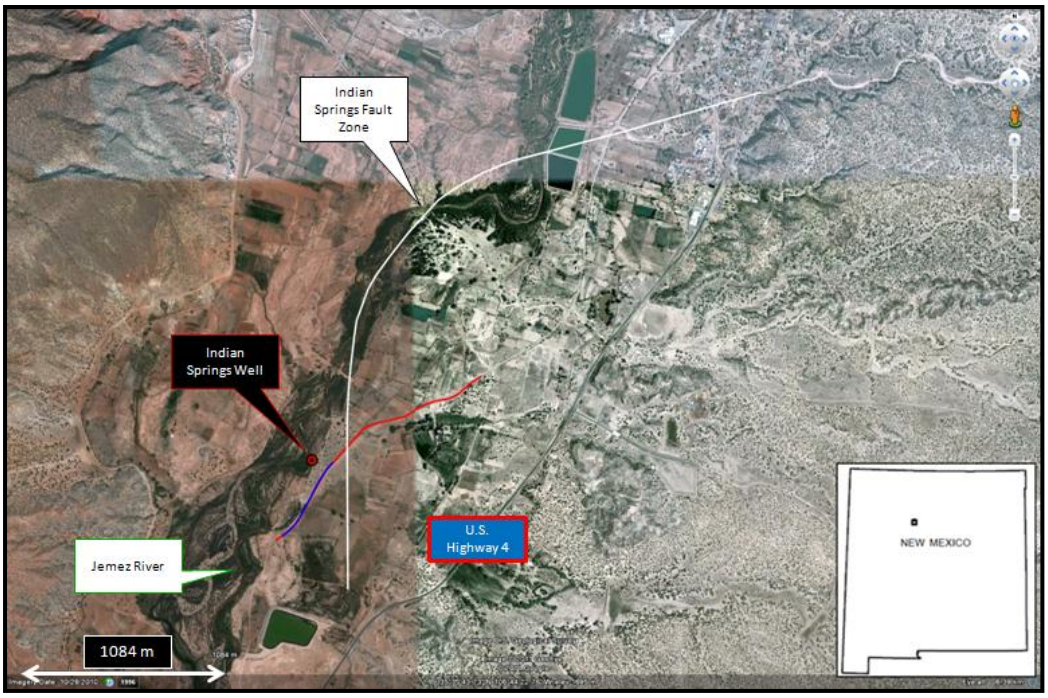

Fig. 4.1. Google Earth image of Pueblo of Jemez geophysical study area. Blue line indicates extent of seismic survey. Red line denotes extent of gravity survey. Other important features nearby are also labeled. Inset picture shows location of survey area in New Mexico.

4.1.2 Geologic Background

The survey area, near the Jemez volcanic field, is located above the intersection of the north-south Rio Grande Rift and the northeast-southwest Jemez volcanic lineament (Heiken and Goff, 1983). Geologic studies indicate a thinning of the crust due to tectonic rifting, causing an upwelling of magma close to the surface and heating near-surface waters to temperatures of up to 72°C, resulting in numerous hot springs in the area (Huang and Albrecht, 2011). The geophysical study area is mainly characterized by Paleozoic and Mesozoic sedimentary rocks. From youngest to oldest, the formations include the topmost Miocene Zia "sand" Formation (part of the Santa Fe Group), the

well-known Triassic Chinle and Moenkopi Formations, and the Permian Glorieta, Yeso, Abo, and Madera Formations, all of which are underlain by Precambrian igneous and metamorphic basement rocks. For a more comprehensive summary of the stratigraphy, the reader is referred to Black and Hiss (1974).

The tectonically active rift zone is also characterized by numerous steep (mainly normal) faults. The previously mapped major faults in the area are the Jemez, Indian Springs, and Vallecito Creek fault zones; a detailed east-west geologic cross-section near the survey area is shown in Fig. 4.2. Although the distribution of these main faults is well understood, other lesser-known faults may also exist in the area. Since hydrothermal migration pathways via faults, and therefore the geothermal potential of the area, cannot be properly determined without first understanding the geologic structure of the subsurface in detail, a study such as this is necessary.

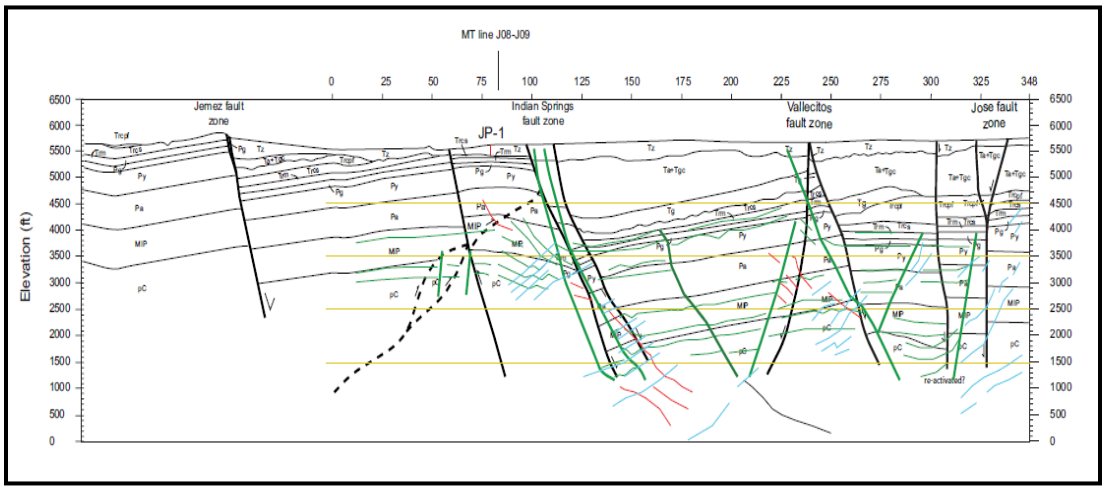

Fig. 4.2. A west to east (left to right) geologic cross-section through the Jemez, Indian Springs, Vallecito Creek, and Jose Fault Zones. Faults in black are those identified from other studies while those in color are from Huang et al. (2011).

4.2 Synthetic Modeling

Like the Meteor Crater study, a model of the subsurface based upon previous geological and geophysical work in the area was created to simulate the expected seismic results. Since the Indian Springs Fault zone was not traversed, a simple model, shown in Fig. 4.3, was created. The model shows 8 distinct formations (including the Precambrian basement rock) dipping slightly to the south (left) at an angle of about 5°. The layers' gross rock properties, obtained from well logs from a well about 17 miles southeast of the area of study, are also shown in the figure.

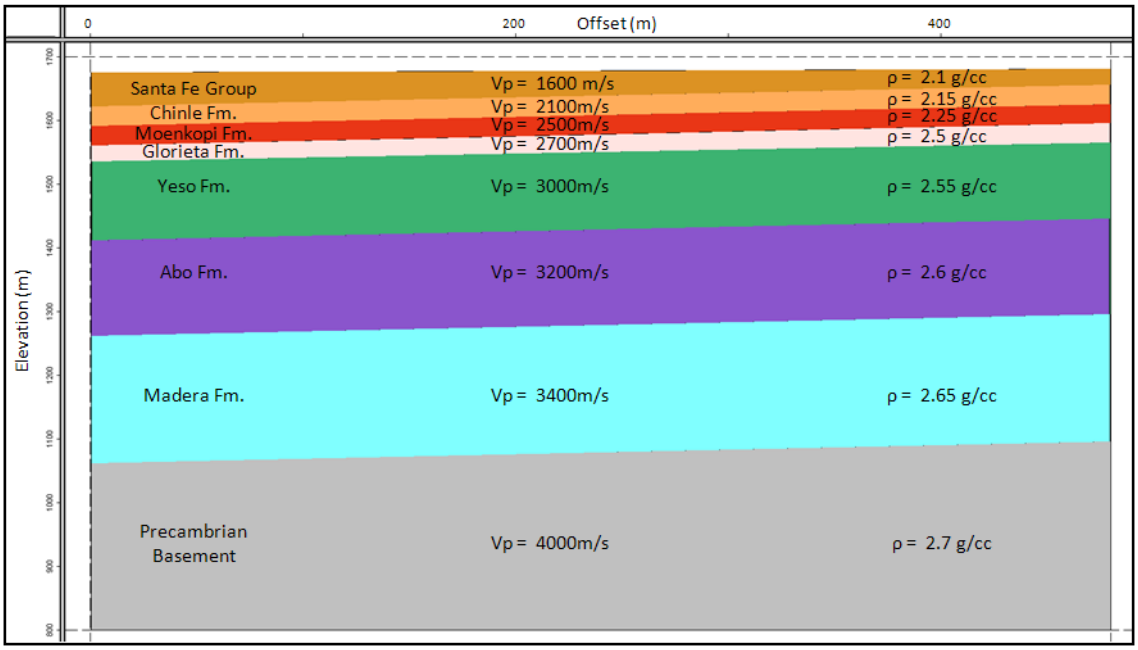

Fig. 4.3. Simple synthetic model of the subsurface beneath the seismic survey at Jemez Pueblo, NM. The various formations and their P-wave seismic velocities and densities are shown. The y-axis shows elevation from 800 to 1700 m.

Acoustic ray tracing of the model was then performed to better understand the reflection hyperbolae that may result from the acquired data (Fig. 4.4). The results also

give an indication of the estimated time of arrival of the reflections from their respective reflectors, which are not expected to be beyond 500 ms. A depth-to-time conversion of the model, shown in Fig. 4.5, demonstrates similar results: reflections beyond 500 ms are not expected.

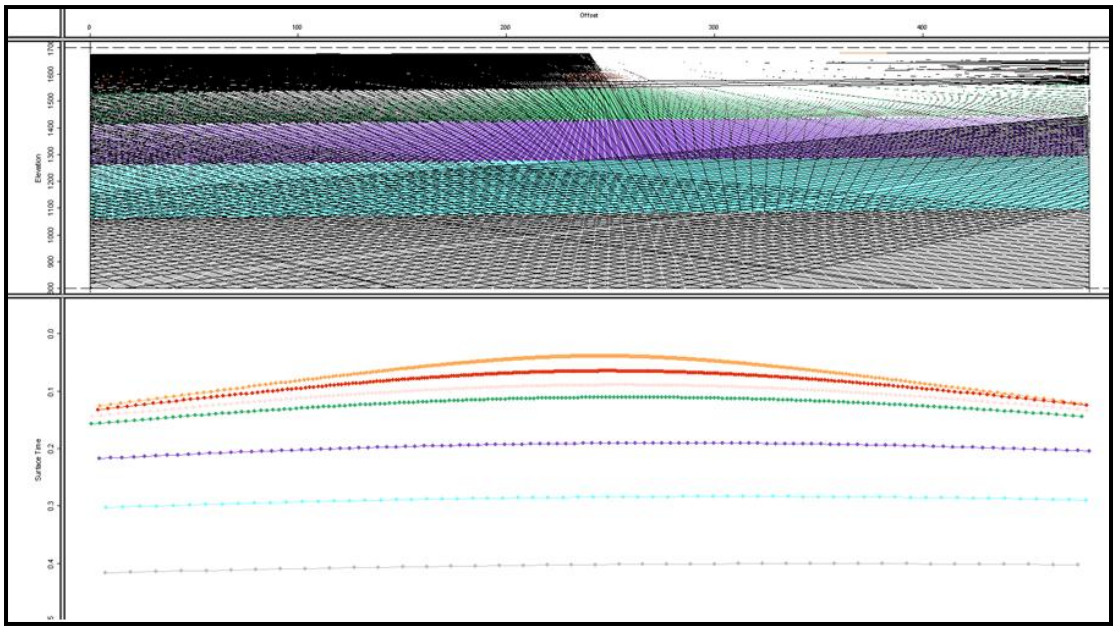

Fig. 4.4. Ray tracing results (bottom) of the simple model shown in Fig. 4.3 (top).

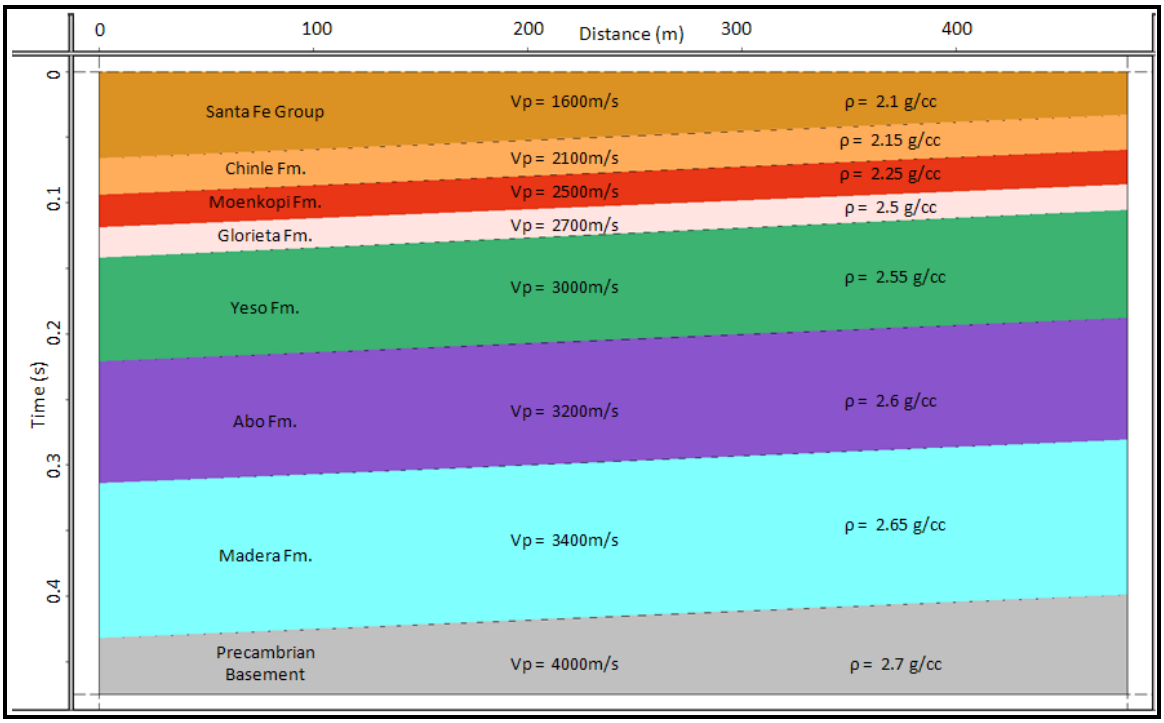

Fig. 4.5. Depth-to-time conversion of the Jemez Pueblo model shown in Fig. 4.3.

4.3 Seismic Analysis

4.3.1 Acquisition

The Jemez Pueblo seismic survey consists of a single 475 m long vertical component 2-D seismic test line. The line was composed of 96 field stations, 24 of which were rolled from the beginning of the line to the end after the shot location reached the end of the first line of 72 geophones. Station spacing remained constant throughout the line at 5 meters. Receiver station 1 marked the beginning of the line and was located at 0 m. The shots, consisting of weight drops from the back of a pick-up truck, were located in between each pair of consecutive receivers and 1 m to the side of the seismic line. The

shot line began off-end about 2.5 meters before the first receiver and continued at a 5 m interval until the last shot, located between receivers 83 and 84, was recorded. A total of 86 shots were recorded. Each shot gather is composed of three shots which were automatically stacked in the field. Fig. 4.6 shows a schematic of the acquisition geometry.

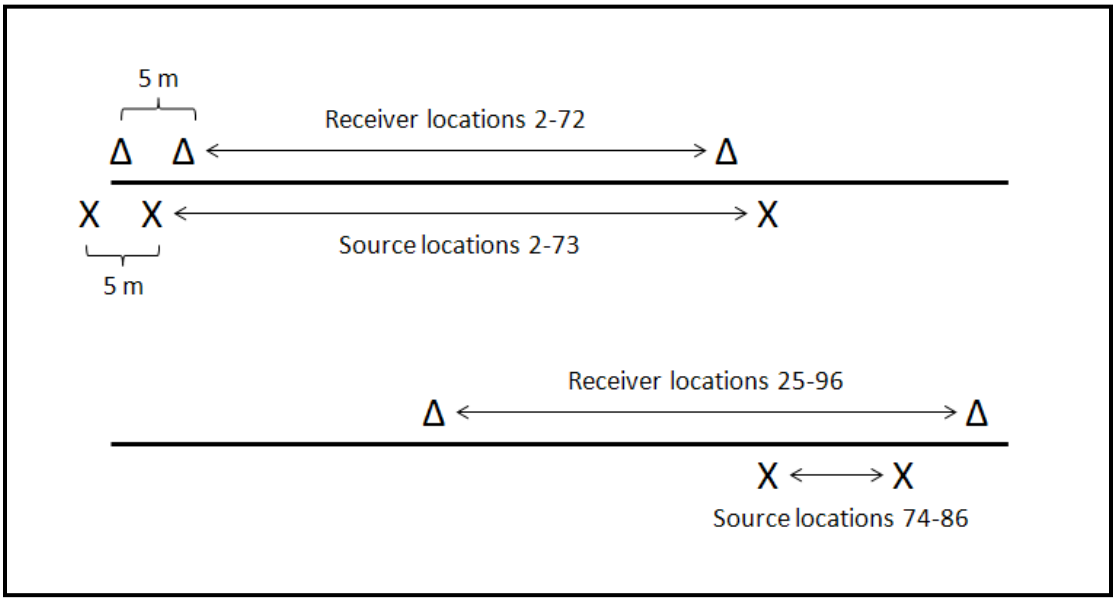

Fig. 4.6. Geometry of the Jemez Pueblo seismic line. Because of the availability of only 72 geophones, the first 24 were rolled to the end of the line to increase the total length of the survey. A total of 86 shots were recorded with 96 live receiver stations. Shot and receiver spacings were each 5 m.

The initial plan of the survey was to roll the receiver line several times to cross the Indian Springs Fault Zone and obtain sufficient subsurface CMP coverage to image the fault. However, accessibility problems, time constraints, and technical difficulties during acquisition resulted in a seismic line that was acquired just short of the fault zone. Fig. 4.7 shows the extent of the seismic line via satellite imagery using Google Earth. It is

clear from the figure that the seismic data were acquired about 100 m short of the fault zone. Nonetheless, the seismic data were processed and interpreted to broaden our understanding of the subsurface in the area. After all, the seismic survey was intended as a test line of the near-surface, not a comprehensive study of the fault zone.

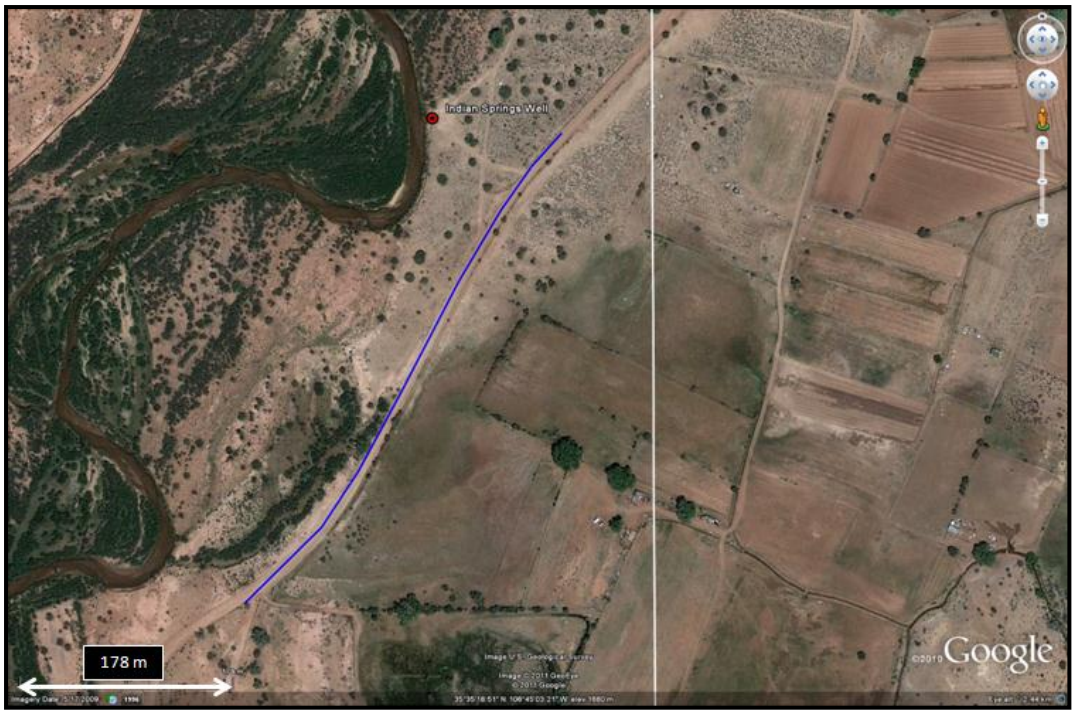

Fig. 4.7. A satellite image of the Jemez Pueblo seismic survey area. Blue and white lines denote the Jemez Pueblo seismic line and the Indian Springs Fault Zone, respectively.

4.3.2 Processing

A simple yet sufficient processing workflow was performed on the seismic data using two seismic software packages: Gedco's Vista and Paradigm Geophysical's Focus. Fig. 4.8 outlines the processing workflow utilized in processing the Jemez Pueblo seismic line.

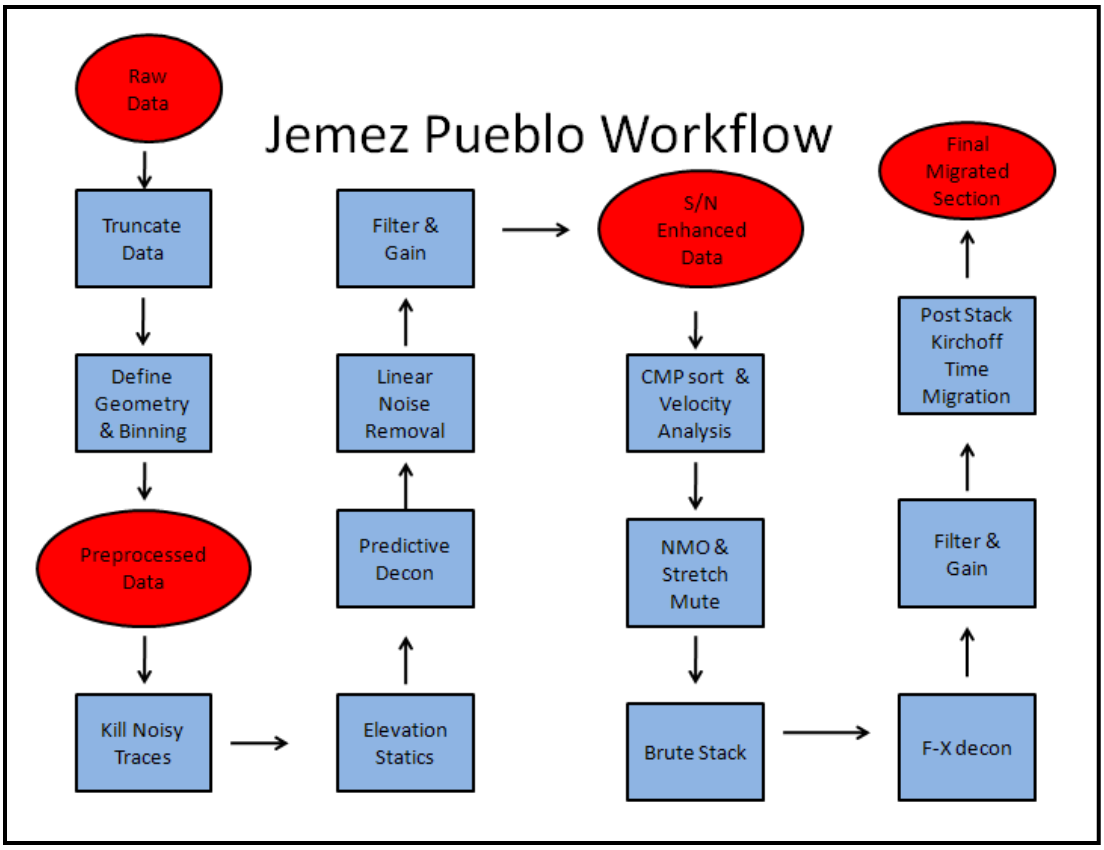

Fig. 4.8. Seismic processing workflow applied to the Jemez Pueblo seismic data.

The first step in the workflow was to input and truncate unused data. Fig. 4.9 shows shot gather 41 before data truncation. It is evident that beyond 1000 ms, the data consists mainly of ground roll and other random noise. In addition, reflective energy from a weight drop is not expected to be recorded beyond this time. Thus, all data beyond 1000 ms were deleted. This step decreased computing time in later processing steps and diverted the processor's attention away from noisy data.

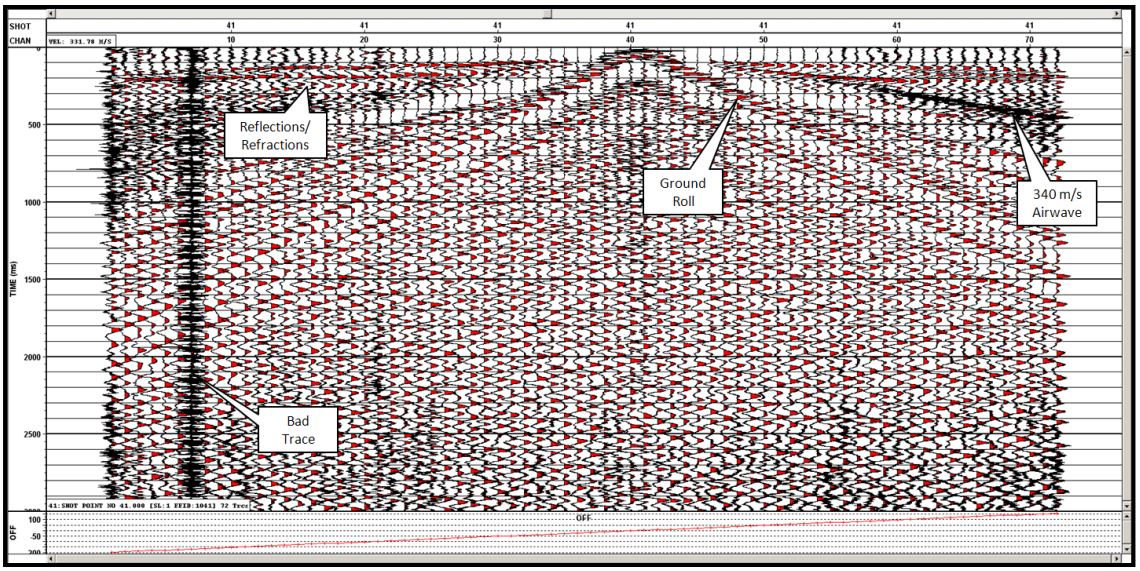

Fig. 4.9. Raw seismic shot gather 41 with a 200 ms AGC window applied. The ground roll, airwave, refractions/reflections, and a bad trace are annotated. No discernible reflective energy exists beyond 1000 m on this raw shot gather.

Next, the source and receiver geometries of the survey were defined based upon the acquisition parameters specified in section 4.3.1 (Fig. 4.10). The survey was then binned and the CMP fold was calculated. Because all geophones were live during each shot and the line was rolled once, an atypical CMP fold resulted (Fig. 4.11). With a CMP bin of 2.5 m, the maximum CMP fold recorded was 73 and the minimum was 1. A first pass examination of the data was then conducted to identify any problems and to quickly analyze it for coherent noise and reflections. Fig. 4.12 shows the main features found in a preprocessed shot gather.

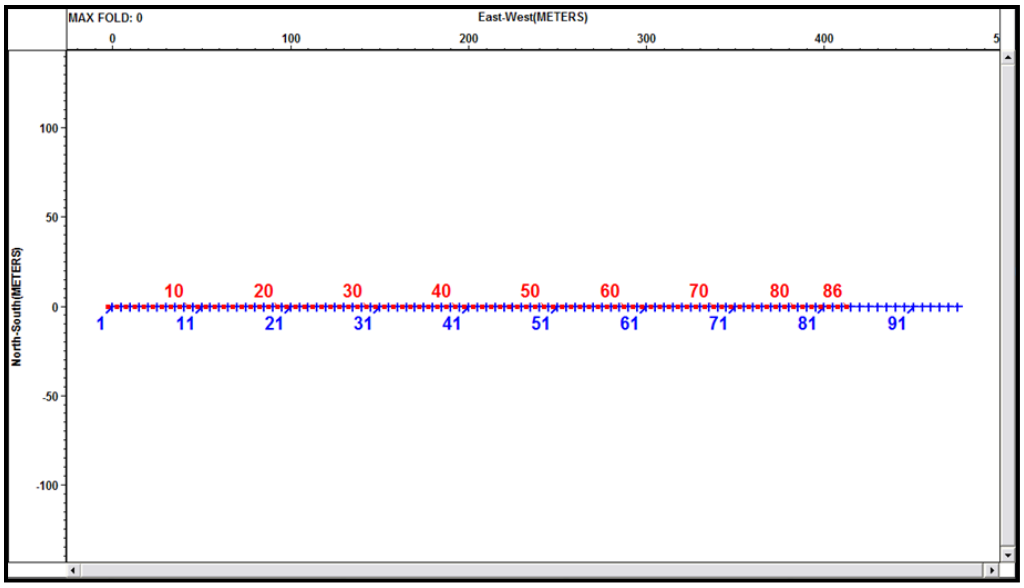

Fig. 4.10. Source and receiver geometry of seismic line at Jemez Pueblo. Red squares and blue crosses represent shot and receiver locations, resepectively.

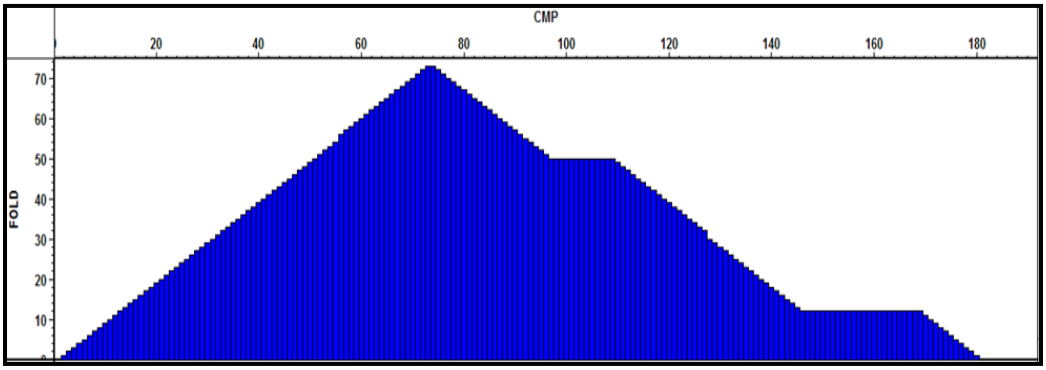

Fig. 4.11. CMP subsurface fold of seismic line at Jemez Pueblo. Atypical fold geometry results from rolling part of the line and keeping all geophones live during acquisition. Maximum CMP fold is 73.

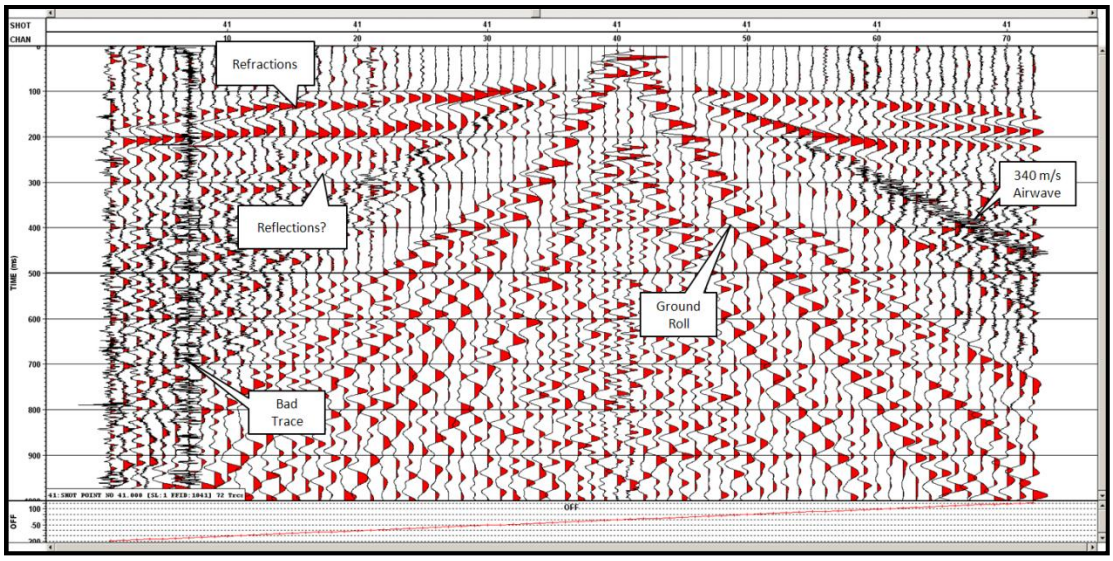

Fig. 4.12. Truncated raw seismic shot gather 41 with a 200 ms AGC gain applied. The ground roll, airwave, refractions, possible reflections, and a bad trace are identified.

A first pass of the data was not encouraging. Numerous noisy traces exist in the raw data as a result of windy conditions, poor coupling, broken geophones, and crew/vehicles moving along the line during acquisition. In addition, although coherent high amplitude events in the near surface are evident, it is not clear whether they are reflections or refractions. Also, no clear coherent reflections are evident within the noise cone, prohibiting reflections from one side of the shot gather to be followed to the other unequivocally. A frequency analysis of the data also showed that the data residing in the noise cone contains frequencies similar to those of the refractions and reflections. Thus, a simple band-pass filter would not be able to separate the ground roll from the reflections, as in other studies (Kaiser et al., 2009). A more precise spectral analysis indicated that the reflected/refracted signals lie in the 20-120 Hz band (Fig. 4.13).

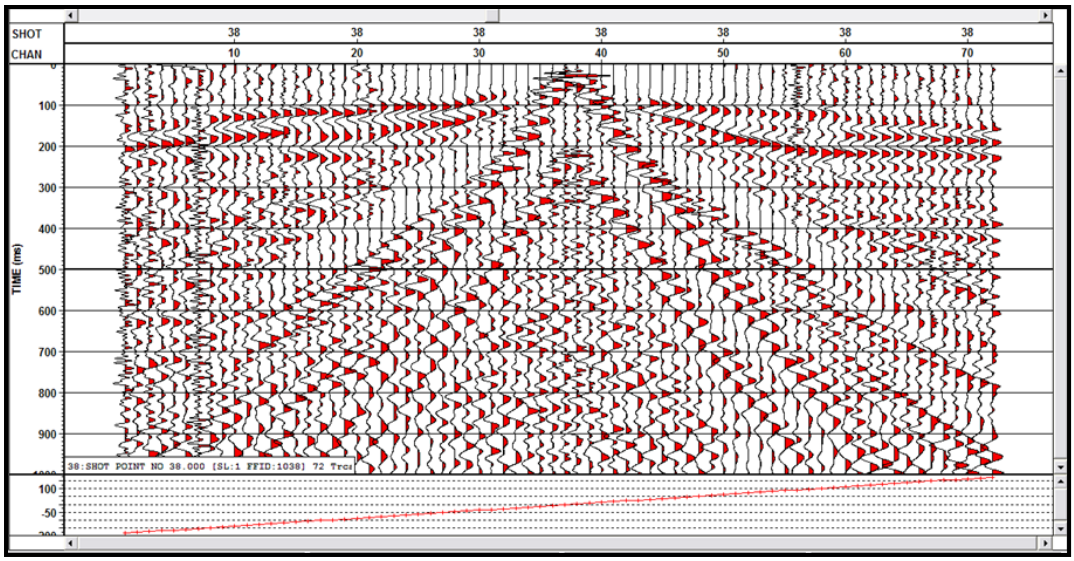

Fig. 4.13. Shot gather 38 with a 200 ms AGC gain and 10-125 Hz band-pass filter to highlight signals of interest.

Next, noisy traces were marked dead and killed to improve the signal-to-noise ratio (S/N) of the data. This proved to be an important step in the processing effort since numerous traces were contaminated by external noise and reduced the overall S/N. Fig. 4.14 shows an example of random noise contamination within a shot gather that was removed.

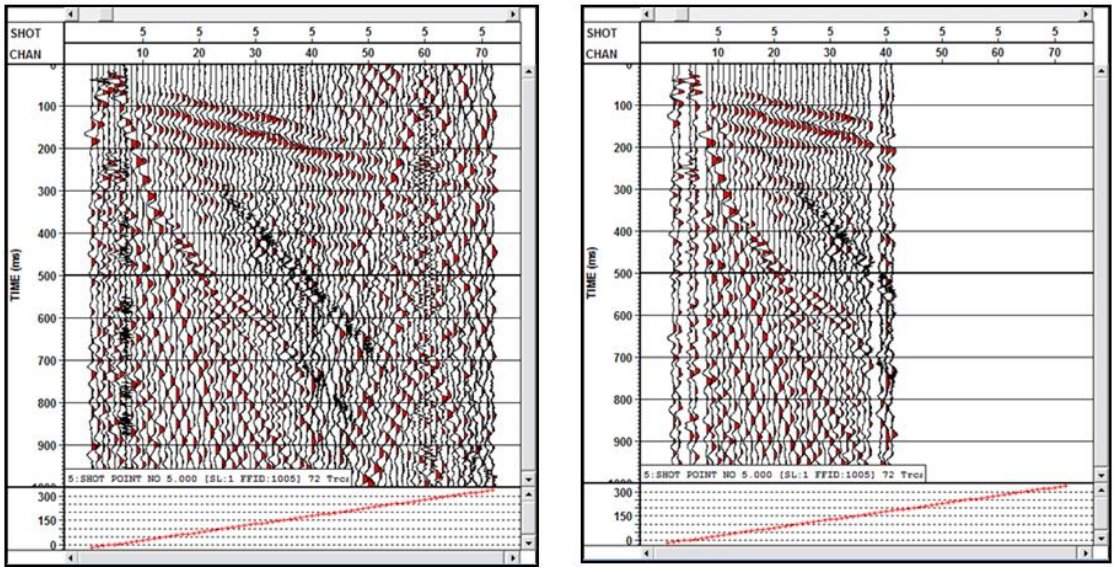

Fig. 4.14. Shot gather 5 with a 200 ms AGC gain applied (left). Same shot gather with noisy traces killed (right).

The next step in the seismic processing workflow, statics corrections, was carried out to gain a better understanding of the near-surface velocity structure and compensate the data for weathering zone heterogeneities. Unlike refraction statics, however, elevation statics were not applied since the topography was not variable along the seismic survey.

The first step in the refraction analysis involved picking first breaks. Next, the first breaks were utilized to estimate the velocity of the direct wave from each shot location to the nearest several geophones. A 1-dimensional model of the direct wave velocity profile is shown in Fig. 4.15. This information was used in choosing an accurate weathering layer velocity in the next step as well as creating a starting point in forming a picture of the subsurface. From Fig. 4.15, it is evident that the shallowest several meters of sediment is loosely consolidated and dry, based on velocities ranging from 340 m/s to 460 m/s. Rapid changes in velocity over short distances (upwards of 60 m/s over a

distance of 40 m) suggest that the subsurface is heterogeneous and complex. Using an average velocity of 400 m/s as the weathing zone velocity, a two-layer model of the subsurface was then created (Fig. 4.16). The model is more complex than initially suspected: a depression resembling a river channel or graben is evident in the middle of the survey and velocities within the 2nd layer tend to increase near the depression. Using these results, the long-wave refraction statics were computed and applied to the data (Fig. 4.17). The refraction results are a first indicator of a complex near-surface that will serve as a starting point for processing and interpreting the reflection seismic data.

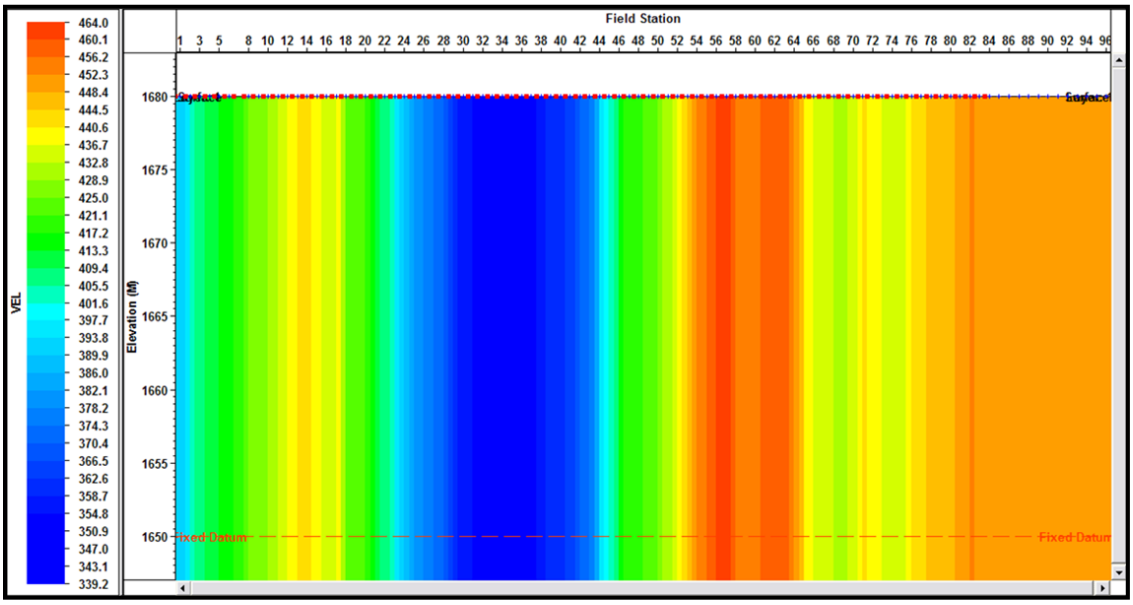

Fig. 4.15. A single layer 1-D model of the direct arrival velocities based on first break picks of refractions from the Jemez Pueblo seismic survey.

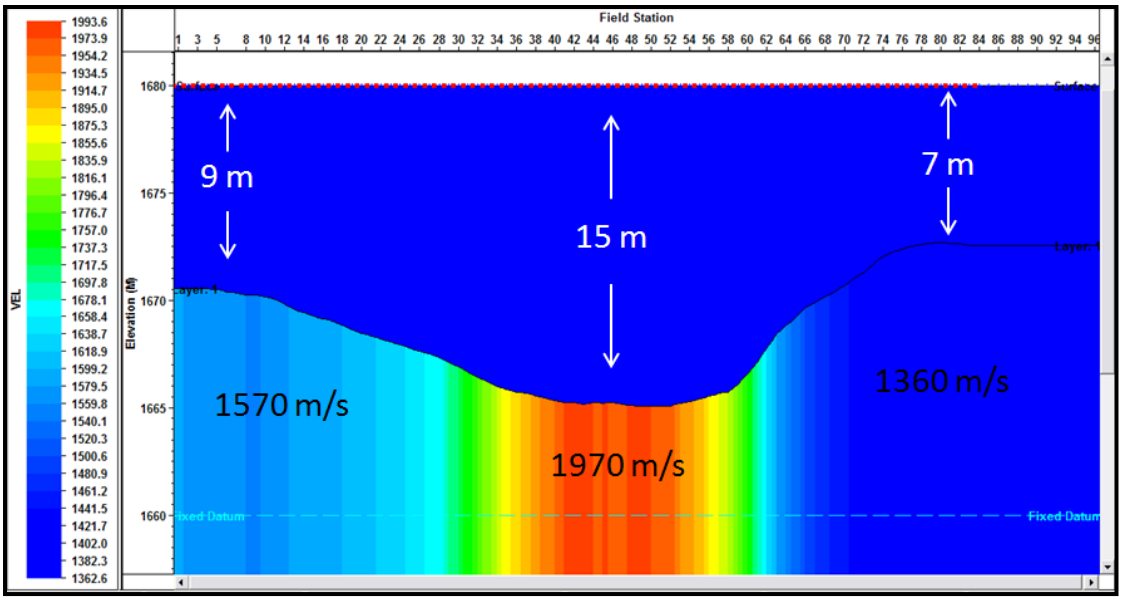

Fig. 4.16. A two layer model of the near-surface at Jemez Pueblo based on refraction data. An average weathering layer velocity of 400 m/s was used based on direct arrival results. The thickness of the weathering layer along the seismic line is shown along with the varying velocity of the 2nd layer.

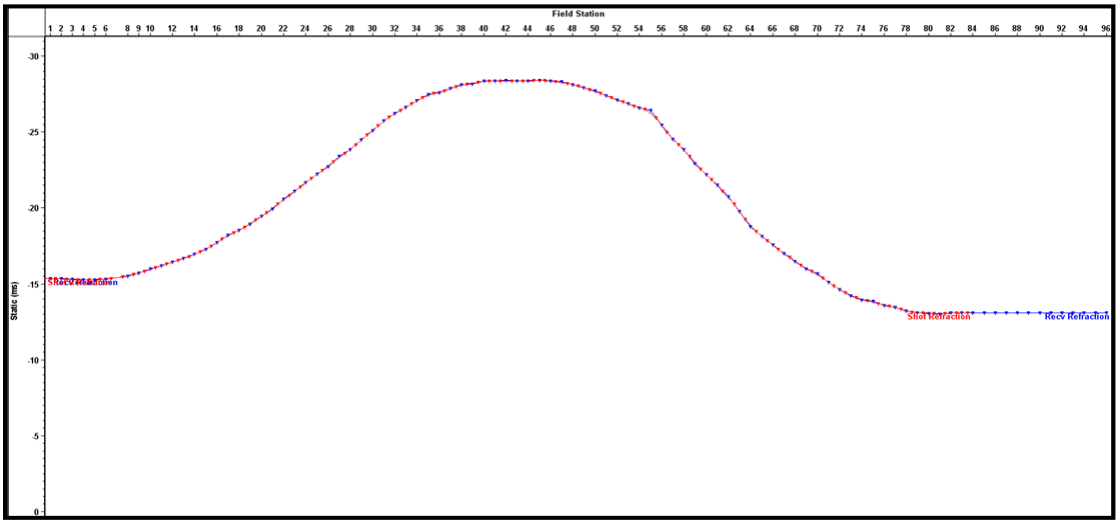

Fig. 4.17. Long-wave refraction statics applied to Jemez Pueblo seismic data. Red and blue points represent source and receiver statics, respectively. The statics increase in the middle is due to the depression-like feature in Fig. 4.16. The maximum difference in applied statics is about 20 ms. X-axis represents field station (1-96) and the y-axis represents the static correction (0-30 ms).

The same justification in applying predictive deconvolution to the Meteor Crater data set was used in applying the process to the Jemez Pueblo seismic data; specifically, to increase the vertical resolution of the seismic data and to predict and attenuate multiples. The operator length of the predictive decon was 100 ms and the prediction lag was 10 ms. Fig. 4.18 and Fig. 4.19 show shot gather 40 before and after predictive decon and their respective frequency analyses. The figures indicate that deconvolution increased the frequency bandwidth of the data and spiked the coherent signals.

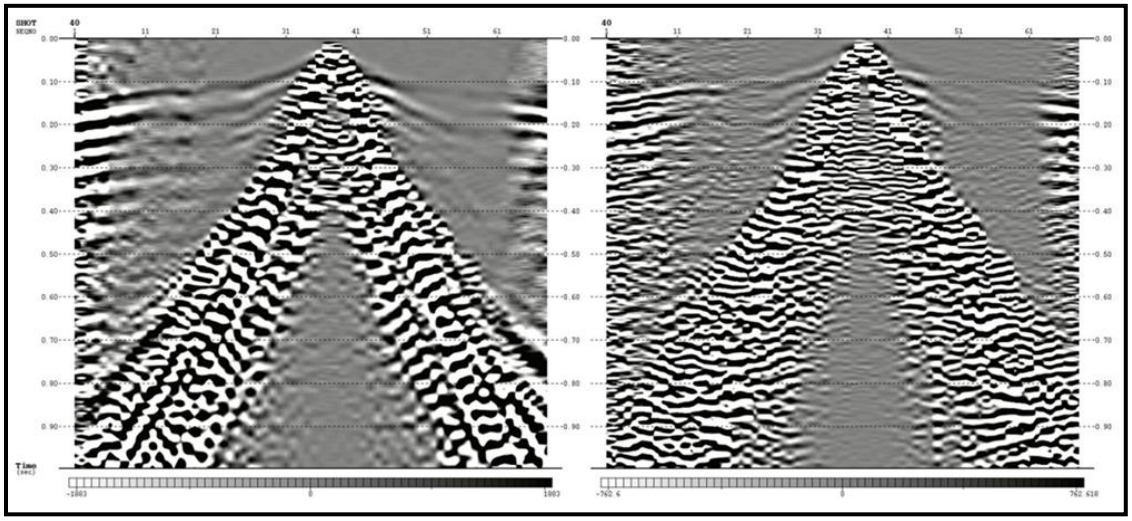

Fig. 4.18. Shot gather 40 with a 200 ms AGC window applied before and after predictive decon (left and right, respectively). The x-axis is trace number (1-70) and the y-axis is time (0-1 s).

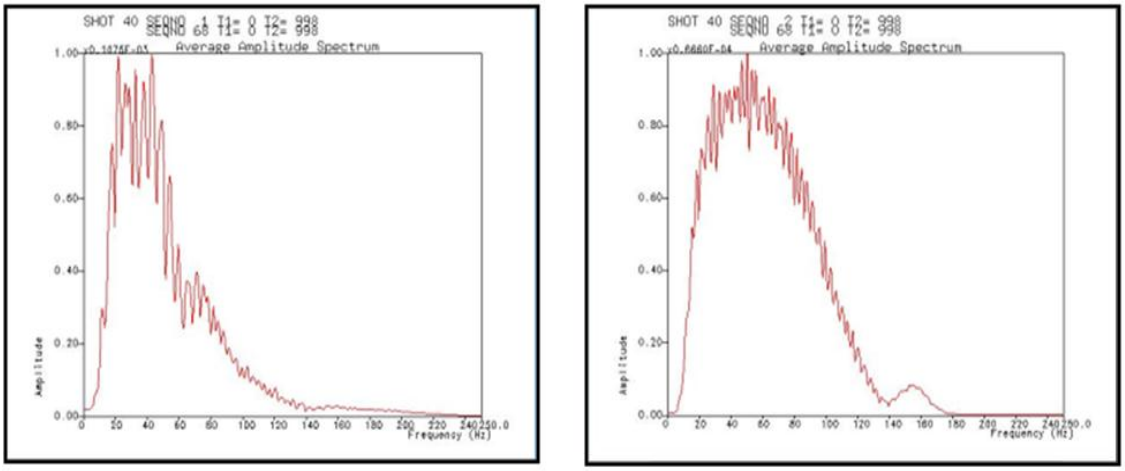

Fig. 4.19. Frequency spectra of shot gather 40 before and after predictive decon (left and right, respectively).

To further increase the S/N of the data, the next step involved reducing or muting known coherent noise such as refractions and ground roll. Several LMO filters of up to 900 m/s were applied to remove some of the low frequency ground roll within the noise cone. Next, a top mute was devised to remove probable refractions and other random noise occuring above the refractions. Fig. 4.20 shows the effect of the linear noise removal and top mute.

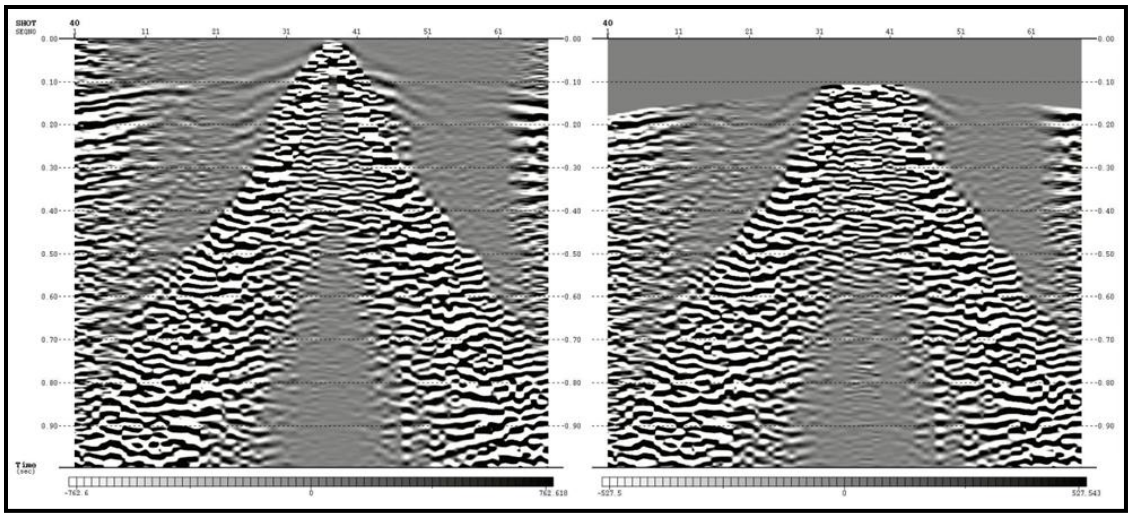

Fig. 4.20. Shot gather 40 with a 200 ms AGC window applied before linear noise removal (left). Same shot gather with LMO filters and top mute applied to remove refractions and other coherent noise (right). The x-axis is trace number (1-70) and the y-axis is time (0-1 s).

The LMO filter only removed linear events with a maximum velocity of 900 m/s to prevent the removal of reflected signals that may appear linear. Since the LMO filter introduced some low frequencies to the data, a 30-190 Hz band-pass filter was applied before a top mute was implemented. The mute itself is a simple concept, yet discerning coherent noise (refractions) from near-surface reflections was a much more difficult task and great care was taken to include only the most probable refractions within the mute.

To help bring out reflections within the noise cone, a frequency-wavenumber (f-k) filter corresponding to about 800 m/s was applied. Although f-k filtering may be problematic if data are aliased, the short spacing between receivers (3 m) and fast sampling rate (0.5 ms) minimized this phenomenon. Fig. 4.21 and Fig. 4.22 show the f-k filter in the shot domain and the effect of the filter on a shot gather along the Jemez Pueblo seismic line, respectively.

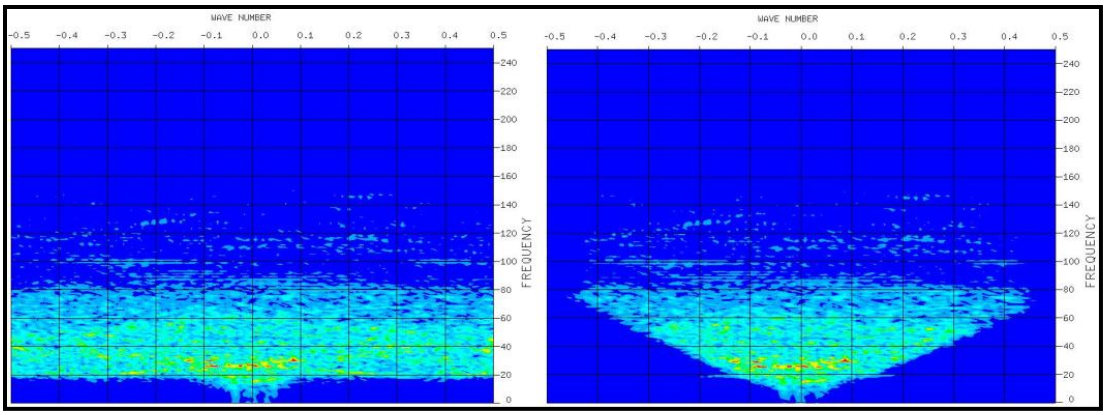

Fig. 4.21. F-k spectra before (left) and after (right) an f-k filter was applied to the Jemez Pueblo seismic line in the shot domain. X-axis is wavenumber (-0.5 to 0.5) and y-axis is frequency (0-250 Hz).

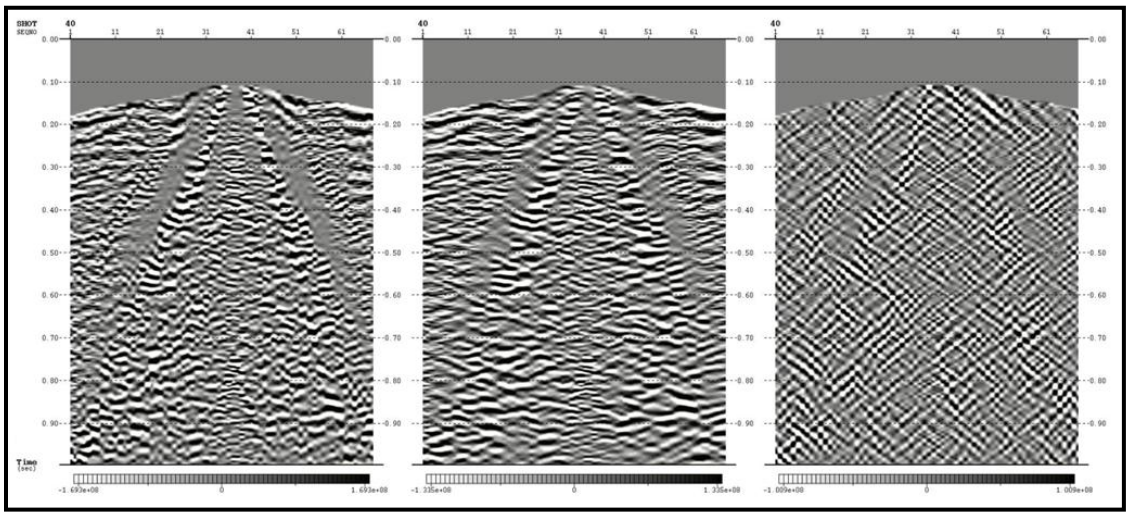

Fig. 4.22. Muted shot gather 40 with a 200 ms AGC window applied (left). Same shot gather with an f-k filter applied (middle). Data removed by the f-k filter is shown in the image on the right. The x-axis is trace number (1-70) and the y-axis is time (0-1 s).

After filtering, the S/N of the data was optimized and the data were sorted by CMP. A velocity analysis was then performed. First, numerous constant velocity stacks (CVSs) were created to gain a sense of the average velocity of the near-surface since semblance plots can be misleading. Fig. 4.23 shows three such CVSs: 1500, 2000, and

2500 m/s. With a better understanding of the velocity structure, NMO velocities were fine-tuned by using semblance plots and sorted CMPs: velocities were picked every 10 CMPs and the resulting smoothed velocity profile is shown in Fig. 4.24. The CMPs were then NMO corrected and a stretch mute of 30% was applied.

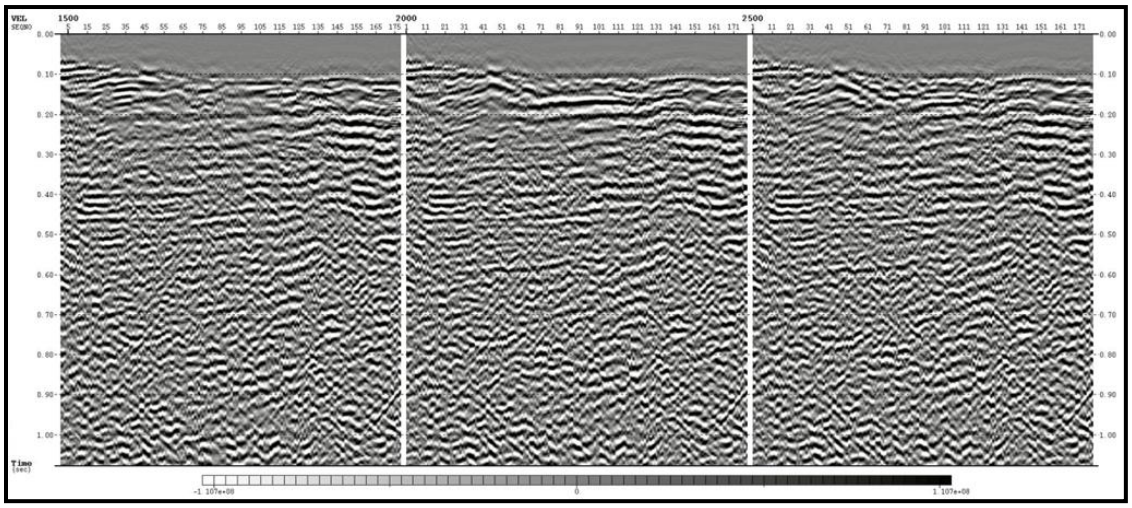

Fig. 4.23. Constant velocity stacks of Jemez Pueblo seismic survey: 1500 m/s (left), 2000 m/s (middle), and 2500 m/s (right). X-axis is CMP (1-178) and y-axis is time (0-1 s).

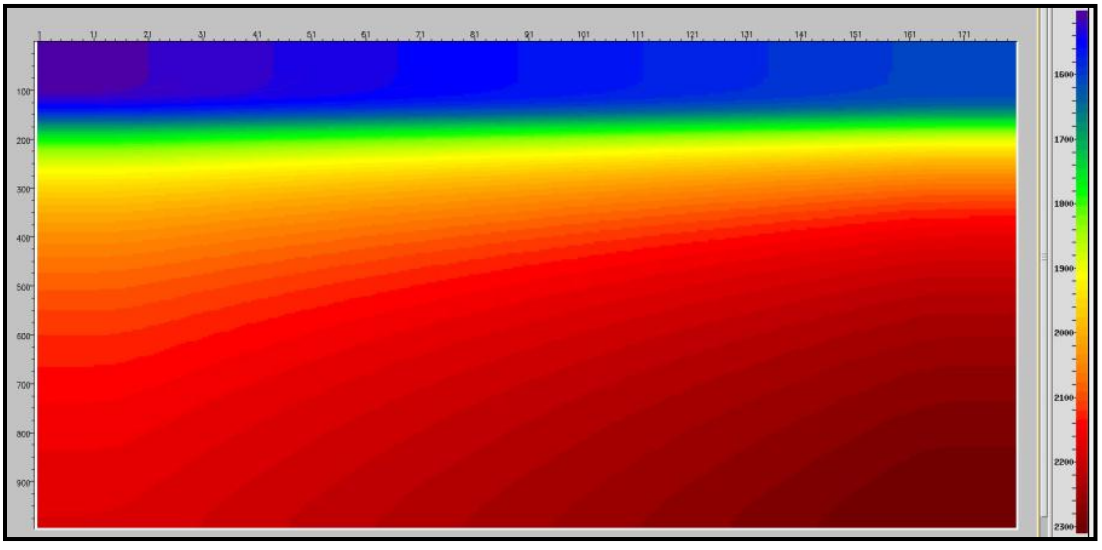

Fig. 4.24. RMS velocity profile of Jemez Pueblo seismic survey. X-axis is CMP (1-180) and y-axis is time (0-1 s). Seismic P-wave velocity varies from 1,500 m/s (blue) to 2,300 m/s (red).

The RMS velocity profile shown in Fig. 4.24 tends to increase with depth, as expected, and increases slightly from left to right, which may be due to slightly dipping beds. The NMO-corrected CMP gathers were then stacked (Fig 4.25). To enhance the brute stack, a 40-190 Hz bandpass filter and an 80 ms frequency-distance (f-x) filter were then applied (Fig 4.25). Finally, a post-stack Kirchoff time-migration with a 10 CMP aperture was implemented to increase the spatial resolution of the stacked section and collapse any diffractions (Fig. 4.26). An interpretation of the results is completed in the following section.

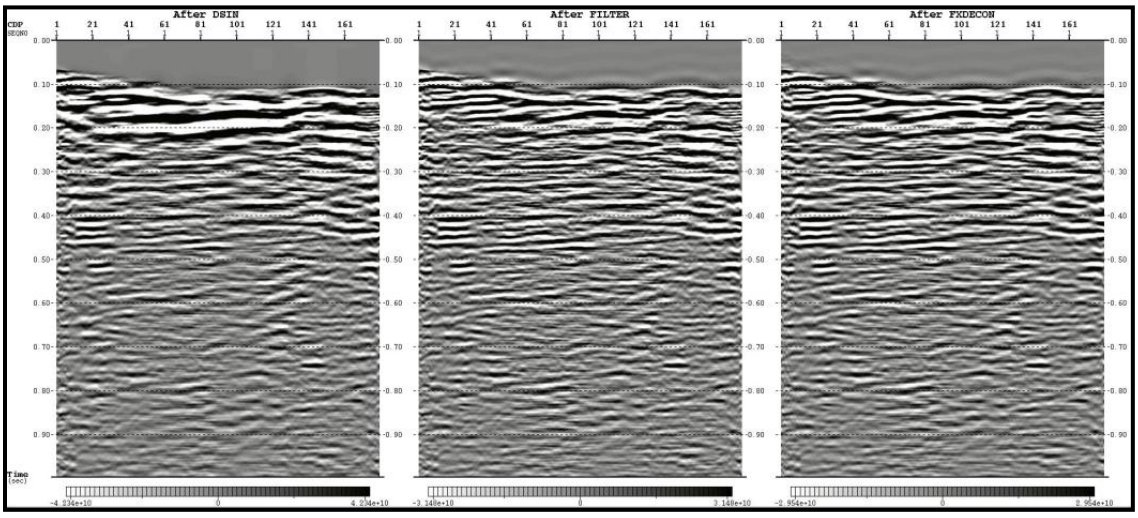

Fig. 4.25. Brute stack of Jemez Pueblo 2-D seismic line (left). Same seismic section after 40-190 Hz band-pass filter (middle). Same seismic section after band-pass filter and f-x deconvolution (right).

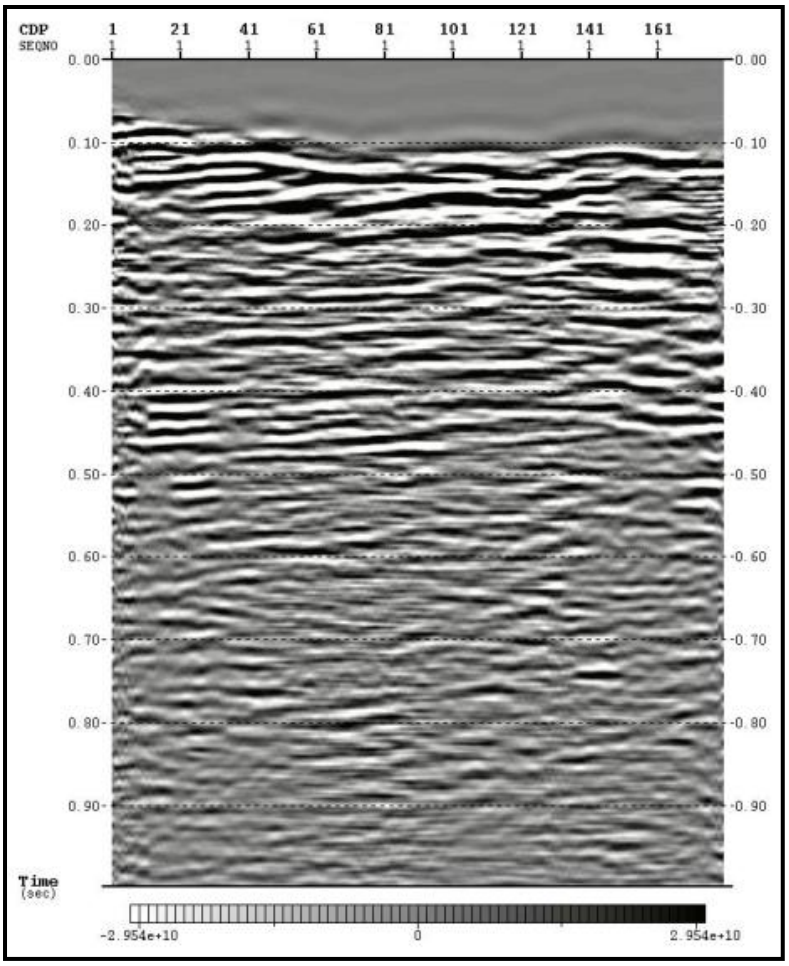

Fig. 4.26. Post-stack Kirchoff time migration of Jemez Pueblo seismic line with 200 ms AGC applied.

4.3.3. Interpretation

Fig. 4.27 represents an interpretation of the final seismic cross-section shown in Fig. 4.26. Several prominent reflectors were picked below 200 ms on the seismic section (it is likely that the coherent signals above 200 ms are refractions and were therefore ignored in the interpretation). The interpreted beds seem to be dipping slightly to the south (left) and are in agreement with results found by Huang and Albrecht (2011). It is

also clear from the seismic section that deeper reflectors (greater than 600 ms) are more poorly imaged, as one would expect.

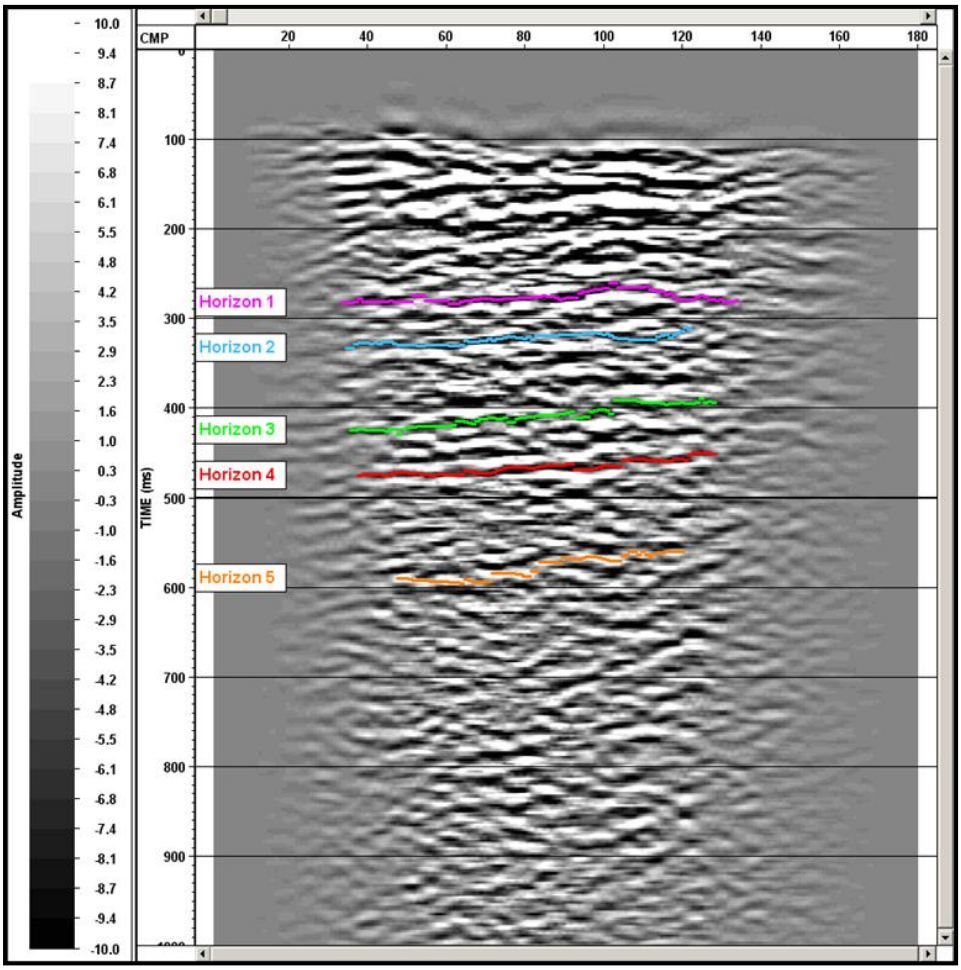

Fig. 4.27. Interpreted post-stack Kirchoff time migrated section. Several prominent reflectors were picked. It is clear that the dominant dip of the reflectors is to the south (left). AGC is not applied.

Five horizons were picked along troughs of 5 reflections on the final stacked seismic section. They were chosen based upon their extent, high amplitude, and coherency, and are most likely the results of major lithologic boundaries. Horizon 1 may correspond to the top of the Yeso Formation, horizon 2 to the top of the Abo, horizon 3 to

the top of the Madera, and horizon 4 to the top of the Precambrian basement rock. Horizon 5 may be a multiple or other noise. This correlation, however, is speculative at best and is mainly the result of the depth-to-time conversion of the simple subsurface model (Fig. 4.5) Well logs from a nearby offset well are necessary to create an accurate stratigraphic correlation.

The reason why so few reflectors are imaged well below 500 ms is most likely due to both the acquisition equipment and local geology: the 40 kg accelerated weight drop source has a relatively shallow depth of penetration and the simple model of the expected subsurface shows the basement rock to be about 700 m below the surface, which corresponds to a two-way time of no more than 500 ms, or near horizon 4.

The depression feature seen in the refraction analysis is not evident in the reflection seismic data for several reasons. First, refraction statics were applied to the data to remove the effects of this feature. Also, the depression is very shallow and small in scale, whose seismic response is expected to be lost in the near-surface high amplitude ground-roll. Lastly, since the data were acquired using 14 Hz geophones, such near-surface details may not be imaged properly. Although the feature could be interpreted as a graben with normal faults on either side, it is more likely to be an ancient river channel since the data were acquired next to the Jemez River. Since previous river channels and oxbow lakes are visible on the surface via satellite (Fig. 4.28), it is therefore likely that ancient channels exist in the subsurface as well.

Fig. 4.28. Google Earth image of seismic study area. Blue and white lines denote extent of the Jemez Pueblo seismic line and the Indian Springs Fault Zone, respectively. The red circles bound ancient ox-bow lakes and river channels that make up the larger Jemez River channel system.

To estimate the dip of the beds in the subsurface, a simple calculation was carried out. Using the positive amplitude reflector at about 450 ms, its reflection times at CMPs 40 and 95 were recorded at 0.465 ms and 0.455 ms, respectively, and the vertical distance was calculated using an average velocity of 2000 m/s. This resulted in an elevation change of about 10 m after taking into consideration two-way time. Next, the horizontal distance between the two CMP locations was calculated; since each CMP bin is 2.5 m and there are 50 CMPs between the two locations, the resulting distance is 125 m. Finally, the arctangent of (10/125) resulted in an angle of 4.5° above horizontal. Thus, the beds in the near-surface have an apparent dip of about 4.5° to the south in this location.

4.4 The Gravity Method

4.4.1 Acquisition

The gravity survey was acquired in conjunction with, and beside, the Jemez Pueblo seismic survey. The gravity survey consists of 73 unique gravity stations along a single crooked line with a spacing of 20 meters, measured using a tape measure. The total distance of the line is therefore 1440 meters (Fig. 4.29). The survey line, starting near the beginning of the seismic line, was crooked because the stations were located along Day School Road, which itself is crooked. At the end of the survey, the first station was reoccupied and served as the base station to calculate the drift of the gravimeter throughout the duration of the study. A total of two readings were acquired at each station, each consisting of 60 seconds of acquisition. The gravity reading, along with the time and date of acquisition, were saved automatically by the gravimeter. The elevation, latitude, and longitude of each station were acquired with a separate, more accurate GPS unit and were recorded manually in a field notebook. Unfortunately, the notebook was misplaced shortly thereafter and the data have been lost. Therefore, accurate spatial coordinates of the stations are not available. For a complete overview of the gravity data, the reader is referred to Table 3 in Appendix C.

Fig. 4.29. Google Earth image of gravity survey study area. Red and white lines denote extent of the Jemez Pueblo gravity line and the Indian Springs Fault Zone, respectively.

4.4.2 Processing

The gravity data acquired for the Pueblo of Jemez survey were processed in a similar fashion as the data at Meteor Crater—both followed the same processing workflow (Fig. 3.3). Just like the Meteor Crater gravity survey, this data set was also subject to several preprocessing steps. First, the standard deviations of the observations at each station were calculated as a quality measure to make sure that the readings are precise. Next, the observations at each station were averaged and the value was output as the station's final gravity reading. The unprocessed gravity line is shown in Fig. 4.30.

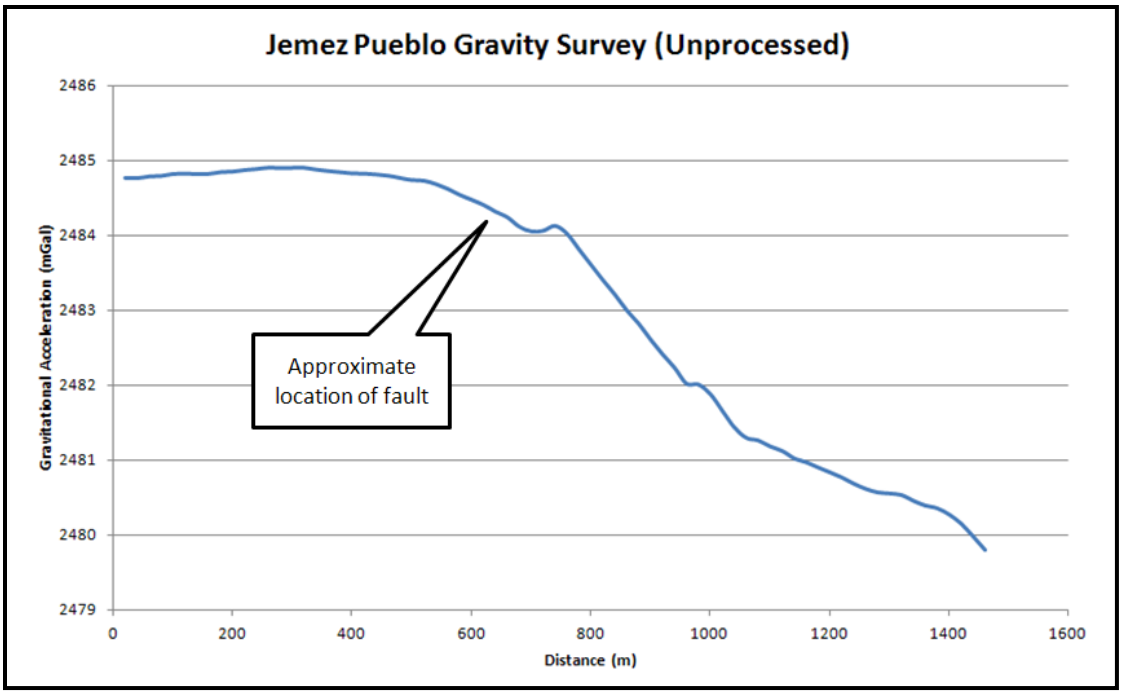

Fig. 4.30. Uprocessed gravitaty vs. distance plot of Jemez Pueblo gravity survey. Approximate location of Indian Springs Fault Zone from Fig. 4.29 is shown (about 630 m).

As with the Meteor Crater gravity study, the tidal correction was automatically accounted for by the gravimeter at the time of acquisition. Thus, the first processing step to be completed manually was the drift correction. As mentioned earlier, the first station along the survey acted as the base station and was occupied at the beginning and end of the survey. With only two base readings, the instrument drift (about 0.4 mGal during the 8 hour survey) was assumed linear throughout the survey and was subtracted appropriately from each station.

The next step in the processing workflow was the latitude correction. As mentioned previously, the latitude, longitude, and elevation of each station were acquired manually, but the data were lost after the survey. Since the latitude correction is an

important step in the processing workflow, latitude values from Google Earth were used instead. Since the first station location was saved by the gravimeter and the survey followed the winding Day School Road, easily visible by satellite, the station locations were interpolated from the beginning of the line in increments of 20 meters. Since the latitude accuracy of a station needs to be within 20 m to maintain an accuracy of 0.01 mGal, the Google Earth spatial corrections were sufficient (Potore, 2008). To correct for the latitude variations, the latitude values at each station were input into the IGF formula (Section 3.1.2) and were subtracted from the gravity measurements.

To properly apply the next step in the workflow, the free air correction, accurate elevations to within 3 cm are needed to maintain an accuracy of 0.01 mGal. Since the spatial data were lost, such accuracy was not able to be attained. However, to put some constraints on the topography along the survey, 7.5-minute USGS topographic maps of the San Ysidro and Jemez Pueblo quadrangles from 2010 and 2011, respectively, were used. With contour intervals of 20 ft (6 m), the elevations were able to be estimated to about ±1 m along the length of the survey via a best-fit 2^{nd} order polynomial (Fig. 4.31). Hence, the data were compensated for long-wavelength signals resulting from large-scale changes in topography. From Fig. 4.31, it is clear that the elevation increases by about 15 m along the length of the survey, which is common in this mountainous area. The resulting free air anomaly is shown in Fig. 4.32, which contains a total change in the gravitational acceleration of about 2.5 mGal, or 2.5 mGal less than prior to the free air correction. Although the data are no longer accurate to within 0.01 mGal, the estimated

0.3 mGal accuracy attained from the quadrangle maps is much better than no elevation constraint at all.

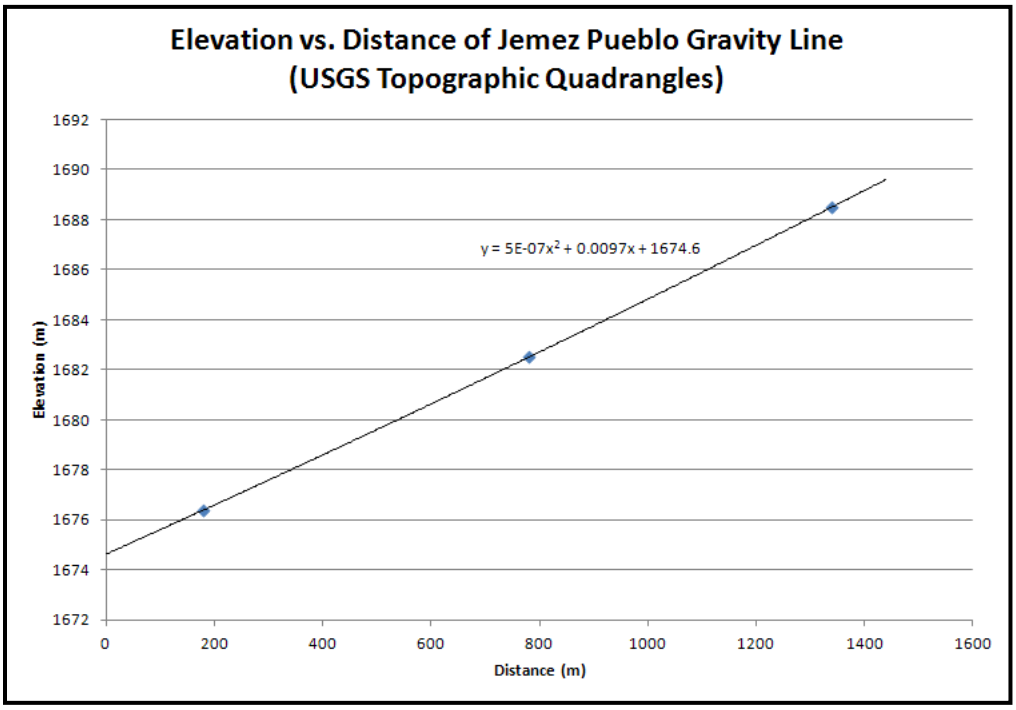

Fig. 4.31. Graph of elevation vs. distance of Jemez Pueblo gravity survey. 3 points were obtained from USGS topographic quadrangles of the area and a best-fit 2nd order polynomial trendline was approximated to interpolate elevations between the points along the survey.

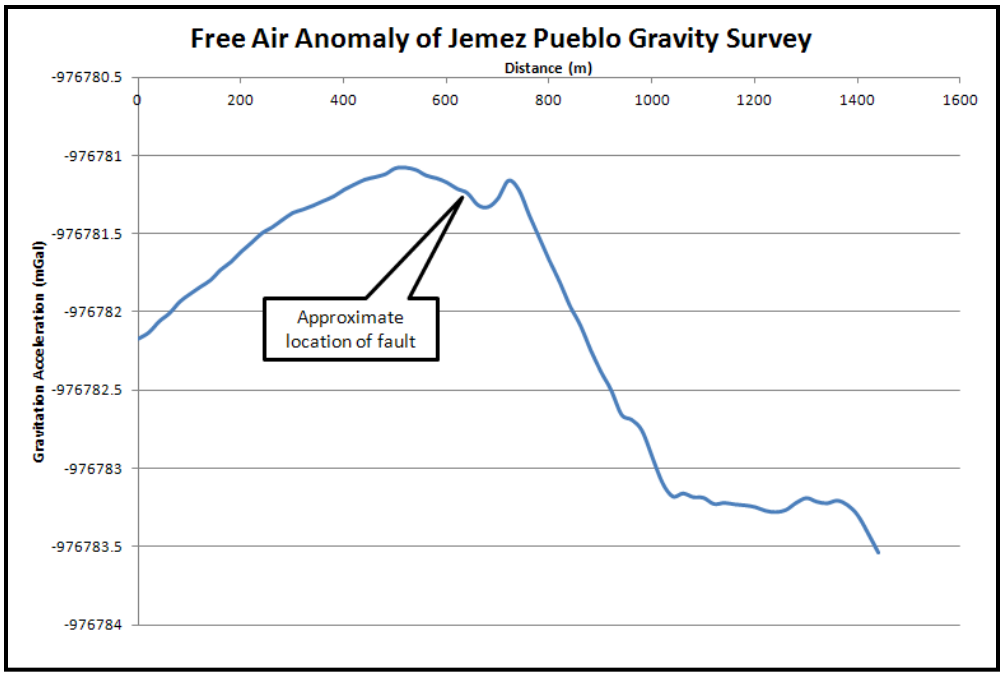

Fig. 4.32. Distance vs. gravity plot of the free air anomaly of the Jemez Pueblo gravity survey. Approximate location of Indian Springs Fault Zone from Fig. 4.29 is shown (about 630 m).

Following the processing workflow shown in Fig. 3.3, a Bouguer correction was applied next. The method consists of using an infinite planar slab of constant density representative of material between the highest and lowest elevations in the survey area. Since a modest change in elevation of 15 m exists along the survey, the density value must be representative of the topmost 15 m of rock and sediment. Although well logs from previously drilled wells in the area were obtained, none represent lithologies of the Santa Fe Group, which includes the topmost Zia Formation among others. Thus, an estimated density of 2.0 g/cc was chosen for the infinite slab. Such a low density was used for several reasons: the Zia Formation is an eolian and fluvial quartz sandstone, it is lightly cemented and porous, is easily eroded, and is of Miocene age (Galusha, 1966). For these reasons, a low density is expected. The Bouguer correction was then calculated and

subtracted from the free air anomaly, resulting in the simple Bouguer anomaly (Fig. 4.33).

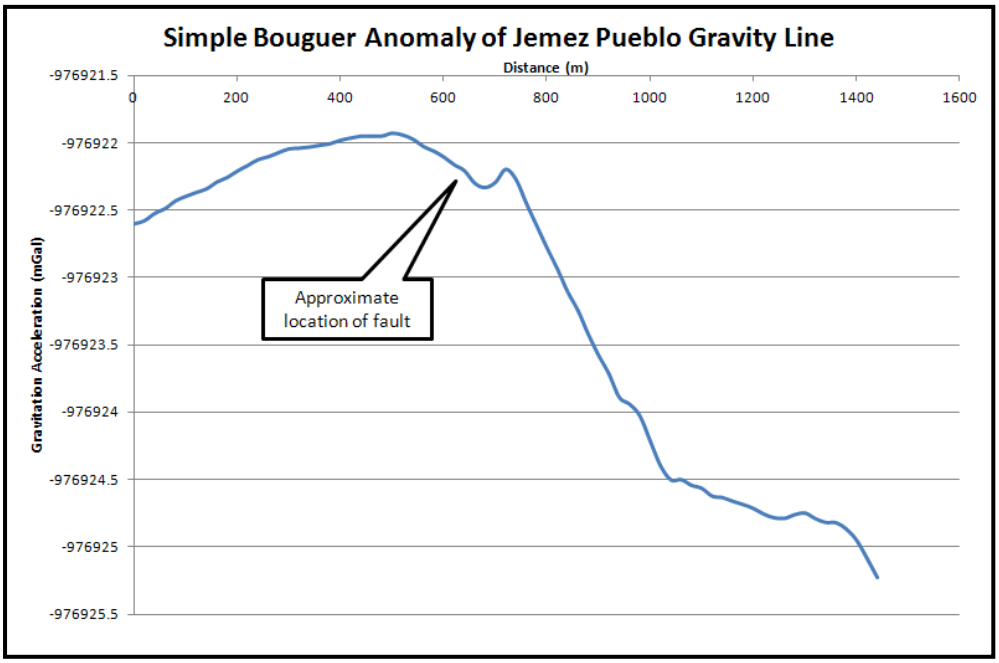

Fig. 4.33. Distance vs. gravity plot of simple Bouguer anomaly of Jemez Pueblo gravity survey. Approximate location of Indian Springs Fault Zone from Fig. 4.29 is shown (about 630 m).

After the simple Bouguer anomaly was obtained, data processing was completed. A terrain correction was not applied to the Jemez Pueblo gravity survey for the following reasons: accurate elevations along the survey were not known, the topography was not very severe, only small corrections would result from such a laborious step, the data contain a precision of no more than 0.3 mGal, and the survey served as a study of the overall structure of the subsurface as opposed to a high resolution microgravity survey. Thus, with some knowledge of the subsurface geologic structure from this study's seismic line and other geophysical studies, an interpretation of the data was undertaken in the following section.

4.4.3 Interpretation

Although the initial phase of gravity interpretation usually involves anomaly separation to isolate the residual signal from the regional one, the step was omitted in this study because most of the composite signal seems to belong to the major fault in the area, which is the signal of interest. A more extensive study would be necessary to remove very long-wavelength signals resulting from very deep sources. Also, small-wavelength signals from shallow sources do not seem to have a large effect on the smooth composite signal and were therefore left alone. Thus, the next step involved creating a forward model of the gravity data based upon a priori geologic and geophysical knowledge of the area.

Several sources were consulted in creating the simple subsurface model. Structural and stratigraphic information were obtained from a recent seismic study by Huang et al. (2011) and served as the centerpiece for the model. Densities for the various lithologies were obtained from a compensated bulk density log from a nearby well. In fact, the offset well, a wildcat oil-test well drilled by Shell Oil in 1972 about 27 km from the seismic line, was extensively studied and documented (Black and Hiss, 1974). Integrating all of these pieces of information, the model shown in Fig. 4.34 was created.

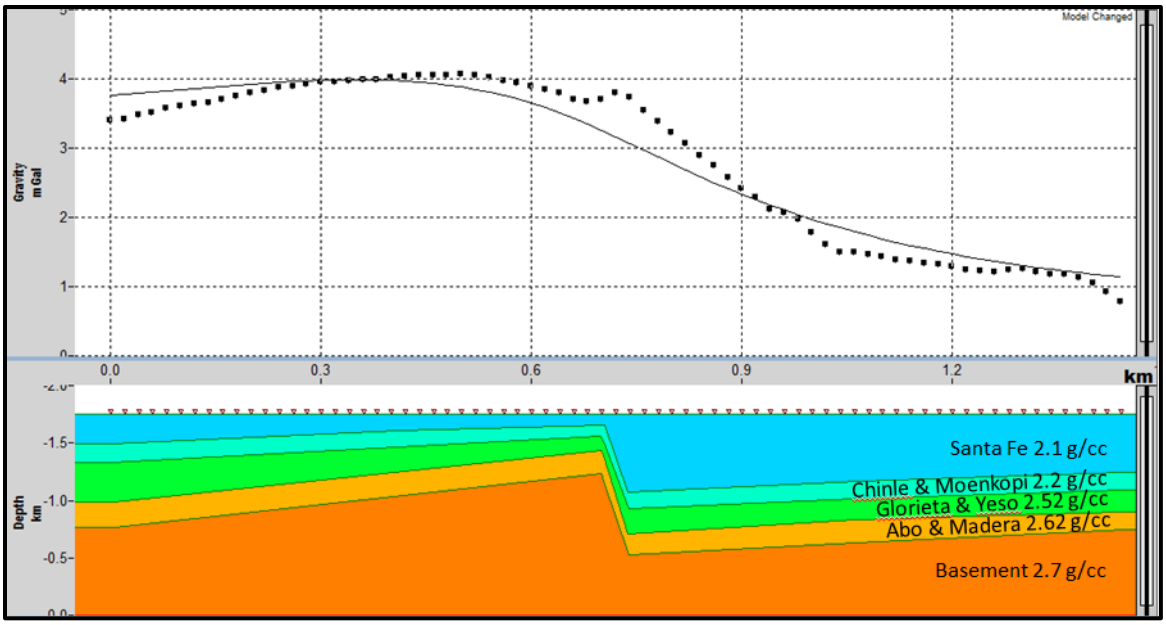

Fig. 4.34. A simplified subsurface model along the gravity survey at Jemez Pueblo, NM (bottom). Several formations, the same as those shown in Fig. 4.3, with similar densities were grouped together for simplicity. The Indian Springs Fault Zone is shown in the middle. Solid black line (top) represents gravity field resulting from the model. Dotted black line (top) represents actual field measurements from the gravity survey. The gravity misfit between the acquired data and model is 0.254 mGal.

Fig. 4.34 consists of two parts: the model, shown at the bottom, and the gravity readings, shown at the top. The model consists of 5 layers representing the 8 formations shown in Fig. 4.3—formations with similar densities were merged to simplify the model. Since the gravity survey was much longer than the seismic survey and traversed over the Indian Springs fault zone, the model was modified from Fig. 4.3 to reflect those changes.

With a misfit of 0.254 mGal, the gravity field resulting from the model (black line) is in good agreement with the actual gravity survey (dotted black line). This type of misfit was expected since the data were processed to within 0.3 mGal, as was mentioned in section 4.4.2. Both lines show an initial increase in the gravity field (resulting from the

southerly dipping beds), then exhibit a large decrease (associated with the large normal fault zone), and then a sub-horizontal response towards the end, which is most likely the combined response of the dipping beds and distant fault. The greatest discrepancy between the model and the actual data exists closest to the fault location, where the acquired data show a large decrease over a much shorter distance than the model. This difference is most likely the result of a more complex fault system than is represented by the single fault within the model. Nonetheless, the model accurately portrays a simplified structure of the subsurface.

4.5 Joint Interpretation

Integrating the seismic and gravity data, a joint interpretation over the area of the seismic study was conducted to determine if both methods are in agreement with the simple model created in the previous section. As mentioned previously, the seismic data show reflectors dipping at about 4.5° to the south. Hence, the formations to the left (south) of the fault within the simple model also have beds dipping at about 4.5°. A closer inspection of the model gravity results and stacked seismic section are shown in Fig. 4.35. Clearly, there is a general increase in the gravity field from left to right (south to north) in both the actual and model data, likely due to the dipping beds shown in the seismic section. The disparities between the model results and actual gravity data are small in both amplitude and frequency, likely to be caused by small-scale features. Since the results from the seismic method do not show changes in acoustic impedance

consistent with these features, it is likely that they are below the resolution of the seismic method or are caused by out-of-plane structures.

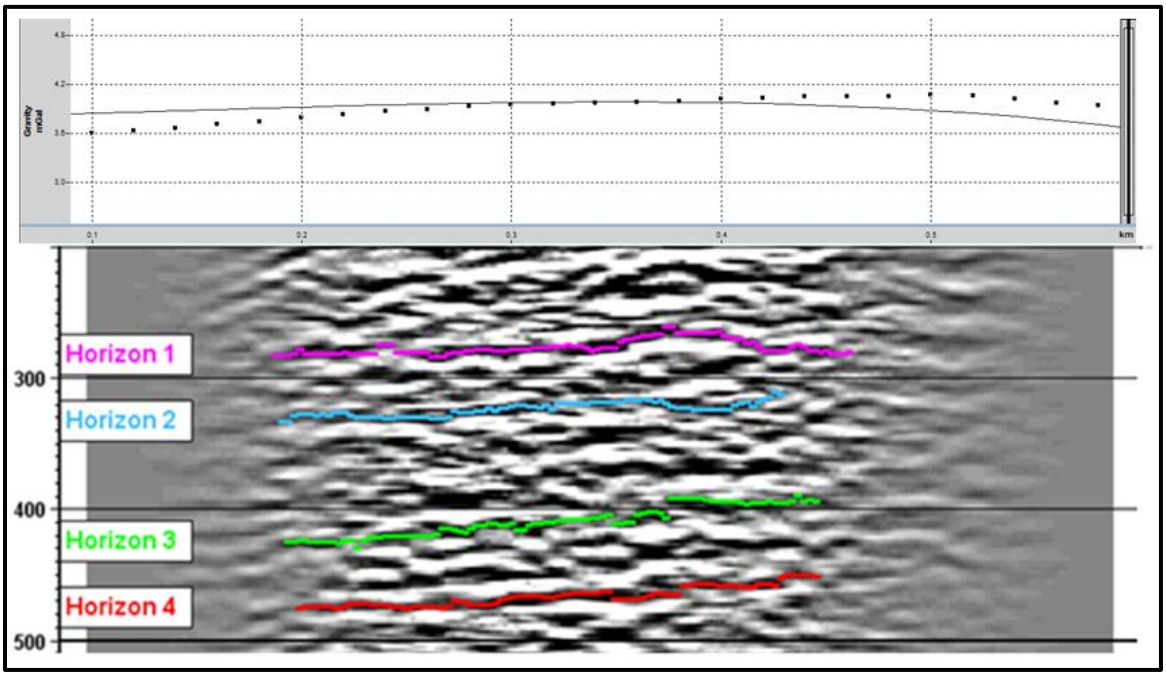

Fig. 4.35. Gravity results (top) and stacked seismic section (bottom). The solid black and dotted lines on the gravity data represent the model and actual results, respectively. The seismic section shows 4 interpreted horizons up to a time of 500 ms. The dipping reflections are likely the cause of the increase in the gravity field from left to right.

4.6 Discussion/Conclusions

The results of the near-surface geophysical study at the Pueblo of Jemez, NM, have reaffirmed what has previously been suspected from geologic work in the area: southerly dipping beds cross-cut by a major fault zone extending to the basement rock. Numerous southerly-dipping reflections (4-5°) have been imaged to the south of the fault zone up to 600 ms in time (or roughly 600 m in depth) via a 475 m 2-D seismic line. A

model resembling the subsurface of the seismic line was created to simulate the reflection seismic study. The model results show numerous reflections at the near-surface, extending to a time of 500 ms, in close agreement with the actual seismic study.

The 1.44 km gravity survey indicates a decrease in the gravitational field across the Indian Springs Fault Zone, in agreement with previous geophysical studies of the area (Huang and Albrecht, 2011; Huang et al., 2011). In addition, the gravity survey also indicates southerly-dipping reflectors along the length of the seismic survey. A forward model of the subsurface along the gravity survey was created to test these hypotheses; initial results confirm such a geologic model as plausible.

Although the seismic and gravity results are encouraging, more work needs to be done to properly image the near-surface. Like the Meteor Crater study, future geophysical work regarding the Pueblo of Jemez geothermal project should include a high-resolution 3-D seismic reflection study. Such a study should consist of a more powerful source (such as a vibe), small shot-receiver spacing, high CMP fold, and a wide range of azimuths. In addition, 3-D gravity, magnetic, and other potential field surveys could be acquired in conjunction with a seismic survey for little cost. Only then will the near-surface structure be properly understood.

Conclusions

The Meteor Crater and Pueblo of Jemez geophysical projects have shown that near-surface imaging utilizing simple acquisition tools and techniques can be effective in helping our understanding of complex structures beneath our feet. The first reflection seismic survey at Meteor Crater helped create a general picture of the subsurface structure through the identification of numerous reflectors and several possible faults. The refraction seismic technique, on the other hand, helped characterize the rock properties of the very near-surface (upper 50 m) and constrain the thickness of low velocity layer—a large increase in near-surface velocity occurs at 250 m, indicating a possible fault or rapid decrease in brecciation. The refraction analysis also indicates an increase in velocity with increasing distance from the crater rim, as was expected.

Gravity and magnetic data were acquired and analyzed to complement the seismic study. The residual gravity anomaly and resulting forward model also support a fault at 250 m along the seismic survey. In addition, the gravity anomalies of the 3 radial lines at Meteor Crater are indicative of an extensive concentric geologic structure since the character of the gravity field of all three lines is similar. A forward model of expected subsurface densities based on the refraction seismic analysis using known density-velocity relationships was also created—the results seem to be inconsistent with the acquired data.

The residual magnetic anomaly of Line 1 at Meteor Crater contains a large magnetic error with respect to the forward model used in the gravity study. This

discrepancy is in large part due to poor subsurface constraints and low lateral resolution. To create a magnetic subsurface model of Meteor Crater, magnetic properties of the formations need to be well understood, subsurface structures need to be of higher resolution, and the effects of iron-rich meteoritic materials on the magnetic field need to be recognized. Also, the three radial lines at Meteor Crater are not of similar character and therefore do not seem to support the existence of a concentric structure. However, the aforementioned lack of subsurface constraints and unknown subsurface structure could be the cause instead. A source-to-depth analysis of the residual magnetic anomaly indicated the average depth of the magnetic perturbations to be at 25 m, in agreement with the top of the iron-rich Moenkopi formation. The depth study also indicated anomalous results near the hypothesized fault, indicative of a large structural feature.

Because the limitations of the techniques and tools used in this study have been recognized, recommendations for future surveys at Meteor Crater were also proposed. Future seismic surveys should include 3-D seismic acquisition and processing technology for enhanced subsurface imaging. Depending on the depth of investigation, sources such as a vibe truck or shotguns should also be considered. Also, if the depth of investigation is shallow, higher frequency geophones and smaller receiver sampling should increase data quality. Like the seismic recommendations, future potential field studies should also include 3-D surveys and possibly shorter station spacing if the shallow near-surface is being investigated.

The geophysical work at the Pueblo of Jemez included a single 2-D seismic test line and a gravity survey. The 475 m seismic survey, acquired just south of the Indian Springs Fault Zone, shows numerous beds dipping to the south at an angle of about 4.5°.

A time-to-depth conversion of the final stacked image supports the top of the Precambrian bedrock to be at a depth of 700 m, or about 500 ms. The refraction statics study also indicates ancient river channels in the very near-surface as part of the larger channel complex.

The 1.44 km gravity survey, acquired over the Indian Springs Fault Zone, shows a distinct decrease in the gravity field, corresponding to the fault. Gravity results from a simple forward model representing the faulted subsurface are in good agreement with the acquired data. Discrepancies between the actual and model data are the results of a simplified 2-D model of a complex 3-D subsurface. The gravity data are also in agreement with the seismic data where the two overlap—dipping beds correspond to a slight increase in the gravity field.

Like the Meteor Crater study, to gain a fuller picture of the subsurface, future work at the Pueblo of Jemez should also include 3-D seismic reflection and potential field data. Because the depth of investigation is deep, a vibe source would likely significantly increase the quality of the final image.

As geophysical acquisition tools and techniques progress, so will our understanding of the near-surface. For example, Appendix B highlights the improvement in data quality and depth of penetration when a more powerful source such as a vibe is used instead of the AWD system. Utilizing such improved technologies in our future work at geologically complex areas such as Meteor Crater and the Pueblo of Jemez will undoubtedly lead to better scientific results and more informed economic decisions.

References

Ackermann, H.D., Godson, R.H., and Watkins, J.S., 1975, A seismic refraction technique used for subsurface investigations at Meteor Crater, Arizona: Journal of Geophysical Research, **80**, 765-775.

Baag, C., and Helsley, C. E., 1974, Evidence of penecontemporaneous magnetization of the Moenkopi formation: Journal of Geophysical Research, **79**, 3308-3320.

Baker, G. S., Steeples W. D., and Drake M., 1998, Muting the noise cone in the near-surface reflection data: an example from southeastern Kansas: Geophysics, **63**, 1332-1338.

Baker, G. S., 1999, Processing Near-surface Seismic-Reflection Data: a Primer: Society of Exploration Geophysicists.

Black, B. A., and Hiss, W. L., 1974, Structure and stratigraphy in the vicinity of the Shell Oil Co. Santa Fe Pacific no. 1 test well, southern Sandoval County, New Mexico: New Mexico Geol. Soc. Guidebook, 25th Field Conf., Ghost Ranch (Central-Northern N.M.), 365-370.

Blakely, R. J., 1996, Potential Theory in Gravity and Magnetic Applications: Cambridge University Press.

Buker, F., Green, and A. G., Horstmeyer, H., 1998, Shallow seismic reflection study of a glaciated valley: Geophysics, **63**, 1395-1407.

Chao, E. C. T., Shoemaker, E. M., and Madsen, B.M., 1960, First natural occurrence of coesite: Science, **132**, 220-222.

Chao, E. C. T., Fahey, J. J., Littler, J., and Milton, D. J., 1962, Stishovite, SiO2, a very high pressure new mineral from Meteor Crater, Arizona: Journal of Geophysical Research, **67**, 419-421.

Cox, M., 1999, Static Corrections for Seismic Reflection Surveys, Society of Exploration Geophysicists.

Diogo, L. A., Diagon, F., and Prado, R. L., 2004, Bedrock imaging using post-critical shallow seismic reflection data: Journal of Applied Geophysics, **57**, 1-9.

Doornenball, J. C., and Helbig, K., 1983, High resolution reflection seismic on a tidal flat in the Dutch Delta—acquisition, processing, and interpretation: First Break, **1**, No. 5, 9-20.

Foote, A. E., 1891, A new locality for meteoritic iron with a preliminary notice of discovery of diamonds in the iron: Proc. American Association of Advanced Science, **40**, 279-283.

Galusha, T., 1966, The Zia sand formation, new early to medial Miocene beds in New Mexico: American Museum Novitates, 2271, 12 p.

Gardner, G. H. F., Gardner, L. W., Gregory, A. R., 1974, Formation velocity and density—the diagnostic basics for stratigraphic traps: Geophysics, **39**, 770-780.

Harding, N., 1954, A Gravity investigation of Meteor Crater Arizona: Master of geology-geophysics science thesis, University of Wisconsin, 44 p.

Heiken, G. and Goff, F., 1983, Hot dry rock geothermal energy in the Jemez Volcanic Field, New Mexico: Journal of Volcanology and Geothermal Research, **15**, 223-246.

Huang, L., and Albrecht, M., 2011, Seismic and magneto-telluric imaging for geothermal exploration at Jemez Pueblo in New Mexico: Proceedings, 36th Workshop on Geothermal Reservoir Engineering Stanford University, Stanford, California, January 31 - February 2, 2011 SGP-TR-191

Huang, L., Albrecht, M., Kaufman, G., Kelley, S., Rehfeldt, K., Zhang, Z., 2011, Imaging faults with reverse-rime migration for geothermal exploration at Jemez Pueblo in New Mexico: GRC's 35th annual meeting, 2011-10-23/2011-10-26 (San Diego, California, United States), LA-UR-11-10640

Hunter, J. A., Pullan, S. E., Burns, R. A., Gagne, R. M., and Good, R. L., 1984, Shallow seismic reflection mapping of the overburden-bedrock interface with the engineering seismograph—some simple techniques: Geophysics, **49**, 1381-1385.

Kaiser, A. E., Green, A.G., Campbell, F.M., Horstmeyer, H., Manukyan, E., Langridge, R. M., McClymont, A. F., Mancktelow, N., Finnemore, and M., Nobes, D. C., 2009, Ultrahigh-resolution seismic reflection imaging of the Alpine Fault, New Zealand: Journal of Geophysical Research, **114**, 2156-2202.

Kallweit, R. S., and Wood, L. C., 1982, The limits of resolution of zero-phase wavelets, Geophysics, **47**, 1035-1046.

Kane, M. F., 1962, A comprehensive system of terrain corrections using a digital computer, Geophysics, **27**, 445-462.

Kring, D.A., 2007, Guidebook to the Geology of Barringer Meteorite Crater, Arizona (a.k.a. Meteor Crater): LPI Contrib., 150 pp., Lunar and Planetary Institute, Houston, TX.

Kumar, P. S., and Kring, D. A., 2008, Impact fracturing and structural modification of sedimentary rocks at Meteor Crater, Arizona: Journal of Geophysical Research, **113**, 1-17.

Miller, R. D., and Xia, J., 1998, Large near-surface velocity gradients on shallow seismic reflection data: Geophysics, **63**, 1348-1356.

Pilkington, M. and Grieve, R.A.F., 1992, The geophysical signature of terrestrial impact craters: Reviews of Geophysics, **30**, 161-181.

Pilon, J.A., Grieve, R.A.F, and Sharpton, V.L., 1991, The subsurface character of Meteor Crater, Arizona, as determined by ground-probing radar. Journal of Geophysical Research, **96**, 15563-15576.

Poelchau, M.H. and Kenkmann, T., 2008, Asymmetric signatures in simple craters as an indicator for an oblique impact direction: Meteoritic and Planetary Science, **43**, 2059-2072.

Poelchau, M.H., Kenkmann, T., and Kring, D.A., 2009, Rim uplift and crater shape in Meteor Crater: effects of target heterogeneities and trajectory obliquity: Journal of Geophysical Research, **114**, E01006, doi:10.1029/2008JE003235.

Potore, D., 2008, Horizontal positional accuracy of Google Earth's high-resolution imagery archive: Sensors, **8**, 7973-7981.

Purucker, M. E., Elston, D. P., and Shoemaker, E. M., 1980, Early acquisition of characteristic magnetization in red beds of the Moenkopi formation (Triassic), Gray Mountain, Arizona: Journal of Geophysical Research, **85**, 997-1012.

Regan, R.D. and Hinze, W.J., 1975, Gravity and magnetic investigations of Meteor crater, Arizona. Journal of Geophysical Research, **80**, 776-788.

Roddy, D.J., Boyce, J.M., Colton, G.W., and Dial, A.L. Jr., 1975, Meteor Crater, Arizona, rim drilling and thickness, structural uplift, diameter, depth, volume, and mass-balance calculations: Proc. Lunar and Planetary Science Conf 6th, 2275-2308.

Roddy, D.J., 1978, Pre-impact geologic conditions, physical properties, energy calculations, meteorite, and initial crater dimensions and orientations of joints, faults, and walls at Meteor Crater, Arizona: Proc. Lunar and Planetary Science Conference 9th, 3891-3930.

Roy, S., Stewart, R., and Dulaijan, K.A., 2010, S-wave velocity and statics from ground-roll inversion: The Leading Edge, **29**, 1250-1257.

Salvador, A. (ed.), 1991, Decade of North American Geology, Gulf of Mexico Basin: The Geological Society of America.

Shoemaker, E. M., 1960, Penetration mechanics of high velocity meteorites, illustrated by Meteor Crater, Arizona: International Geological Congress, 21st, Copenhagen, 418-434.

Shoemaker, E. M., 1963, Impact Mechanics at Meteor Crater, Arizona, in B. M. Middlehurst and G. P. Kiuper, The Moon, Meteorites, and Comets, v. IV, 301-336.

Shoemaker, E. M., 1987, Meteor Crater, Arizona: Geological Society of America Centennial Field Guide—Rocky Mountain Section, 399-404.

Shtivelman, V., Frieslander, U., Zilberman, E., and Amit, R., 1998, Mapping shallow faults at the Evrona playa site using high-resolution reflection method: Geophysics, **63**, 1257-1264.

Steeples, D. W. and Miller, R. D., 1998, Avoiding pitfalls in shallow seismic reflection surveys: Geophysics, **63**, 1213-1224.

Yilmaz, O., 2001, Seismic Data Analysis: Processing, Inversion, and Interpretation of Seismic Data: Society of Exploration Geophysicists.

Appendix A—LaMarque, TX

Abstract

A seismic survey was conducted at the University of Houston Coastal Center (UHCC) in LaMarque, TX, to determine the imaging capabilities of the seismic equipment and to gain an in-depth understanding of the near-surface. A single component 360 m 2-D seismic line was acquired over several days to achieve these goals. After the data were processed via a conventional workflow, the data were then interpreted. The results indicate numerous flat-lying reflectors along the length of the line, absent of complex geologic structures. This type of geology was expected since the survey area resides along the coastal plains of Texas. However, the clarity of the reflectors and the depth of penetration were unexpected: reflectors are imaged up to nearly 1 km in depth in the final migrated section. These results are very encouraging and will no doubt be a stepping stone for further geophysical research.

Introduction

A seismic survey was conducted at the University of Houston Coastal Center (UHCC) in LaMarque, TX on March 20th and 21st, 2010. The purpose of this study was to test the capabilities of the recently purchased seismic acquisition equipment and to gain an understanding of the subsurface geology at the UHCC, where numerous oil and gas wells are in operation. Although the coastal subsurface geology is expected to be "layer-

cake" like, this study served as a learning experience for future high resolution near-surface seismic reflection studies in more structurally complex areas such Meteor Crater, Arizona, and Jemez Pueblo, New Mexico.

Area of Study

As previously mentioned, the seismic survey was conducted at the UHCC, which is located near Interstate 45 in LaMarque, Galveston County, Texas (Fig. A.1). Although the UHCC mainly serves as an area for environmental research of the Texas coast, such as prairie and wetland ecology, it was also found to be an ideal site for near-surface geophysical research because of its seclusion, large expanse, access to UH personnel, and producing oil and gas wells.

Fig. A.1. Google Earth image of UHCC outlined in red. Major roads shown. Galveston Island is located in bottom right corner.

Geologic Background

The geology of coastal Texas is characterized by fairly flat-lying sediments, prograding towards the Gulf of Mexico Basin (Fig. A.2). These terrigenous sediments, deposited by rivers on the continental shelf, are of Quaternary to Triassic in age. Since this seismic study is concerned with the near-surface, only the Quaternary and Neogene sediments of the Plio-Pleistocene are likely to be imaged.

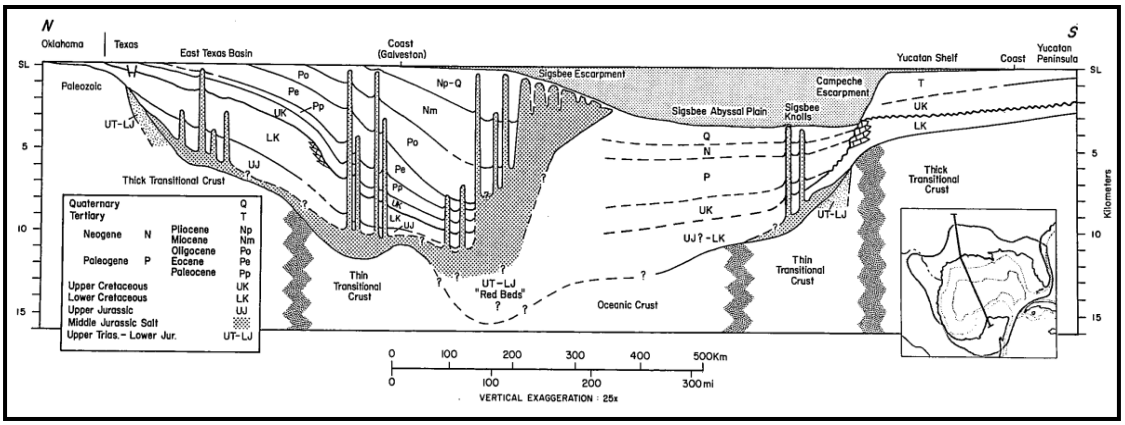

Fig. A.2. Generalized north-south cross-section of Gulf of Mexico Basin (Salvador, 1991).

Acquisition

Although several seismic surveys were acquired during the UHCC near-surface study, this work focuses on the longest of these surveys: a 360 m vertical-component 2-D seismic line in the northwest corner of the UHCC (Fig. A.3). The survey was composed of 120 14-Hz geophones in a straight line with a spacing of 3 m. The shots, or accelerated weight drops, were located in between each pair of consecutive receivers and had a spacing of 3 m, resulting in a total of 121 shots. The geometry of the line is shown in Fig. A.4.

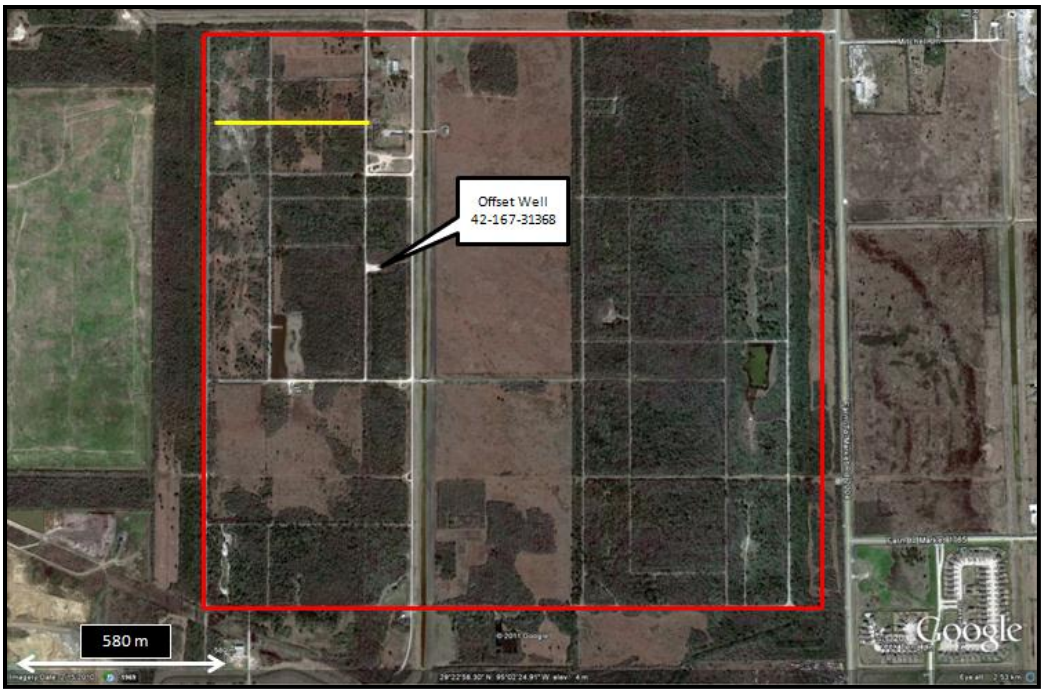

Fig. A.3. Google Earth image of area of study. Red box outlines extent of UHCC and yellow line represents extent of seismic reflection study. Callout points to offset well used in seismic to well log correlation.

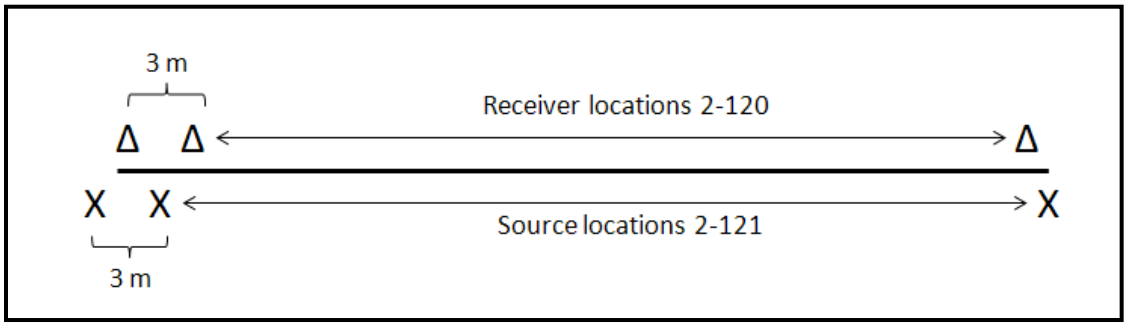

Fig. A.4. Geometry of the Lamarque seismic survey. Both source and receiver spacings remained constant at 3 m. The survey consists of 120 receivers and 121 shots.

Processing

A processing workflow similar to the Meteor Crater and Jemez Pueblo workflows was established to process the acquired seismic data and to compare and contrast the various data sets (Fig. A.5). The key difference is a pre-stack time migration in addition to a post-stack time migration. A pre-stack migration was chosen in this case because the simple layer-cake geology of the area and prominent reflectors allowed the pre-stack migration to be effective.

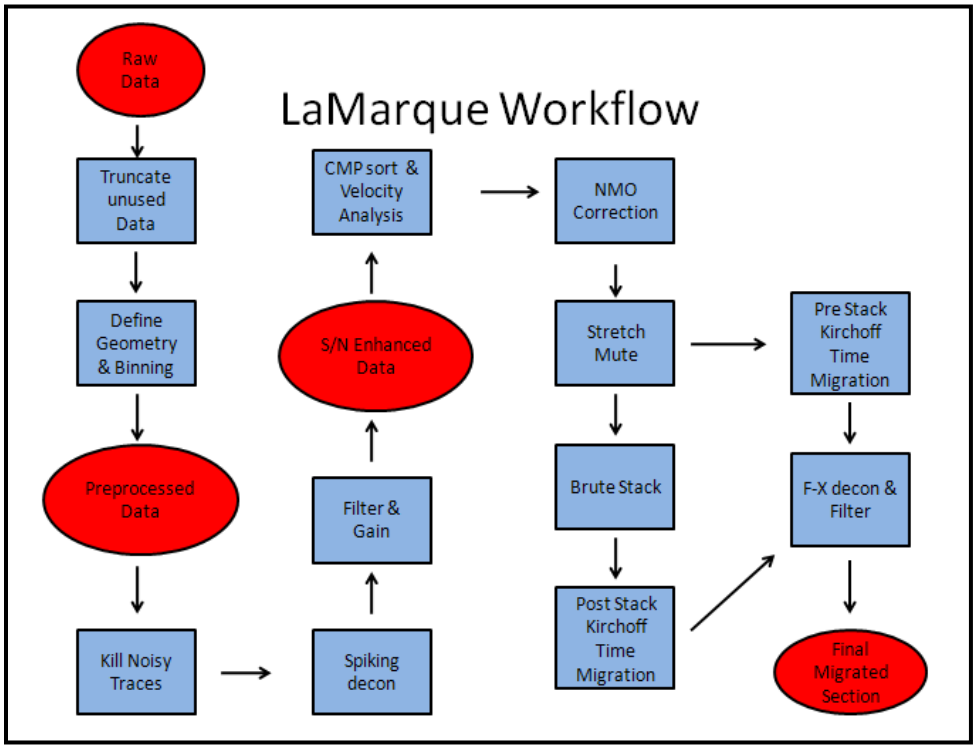

Fig. A.5. LaMarque seismic data processing workflow.

First, the data were truncated to 1000 ms since no visible reflectors were seen beyond that time. Next, the source and receiver geometries of the survey were defined according to the acquisition parameters mentioned in the previous section (Fig. A.6).

CMP bins were then created along the line to sort the data by CMP in later processing steps, resulting in CMP bins of 1.5 meters. The CMP fold of the line was then calculated based on the acquisition parameters (Fig. A.7).

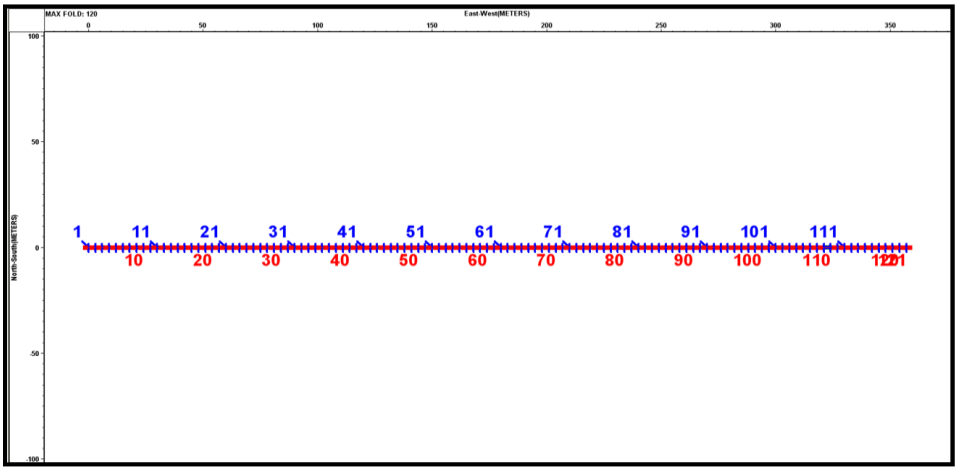

Fig. A.6. Source and receiver geometry of seismic line at LaMarque, TX. Red squares and blue crosses represent shot and receiver locations, resepectively. X-axis is distance along seismic line (0-360 m) and y-axis is distance perpendicular to seismic line (-100-100 m).

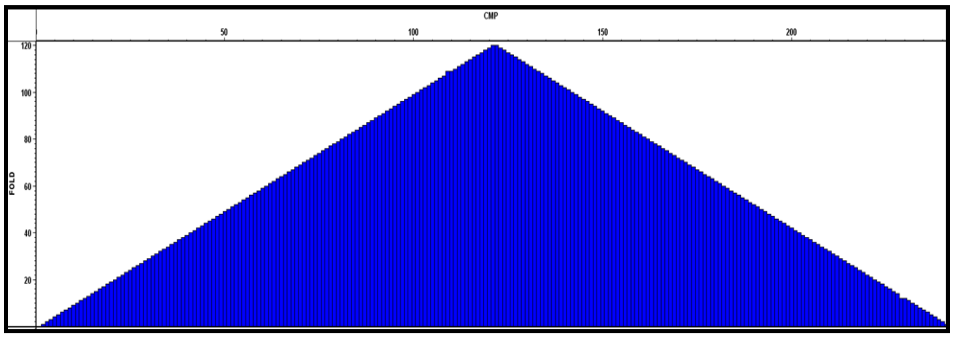

Fig. A.7. Sub-surface CMP fold of LaMarque seismic line. Maximum fold is 120. X-axis is CMP number (0-240) and y-axis is fold (0-120).

The raw shot gathers were then examined to inspect the quality of the data (Fig. A.8). The inspection was promising: clear reflections below the refractions were easily visible and the reflections extended to nearly 1000 ms, very deep for such a small source

and short line. Next, noisy traces resulting from bad geophones and surface noise were killed to increase the S/N of the data. A refraction analysis was then conducted to get an idea of the very near-surface geology and velocity structure and to estimate the refraction statics necessary to compensate for near-surface heterogeneities. Elevation statics were not applied because the elevation throughout the length of the line did not vary by more than 1 m.

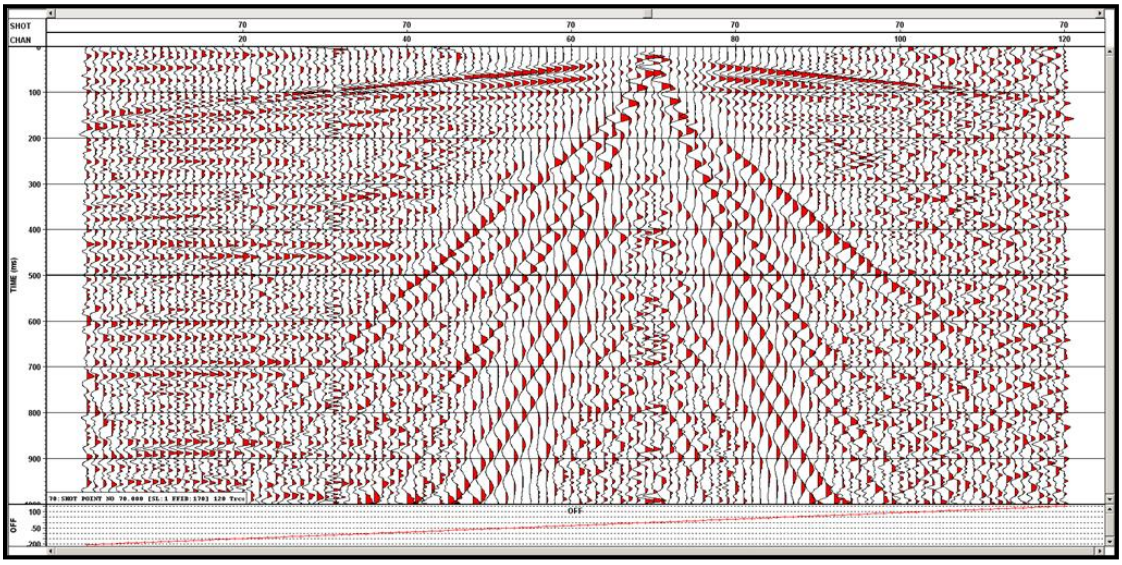

Fig. A.8. Raw shot gather 70 of LaMarque seismic data. Reflections are clearly visible on left side of shot location. Channels 1-120 along x-axis and 0-1000 ms along y-axis.

A 100 ms operator length predictive lag decon with a 10 ms lag was then applied to the data to increase temporal resolution and eliminate multiples. LMO, f-k, and band-pass filters were also applied to reduce ground roll and other low-frequency noise. The LMO filters ranged from 0 to 1000 m/s and up to 20 Hz in frequency; the f-k filter eliminated coherent signals up to about 500 m/s; the band-pass filter consisted of a 25 Hz

low-cut filter. These steps dramatically improved image quality, evidenced by Fig. A.9, which shows the effect of the f-k filter.

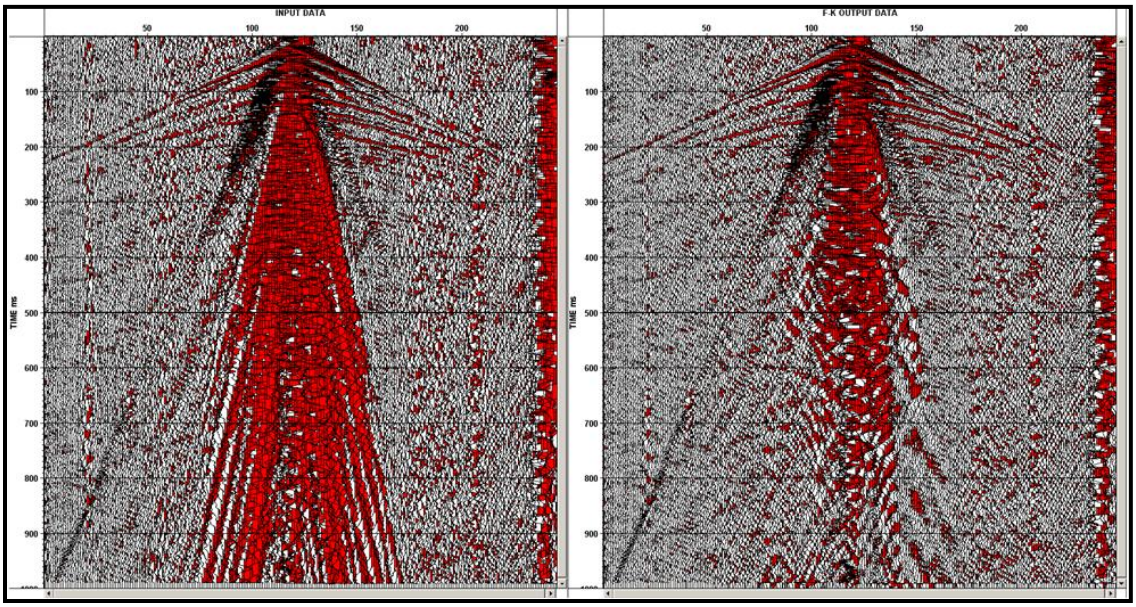

Fig. A.9. Shot gather 60 before (left) and after (right) applying an f-k filter. Much of the linear ground roll has been removed and reflections are easier to discrminiate after the f-k filter.

Next, a velocity analysis was undertaken through the use of semblance plots, CMP gathers, and constant velocity stacks (Fig. A.10). Velocities were picked every 10 CMPs and the resulting velocity structure that emerged is shown in Fig. A.11. Using this velocity structure, an NMO correction was then applied and a 30% stretch was used. At this point, the workflow diverged in two directions: a brute stack of the NMO-corrected CMP gathers was created as was a pre-stack time migration. Following the brute stack, a post-stack time-migration was then applied. This was done in an effort to compare and contrast the effect of time migration before and after stacking.

Finally, after migration, an 80 ms f-x decon operator and a 30-150 Hz band-pass filter were applied to increase the coherency of the final sections. Fig. A.12 shows a pre-stack and post-stack Kirchoff time migration along with a brute stack. From the figure, it seems that a pre-stack migration resulted in the sharpest final image. An interpretation of the data is completed in the following section.

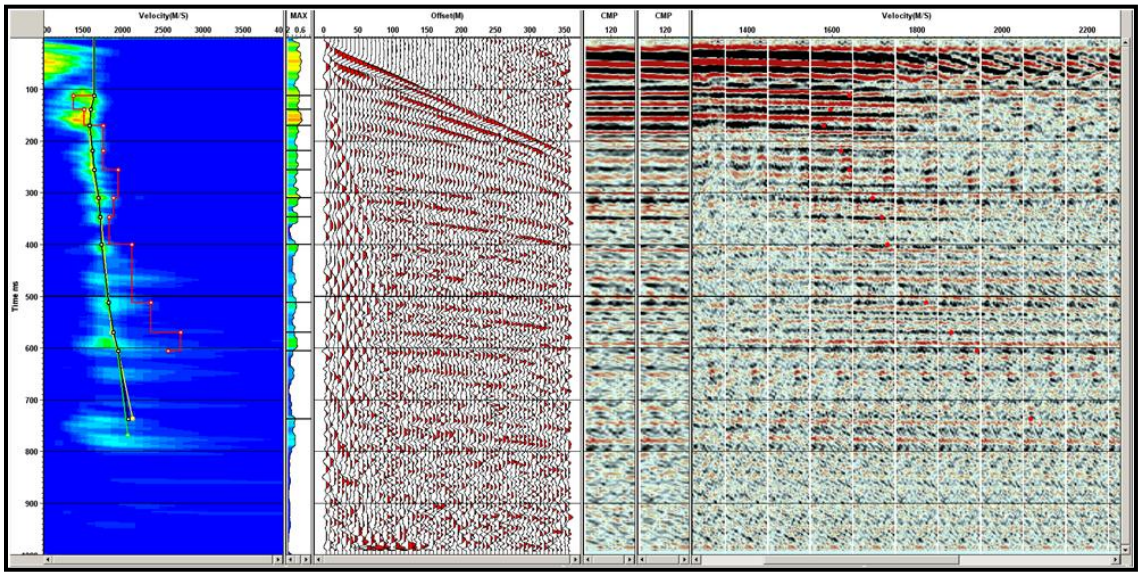

Fig. A.10. RMS velocity analysis using a semblance plot (left), a CMP gather (middle), and constant velocity stacks (right).

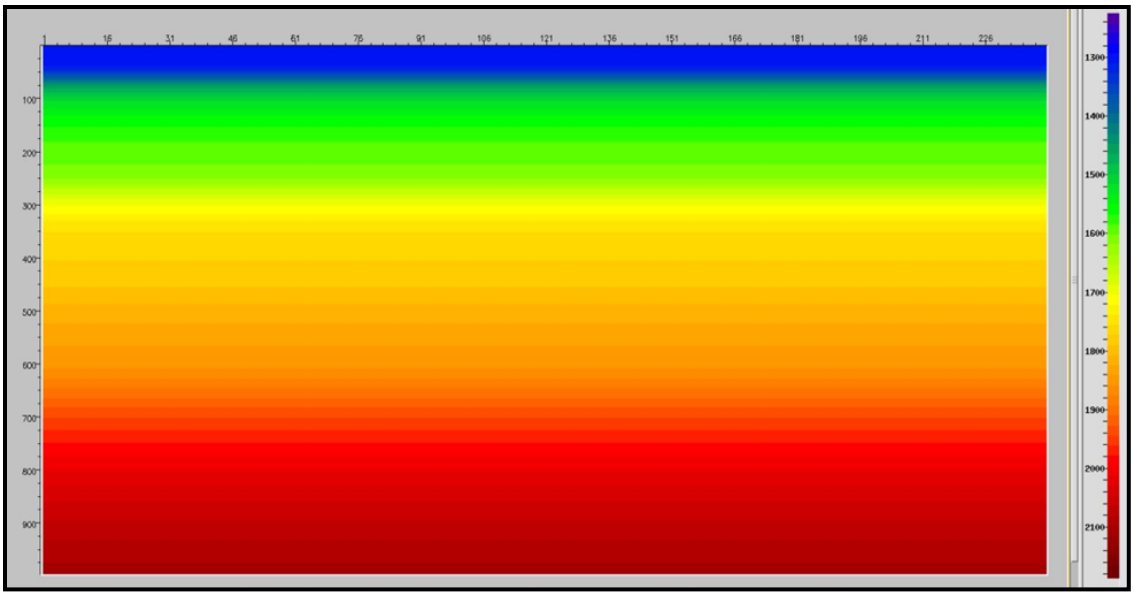

Fig. A.11. RMS velocity profile from velocity analysis. X-axis represents CMP (1-240) and y-axis time (0-1000 ms). Velocity scale at right ranges from 1,200 m/s (blue) to 2,200 m/s (red).

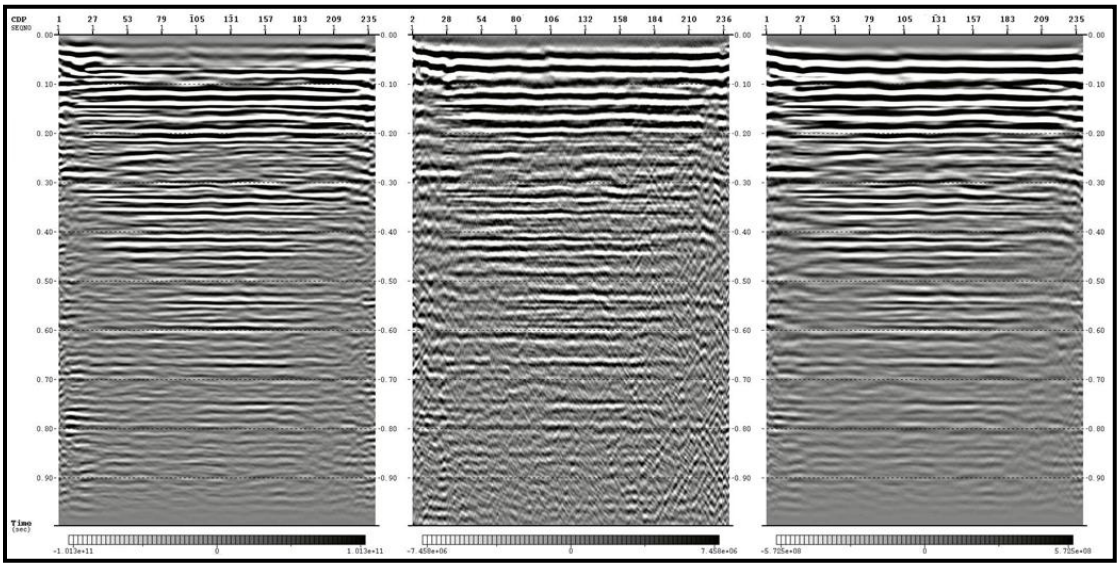

Fig. A.12. A pre-stack Kirchoff time-migration (left), a brute stack (middle), and post-stack Kirchoff time migration (right) are shown. X-axis represents CMP (1-240) and y-axis time (0-1000 ms).

Interpretation

It is quite clear from Fig. A.12 that numerous reflectors were imaged in the subsurface, as deep as 900 ms, or roughly about 900 m. All of these reflectors are nearly flat-lying—complex structures such as faults or folds are not apparent. Since the pre-stack time migration resulted in the sharpest image, that is, one with the least noise and most coherent reflectors, it was chosen as the final image to be interpreted. Fig. A.13 shows the pre-stack time migration with several prominent reflectors picked.

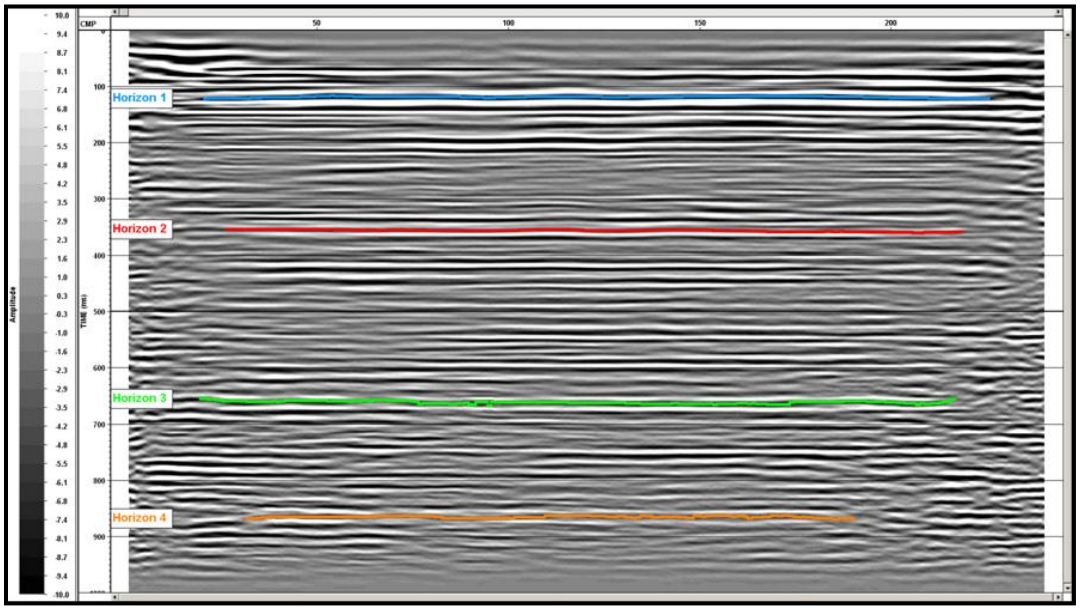

Fig. A.13. An interpreted pre-stack Kirchoff time-migrated section with several reflectors picked. X-axis represents CMP (1-240) and y-axis time (0-1000 ms).

It is important to note here that the topmost coherent signals, those above 100 ms, are most likely refractions (because of their low frequency content) and are therefore excluded from the interpretation. Also, one can see that the best-imaged portions of the

reflectors are in the center of migrated section, a result of the acquisition geometry which yielded the highest fold in the middle.

Although out-of-plane reflections may often be problematic when interpreting 2-D data, it is not a concern in this case because of the flat-lying nature of the reflectors—dipping layers and other complex structures are often the cause of such phenomena. In addition, multiples may exist in the final migrated section, although such contamination does not seem very likely because of the lack of cyclical reflections and "ringiness" within the data, due in part to the application of predictive decon. An autocorrelation of the pre-stack spiked data confirmed this assumption. Thus, the interpreted section seems to exhibit true acoustic impedances in the subsurface.

To better estimate the depth of the interpreted horizons within the pre-stack migrated section, a time-to-depth conversion was carried out using the velocity profile shown in Fig. A.11. Fig. A.14 shows the pre-stack time-migrated section next to the depth-converted seismic section, along with their respective interpreted horizons. The velocity structure is evident in the comparison between the two sections: the topmost horizons are compressed in the depth section while the lower horizons are expanded, as expected.

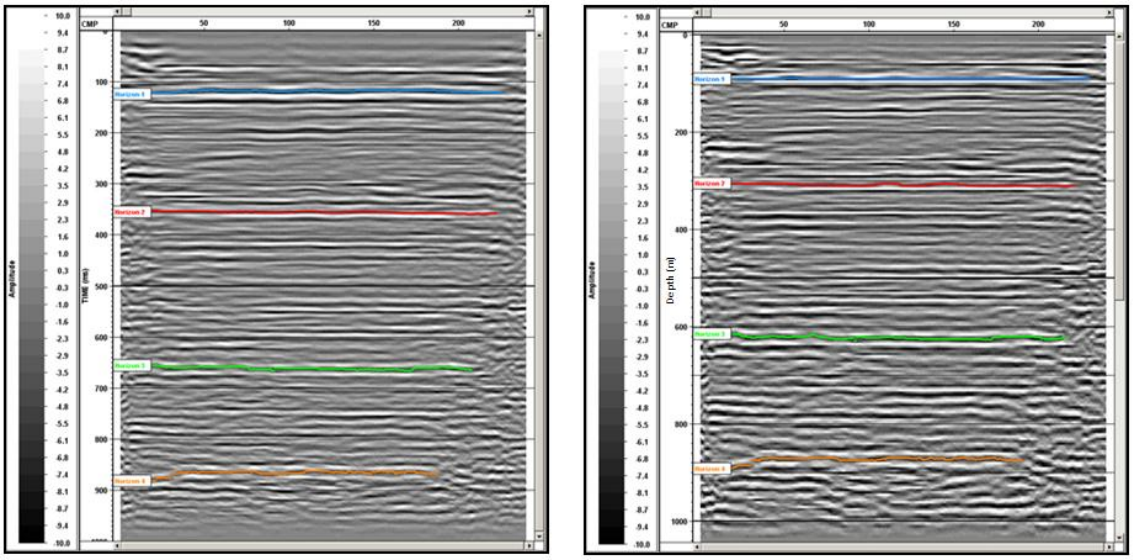

Fig. A.14. Interpreted pre-stack Kirchoff time-migration (left) and its respective time-to-depth converted section (right). X-axis represents CMP (1-240) and y-axis time (0-1000 ms).

In addition, since there are numerous producing oil and gas wells in the area, well logs from an offset well near the seismic survey area were obtained (offset well shown in Fig. A.3.). Although the producing reservoirs are 8800 ft deep or more, much deeper than the penetration depth of this survey, the well logs begin at a depth of about 1300 ft, or 400 m, allowing a portion of the seismic data to be correlated to well log data.

The suite of well logs consists of spontaneous potential (SP), gamma ray (GR), resistivity (ILS, ILM, ILD), tension (TENS), and caliper (DCAL) logs (Fig. A.15.). Using these logs, a simple facies analysis was conducted (Fig. A. 15) and the correlation was overlaid on the seismic data (Fig. A.16). The visual correlation of the well logs and seismic data is quite good—areas of high acoustic impedance on the seismic section correspond to lithologic changes on the well logs, as expected. However, the method is not perfect: the well logs were moved up about 50 m on the seismic section to create

greater agreement between the two, which could be the result of a slightly inaccurate velocity section. Also, not all lithologic changes correspond to noticeable acoustic impedances on the seismic section, which is common. Nonetheless, it is a first step in creating a detailed picture of the subsurface.

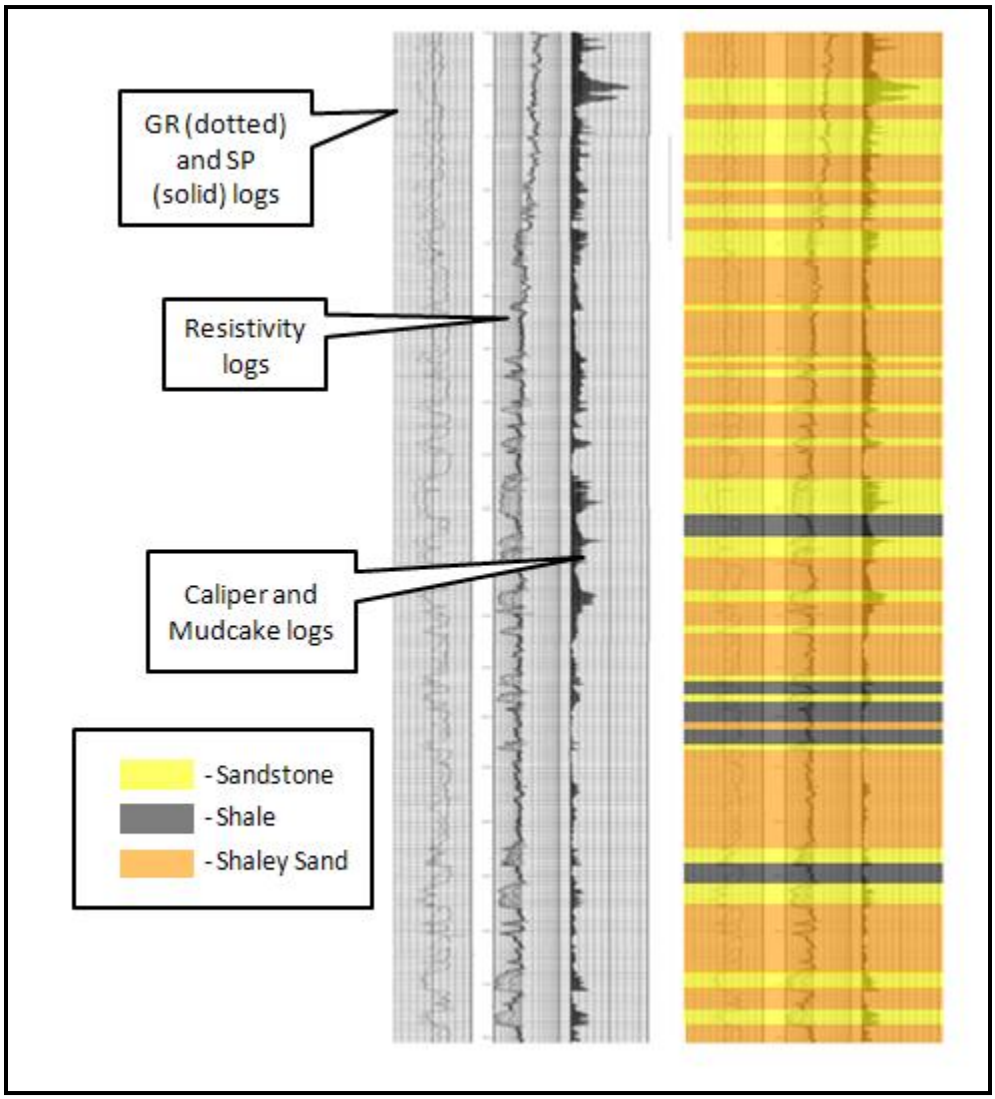

Fig. A.15. Well logs used for correlation to seismic data (left) and a facies interpretation of the well logs (right). Well API # 42-167-31368. GR scale is 0-150 API units. SP scale is -160-40 MV. Resistivity scale is 0.2-2000 OHMM on a logarithmic scale. Depth of logs is from 1,300' to 3,200'.

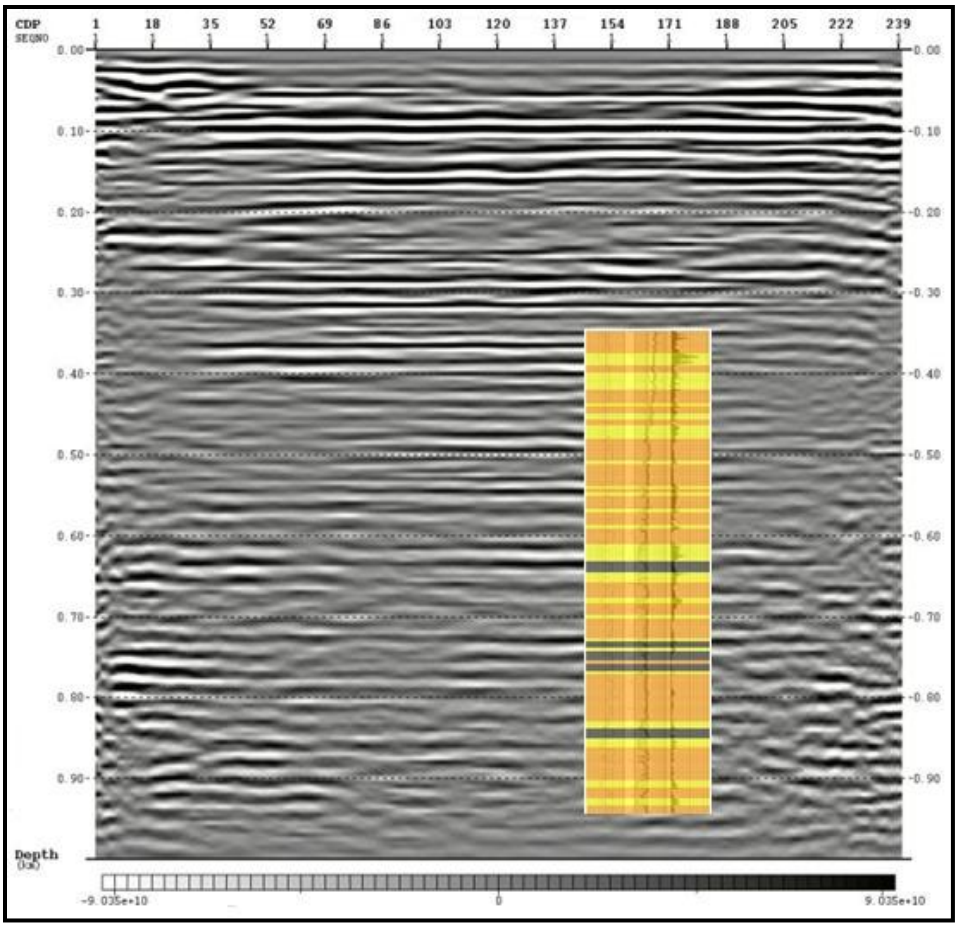

Fig. A.16. Depth-converted pre-stack time-migrated seismic section (background) with well logs from offset well 42-167-31368 in foreground. Well logs contain a color-coded facies analysis based on the GR, SP, and resisitivity logs: yellow, brown, and black represent sandstone, sandy shale, and shale, respectively. X-axis represents CMP (1-240) and y-axis time (0-1000 ms).

Conclusions

A single-component 360 m 2-D seismic line was acquired at the UHCC over a period of two days to test seismic equipment capabilities and to gain a better understanding of the subsurface at LaMarque, TX. The near-surface data were processed using a simple and conventional, yet sufficient, processing workflow to create an

appropriate image of the subsurface. Subsequent interpretation resulted in a flat and uniformly layered subsurface with very little complexity. Several prominent reflectors up to 900 m below the surface were interpreted. Well logs from an offset well were then used to visually correlate the depth-converted seismic data to down-hole log data.

The survey was a success: the geophysical equipment proved to be effective in imaging up to a kilometer beneath the surface and valuable information regarding the subsurface at the UHCC was obtained, which will no doubt pave the way for more extensive geophysical research in the area. Indeed, a longer seismic survey and a more powerful source, now feasible with the latest equipment, will allow for greater depth of penetration and better imaging capabilities, perhaps to the deeper hydrocarbon reservoirs themselves.

Appendix B—Houston, TX

Introduction

A seismic survey was conducted at the University of Houston Energy Research Park (UH-ERP), Houston, TX, on November 10th and 11th, 2011 (Fig. B.1). The purpose of this study was to compare the acquisition capabilities of two seismic sources: a 40 kg accelerated weight drop (AWD) and a "minivib" high fidelity acoustic projector (vibe). Although the vibe was expected to acquire data from deeper reflectors and of higher S/N, it was uncertain what the disparity between the two would be.

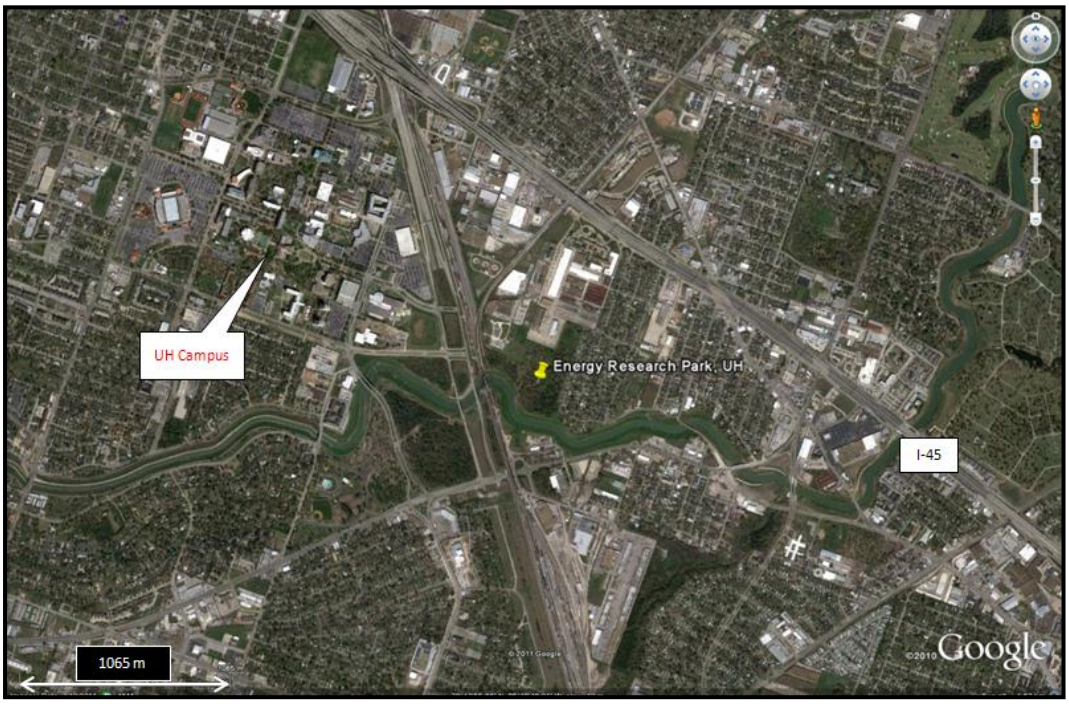

Fig. B. 1. Google Earth image of location of study area, shown by the yellow pindrop. Location of the University of Houston main campus is shown by the callout.

Acquisition

To carry out this test, 96 14-Hz single-component geophones with a spacing of 3 m were laid out in a straight line, resulting in a single 285 m 2-D receiver line (Fig. B.2). The geophones were connected to 24-bit Geometrics Geode analog-to-digital (A/D) converters and the data were acquired using Geometrics acquisition software on rugged field laptops. The shots, consisting of either 3 weight drops on a metallic base plate (which were automatically stacked in the field) or a 10-150 Hz sweep by the vibe, were located in between each pair of geophones and were also spaced 3 m apart. The total number of shot locations by each source type totaled 95. The recording time of the AWD source was 2 s and that of the vibe was 4 s.

Fig. B. 2. Google Earth image showing extent of the seismic line at UH-ERP, represented by the red line.

Processing

Upon acquisition, each data set underwent a similar processing workflow, which consisted of trace editing, predictive decon, filtering, gain, velocity analysis, NMO, stretch mute, brute stack, and noise attenuation (Fig. B.3). An inspection of the shot gathers by each of the two sources showed noticeable differences in data quality: the vibe data contain higher frequencies and have a higher S/N (Fig. B.4). Since there were no changes in the two surveys besides source type, the geometry and fold of the seismic lines remained the same (Fig. B.5). After predictive decon (20 ms lag) and f-k filtering were applied, a velocity analysis consisting of a semblance plot and constant velocity stacks was carried out. The resulting NMO velocity profile, shown in Fig. B.6, was applied to both data sets. After a 30% stretch mute was utilized, the data were stacked. To attenuate white noise and increase coherency, f-x decon and frequency filtering were applied to the stacked data. Finally, the data were converted from time to depth to compare the depth of penetration of the two data sets. The final stacked images of the AWD and vibe data are shown in Fig. B.7 and Fig. B.8, respectively.

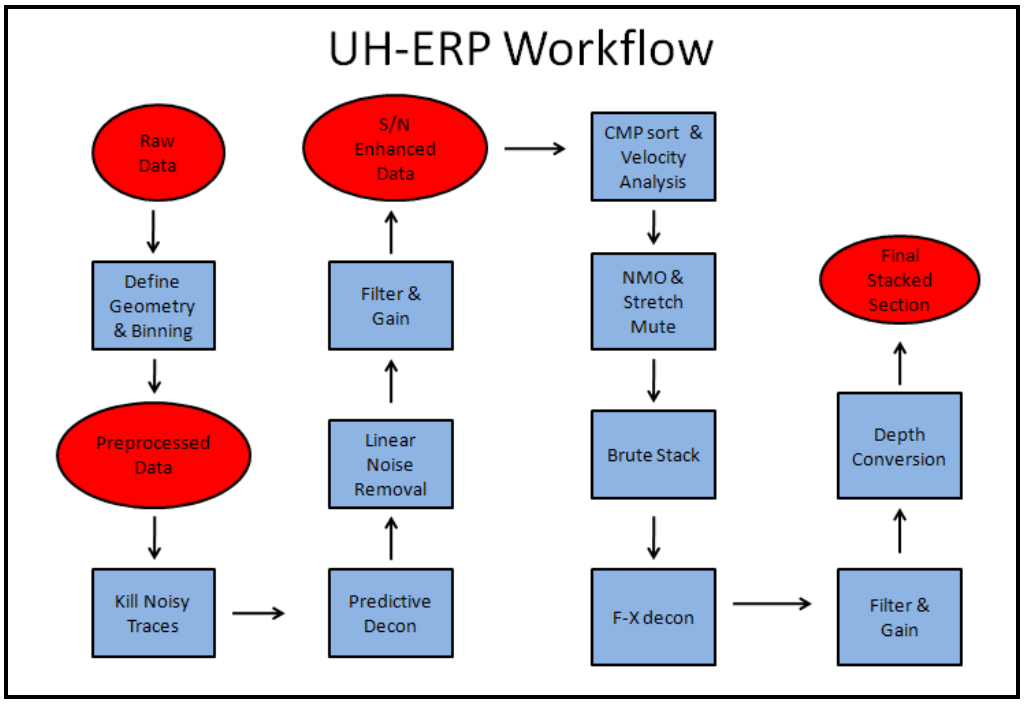

Fig. B. 3. Seismic processing workflow applied to UH-ERP seismic data.

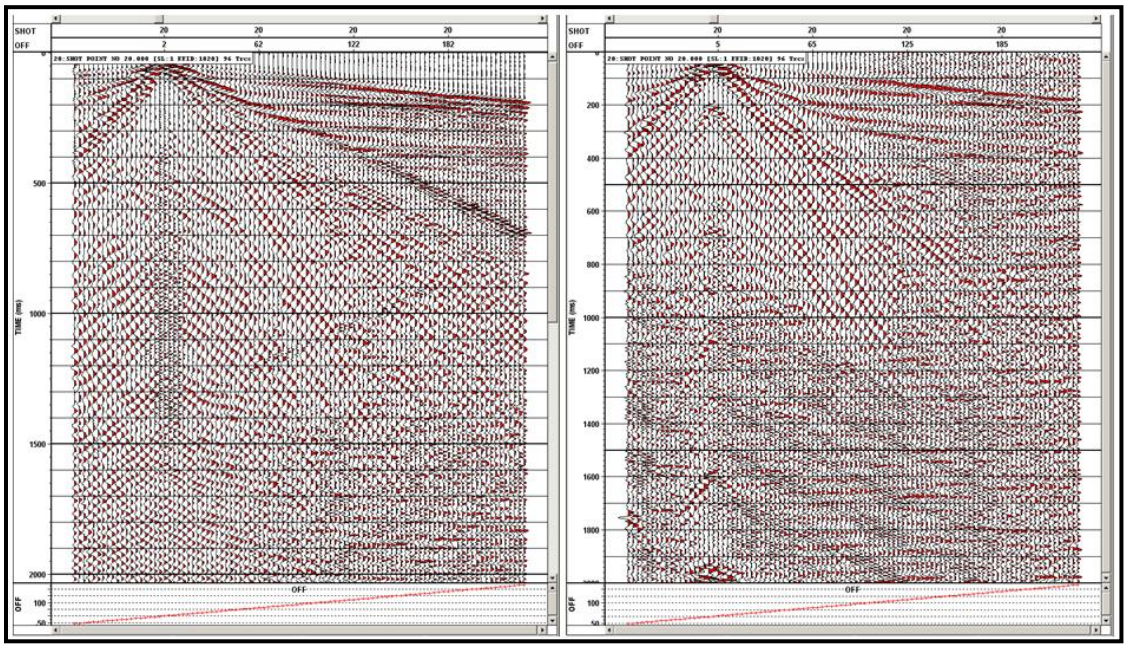

Fig. B. 4. A comparison of raw shot gather 20 using the vibe (left) and AWD (right) sources. The vibe data are clearly higher in frequency and have a higher S/N than the AWD, which allows reflections to to be discriminated more easily.

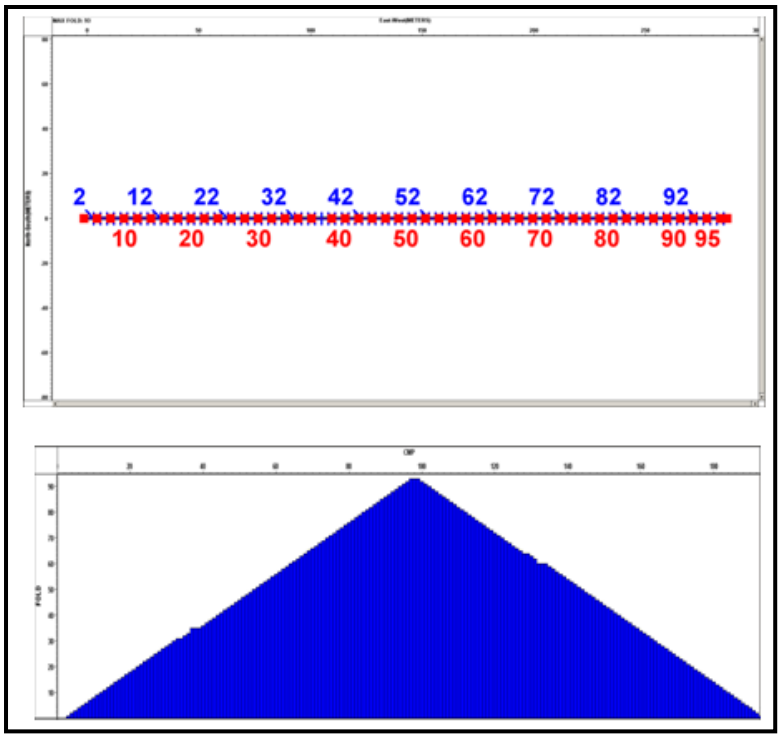

Fig. B. 5. Survey geometry (top) and subsurface CMP fold (bottom) of the UH-ERP seismic line of both surveys. The red boxes and blue crosses on the survey geometry indicate shot and receiver locations, respectively. The maximum subsurface CMP fold is 93.

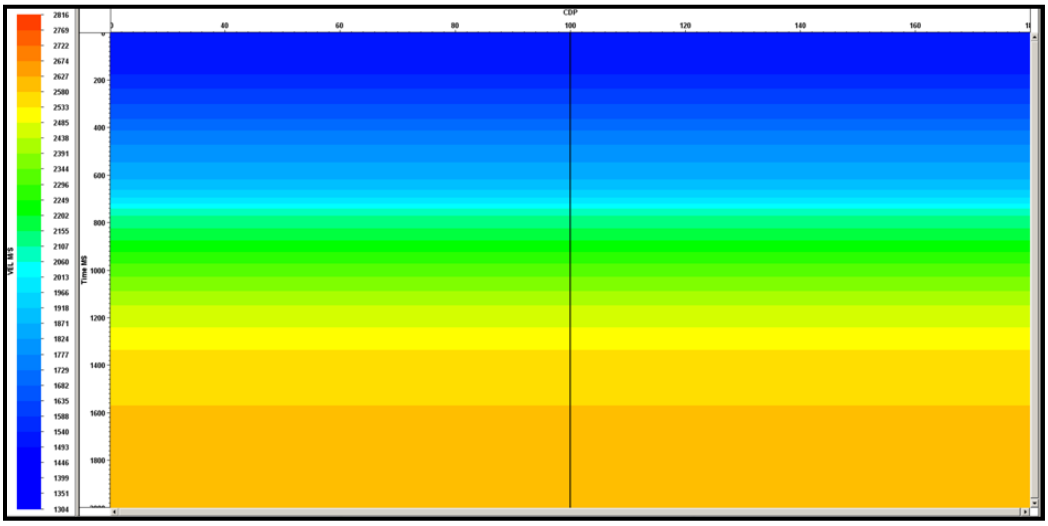

Fig. B. 6. NMO velocity profile of UH-ERP seismic line. It is flat because of the flat-lying sediments in subsurface, typical of the Texas Gulf Coast region.

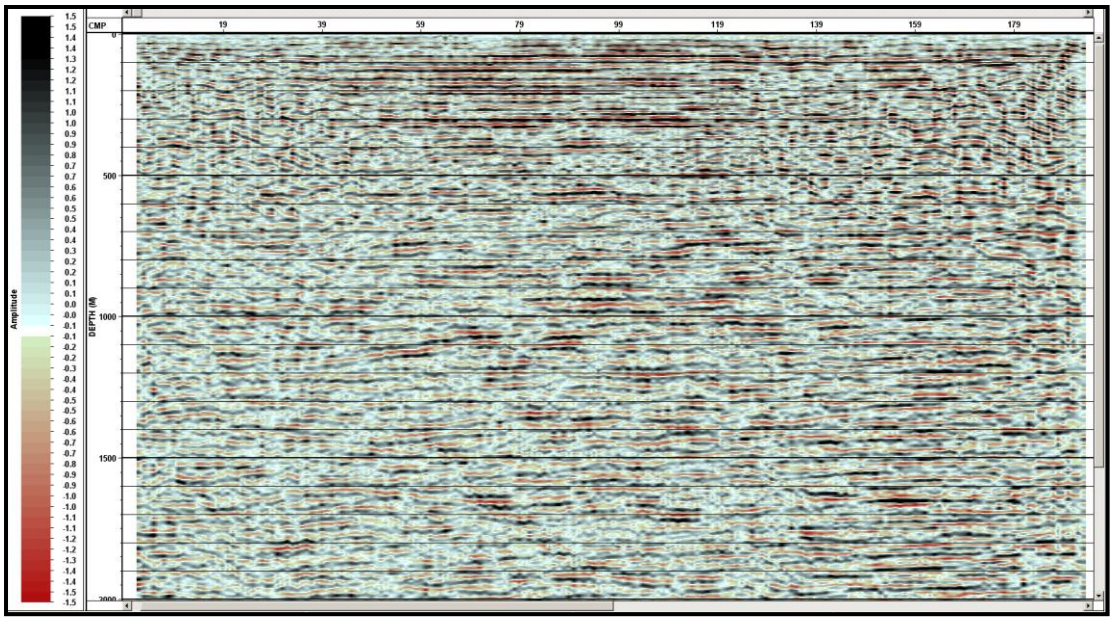

Fig. B. 7. Final stacked seismic section from the AWD survey. Reflectors are well-imaged within the top 300 m of the subsurface only. Deeper reflections are not coherent and cannot be confidently interpreted.

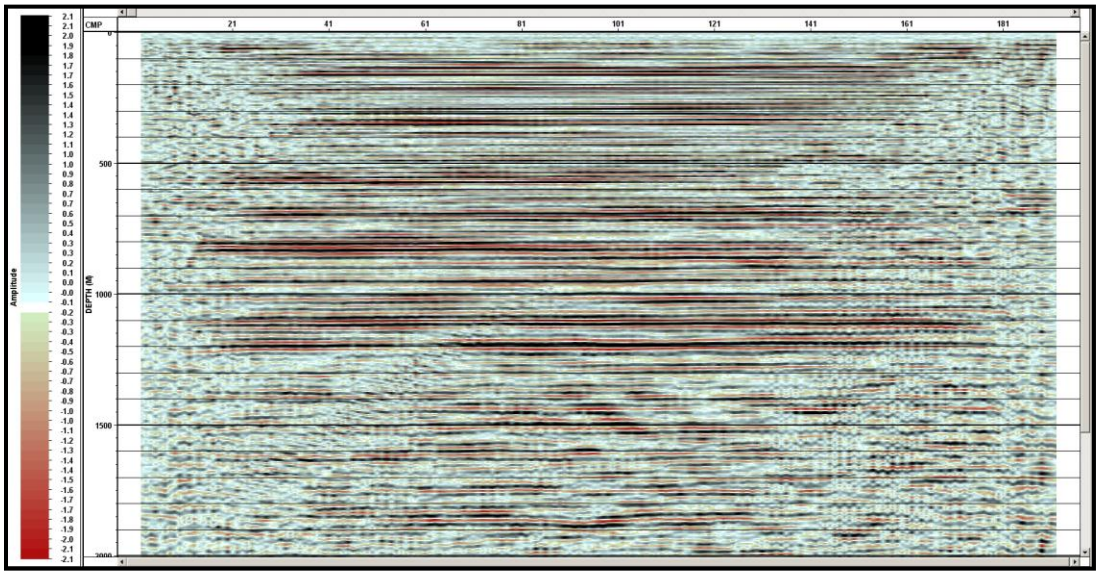

Fig. B. 8. Final stacked seismic section from the vibe survey. Reflectors are imaged well up to a depth of at least 1200 m, much greater than the AWD survey.

Discussion/Conclusions

It is clear from the results that even under favorable conditions (water-saturated fine-grained weathering layer and layer-cake subsurface geology), the vibe data are of much higher quality and penetrate much deeper. It is actually quite surprising how much the vibe data are improved over the AWD data: the depth of penetration of the vibe data seems to be up to 1200 m, whereas reflections within the AWD data can only be confidently interpreted to a depth of 300 m. Thus, it is quite clear that previously-acquired data with the AWD in places such as Meteor Crater and Jemez Pueblo can be significantly improved if the surveys are re-acquired using the vibe source.

Appendix C—Tables

Table 1. Meteor Crater Gravity Survey.

Line	Station	Latitude	Longitude	Elevation (m)	Local Time	Date	Mean Gravity Field (mGal)	Terrain Correction (mGal)
1	2	35.02236	-111.02153	1729.511	0.620116	5/17/2010	2428.83	2.43
1	3	35.02212	-111.02142	1723.100	0.627512	5/17/2010	2430.82	1.78
1	4	35.02187	-111.02126	1719.089	0.632141	5/17/2010	2432.03	1.30
1	5	35.02163	-111.02113	1716.038	0.637986	5/17/2010	2432.83	1.00
1	6	35.02139	-111.02100	1713.366	0.644109	5/17/2010	2433.61	0.78
1	7	35.02115	-111.02088	1710.753	0.648657	5/17/2010	2434.31	0.64
1	8	35.02090	-111.02075	1708.190	0.654618	5/17/2010	2435.00	0.56
1	9	35.02065	-111.02060	1705.262	0.659282	5/17/2010	2435.69	0.52
1	10	35.02042	-111.02047	1702.144	0.669456	5/17/2010	2436.20	0.53
1	11	35.02019	-111.02031	1702.144	0.675613	5/17/2010	2436.64	0.54
1	12	35.01992	-111.02019	1700.906	0.681296	5/17/2010	2436.99	0.56
1	15	35.01966	-111.02001	1699.407	0.453472	5/18/2010	2439.73	0.55
1	16	35.01941	-111.01989	1698.208	0.459363	5/18/2010	2439.03	0.51
1	17	35.01917	-111.01976	1697.011	0.467743	5/18/2010	2438.96	0.46
1	18	35.01892	-111.01963	1696.259	0.473681	5/18/2010	2439.00	0.41
1	19	35.01866	-111.01952	1695.576	0.480590	5/18/2010	2439.13	0.36
1	20	35.01841	-111.01935	1695.064	0.489444	5/18/2010	2439.20	0.33
1	21	35.01822	-111.01922	1694.957	0.495081	5/18/2010	2439.18	0.31
1	22	35.01799	-111.01910	1695.171	0.501701	5/18/2010	2439.14	0.31
1	23	35.01776	-111.01898	1694.550	0.508692	5/18/2010	2439.42	0.32
1	24	35.01752	-111.01883	1691.117	0.553275	5/18/2010	2439.93	0.33
1	25	35.01733	-111.01866	1689.260	0.561238	5/18/2010	2440.32	0.35
2	1	35.02196	-111.01693	1706.958	0.600463	5/18/2010	2436.50	0.59
2	2	35.02217	-111.01710	1708.728	0.606759	5/18/2010	2436.08	0.67
2	3	35.02234	-111.01730	1710.160	0.611539	5/18/2010	2435.57	0.81
2	4	35.02255	-111.01745	1712.195	0.615949	5/18/2010	2435.06	1.05
2	5	35.02274	-111.01761	1714.934	0.619850	5/18/2010	2434.31	1.35
2	6	35.02294	-111.01774	1718.616	0.625012	5/18/2010	2433.29	1.70
2	7	35.02312	-111.01787	1722.689	0.631111	5/18/2010	2432.04	2.00
2	9	35.02175	-111.01672	1706.313	0.655127	5/18/2010	2436.71	0.56
2	10	35.02154	-111.01653	1705.327	0.661400	5/18/2010	2436.96	0.54
2	11	35.02135	-111.01635	1705.404	0.667581	5/18/2010	2437.00	0.51
2	12	35.02119	-111.01615	1702.264	0.674815	5/18/2010	2437.73	0.49
2	15	35.02106	-111.01596	1697.532	0.403681	5/19/2010	2439.16	0.47
2	16	35.02090	-111.01575	1695.287	0.408611	5/19/2010	2439.75	0.46
2	17	35.02075	-111.01553	1693.633	0.414236	5/19/2010	2440.15	0.45
2	18	35.02059	-111.01530	1692.438	0.420220	5/19/2010	2440.48	0.45
2	19	35.02041	-111.01506	1691.178	0.425810	5/19/2010	2440.82	0.44
2	20	35.02025	-111.01485	1690.865	0.431655	5/19/2010	2440.96	0.42

Table 1. Meteor Crater Gravity Survey (cont'd).

2	21	35.02009	-111.01462	1688.358	0.436516	5/19/2010	2441.55	0.40
2	22	35.01995	-111.01436	1687.574	0.442025	5/19/2010	2441.79	0.37
3	1	35.02192	-111.01692	1706.802	0.476817	5/19/2010	2436.74	0.59
3	2	35.02188	-111.01719	1706.389	0.482731	5/19/2010	2436.78	0.57
3	3	35.02183	-111.01747	1706.347	0.487627	5/19/2010	2436.73	0.55
3	4	35.02176	-111.01776	1706.506	0.493079	5/19/2010	2436.61	0.54
3	5	35.02171	-111.01804	1706.703	0.497975	5/19/2010	2436.49	0.53
3	6	35.02164	-111.01831	1707.064	0.502465	5/19/2010	2436.34	0.51
3	7	35.02160	-111.01859	1707.922	0.509086	5/19/2010	2436.13	0.50
3	8	35.02154	-111.01888	1708.605	0.514074	5/19/2010	2435.84	0.47
3	9	35.02147	-111.01915	1708.573	0.519144	5/19/2010	2435.80	0.44
3	10	35.02142	-111.01943	1708.237	0.524931	5/19/2010	2435.77	0.42
3	11	35.02135	-111.01973	1709.098	0.539132	5/19/2010	2435.48	0.43
3	12	35.02130	-111.02004	1709.049	0.577546	5/19/2010	2435.45	0.44
3	13	35.02124	-111.02033	1708.987	0.583125	5/19/2010	2435.38	0.48
3	14	35.02118	-111.02065	1710.006	0.588137	5/19/2010	2435.17	0.56
3	15	35.02114	-111.02087	1710.632	0.593056	5/19/2010	2434.93	0.64
4	1	35.02310	-111.01555	1705.111	0.415301	5/20/2010	2437.75	0.63
4	2	35.02328	-111.01574	1707.452	0.418900	5/20/2010	2437.15	0.72
4	3	35.02345	-111.01591	1709.904	0.422731	5/20/2010	2436.52	0.84
4	4	35.02361	-111.01610	1712.932	0.426053	5/20/2010	2435.74	1.00
4	5	35.02376	-111.01629	1716.757	0.429780	5/20/2010	2434.71	1.25
4	6	35.02392	-111.01647	1722.055	0.434178	5/20/2010	2433.39	1.61
4	7	35.02407	-111.01665	1727.325	0.439306	5/20/2010	2431.78	2.06
4	8	35.02421	-111.01684	1733.660	0.444109	5/20/2010	2429.96	2.47
4	9	35.02293	-111.01533	1703.663	0.455093	5/20/2010	2438.18	0.55
4	10	35.02272	-111.01512	1702.050	0.459468	5/20/2010	2438.62	0.49
4	11	35.02257	-111.01491	1700.736	0.463831	5/20/2010	2439.04	0.44
4	12	35.02240	-111.01473	1697.987	0.469514	5/20/2010	2439.72	0.42
4	13	35.02222	-111.01454	1696.133	0.473854	5/20/2010	2440.24	0.43
4	14	35.02202	-111.01433	1694.127	0.477720	5/20/2010	2440.73	0.48
4	15	35.02185	-111.01413	1692.647	0.485405	5/20/2010	2441.10	0.47
5	1	35.02195	-111.01692	1706.936	0.552894	5/20/2010	2437.20	0.59
5	2	35.02206	-111.01667	1707.170	0.556574	5/20/2010	2437.20	0.60
5	3	35.02220	-111.01645	1706.737	0.559954	5/20/2010	2437.39	0.60
5	4	35.02235	-111.01625	1706.157	0.563692	5/20/2010	2437.55	0.60
5	5	35.02253	-111.01609	1705.408	0.568206	5/20/2010	2437.77	0.61
5	6	35.02273	-111.01592	1705.371	0.571563	5/20/2010	2437.81	0.63
5	7	35.02291	-111.01573	1705.112	0.576968	5/20/2010	2437.85	0.63
5	8	35.02311	-111.01556	1705.269	0.580637	5/20/2010	2437.86	0.63

Table 2. Meteor Crater Magnetic Survey.

Line	Station	Latitude	Longitude	Local Time	Date	Mean Magnetic Field (nT)
1	2	35.02236	-111.02153	0.451389	5/18/2010	49553.17
1	3	35.02212	-111.02142	0.444444	5/18/2010	49485.87
1	4	35.02187	-111.02126	0.684722	5/18/2010	49495.07
1	5	35.02163	-111.02113	0.437500	5/18/2010	49477.07
1	6	35.02139	-111.02100	0.430556	5/18/2010	49485.60
1	7	35.02115	-111.02088	0.423611	5/18/2010	49484.47
1	8	35.02090	-111.02075	0.416667	5/18/2010	49490.63
1	9	35.02065	-111.02060	0.409722	5/18/2010	49488.30
1	10	35.02047	-111.02047	0.402778	5/18/2010	49486.53
1	11	35.02019	-111.02031	0.395833	5/18/2010	49487.83
1	12	35.01992	-111.02019	0.388889	5/18/2010	49493.83
1	15	35.01966	-111.02001	0.515972	5/18/2010	49502.70
1	16	35.01941	-111.01989	12.210000	5/18/2010	49509.03
1	17	35.01917	-111.01976	0.513194	5/18/2010	49513.00
1	18	35.01892	-111.01963	0.511806	5/18/2010	49505.13
1	19	35.01866	-111.01952	0.477778	5/18/2010	49506.67
1	20	35.01841	-111.01935	0.484028	5/18/2010	49503.03
1	21	35.01822	-111.01922	0.490972	5/18/2010	49494.23
1	22	35.01799	-111.01910	0.496528	5/18/2010	49503.77
1	23	35.01776	-111.01898	0.503472	5/18/2010	49504.30
1	24	35.01752	-111.01883	0.554167	5/18/2010	49524.23
1	25	35.01733	-111.01866	0.557639	5/18/2010	49519.33
2	1	35.02196	-111.01693	0.596528	5/18/2010	49481.35
2	2	35.02217	-111.01710	0.602778	5/18/2010	49512.30
2	3	35.02234	-111.01730	0.608333	5/18/2010	49509.27
2	4	35.02255	-111.01745	0.613194	5/18/2010	49514.50
2	5	35.02274	-111.01761	0.617361	5/18/2010	49508.57
2	6	35.02294	-111.01774	0.621528	5/18/2010	49510.43
2	7	35.02312	-111.01787	0.627083	5/18/2010	49509.17
2	8	35.02330	-111.01801	0.634028	5/18/2010	49509.85
2	9	35.02175	-111.01672	0.650694	5/18/2010	49521.63
2	10	35.02154	-111.01653	0.656944	5/18/2010	49529.63
2	11	35.02135	-111.01635	0.662500	5/18/2010	49528.87
2	12	35.02119	-111.01615	0.670139	5/18/2010	49530.83
2	15	35.02106	-111.01596	0.400694	5/19/2010	49533.93
2	16	35.02090	-111.01575	0.406250	5/19/2010	49513.60
2	17	35.02075	-111.01553	0.410417	5/19/2010	49526.70
2	18	35.02059	-111.01530	0.416667	5/19/2010	49518.67
2	19	35.02041	-111.01506	0.422917	5/19/2010	49541.87
2	20	35.02025	-111.01485	0.428472	5/19/2010	49539.43
2	21	35.02009	-111.01462	0.433333	5/19/2010	49539.53
2	22	35.01995	-111.01436	0.438194	5/19/2010	49529.37

Table 2. Meteor Crater Magnetic Survey (cont'd).

3	1	35.02192	-111.01692	0.476389	5/19/2010	49567.07
3	2	35.02188	-111.01719	0.479861	5/19/2010	49522.57
3	3	35.02183	-111.01747	0.484722	5/19/2010	49550.23
3	4	35.02176	-111.01776	0.490278	5/19/2010	49526.27
3	5	35.02171	-111.01804	0.495139	5/19/2010	49545.70
3	6	35.02164	-111.01831	0.499306	5/19/2010	49530.53
3	7	35.02160	-111.01859	0.505556	5/19/2010	49540.63
3	8	35.02154	-111.01888	0.510417	5/19/2010	49554.33
3	9	35.02147	-111.01915	0.515972	5/19/2010	49528.57
3	10	35.02142	-111.01943	0.520833	5/19/2010	49525.77
3	11	35.02135	-111.01973	0.534722	5/19/2010	49530.27
3	12	35.02130	-111.02004	0.575000	5/19/2010	49506.33
3	13	35.02124	-111.02033	0.579861	5/19/2010	49538.80
3	14	35.02118	-111.02065	0.585417	5/19/2010	49540.80
3	15	35.02114	-111.02088	0.590278	5/19/2010	49539.93
4	1	35.02310	-111.01555	0.414583	5/20/2010	49501.10
4	2	35.02328	-111.01574	0.418056	5/20/2010	49501.20
4	3	35.02345	-111.01591	0.422222	5/20/2010	49508.57
4	4	35.02361	-111.01610	0.425000	5/20/2010	49502.50
4	5	35.02376	-111.01629	0.429167	5/20/2010	49487.23
4	6	35.02392	-111.01647	0.433333	5/20/2010	49498.78
4	7	35.02407	-111.01665	0.438194	5/20/2010	49504.20
4	8	35.02421	-111.01684	0.443750	5/20/2010	49498.17
4	9	35.02293	-111.01533	0.454861	5/20/2010	49542.43
4	10	35.02272	-111.01512	0.458333	5/20/2010	49542.50
4	11	35.02257	-111.01491	0.463194	5/20/2010	49547.33
4	12	35.02240	-111.01473	0.468750	5/20/2010	49554.50
4	13	35.02222	-111.01454	0.472917	5/20/2010	49553.93
4	14	35.02202	-111.01433	0.477083	5/20/2010	49555.30
4	15	35.02185	-111.01413	0.484722	5/20/2010	49560.60

Table 3. Jemez Pueblo Gravity Survey.

Station	Latitude	Longitude	Time	Mean Gravity Field (mGal)
1	35.58644	-106.75401	0.360451	2484.77
2	35.58658	-106.75379	0.366123	2484.76
3	35.58672	-106.75357	0.369722	2484.79
4	35.58685	-106.75335	0.374572	2484.80
5	35.58699	-106.75313	0.377882	2484.82
6	35.58718	-106.75299	0.381181	2484.82
7	35.58738	-106.75285	0.384363	2484.82
8	35.58757	-106.75270	0.388206	2484.82
9	35.58777	-106.75256	0.391956	2484.85
10	35.58796	-106.75242	0.394757	2484.85
11	35.58815	-106.75228	0.397650	2484.87
12	35.58835	-106.75213	0.400914	2484.89
13	35.58854	-106.75199	0.405544	2484.91
14	35.58873	-106.75185	0.408947	2484.90
15	35.58893	-106.75171	0.412546	2484.90
16	35.58912	-106.75156	0.415914	2484.90
17	35.58932	-106.75142	0.418588	2484.88
18	35.58951	-106.75128	0.422222	2484.86
19	35.58968	-106.75109	0.424850	2484.85
20	35.58984	-106.75091	0.428148	2484.83
21	35.59001	-106.75072	0.430625	2484.83
22	35.59018	-106.75054	0.434167	2484.82
23	35.59034	-106.75035	0.437662	2484.80
24	35.59051	-106.75017	0.441227	2484.77
25	35.59068	-106.74998	0.444884	2484.74
26	35.59085	-106.74980	0.448056	2484.73
27	35.59101	-106.74961	0.450926	2484.69
28	35.59118	-106.74943	0.453426	2484.62
29	35.59135	-106.74924	0.458669	2484.54
30	35.59151	-106.74906	0.461574	2484.48
31	35.59168	-106.74887	0.470104	2484.41
32	35.59179	-106.74865	0.472373	2484.32
33	35.59189	-106.74842	0.474838	2484.24
34	35.59195	-106.74815	0.477407	2484.12
35	35.59200	-106.74788	0.479873	2484.05
36	35.59206	-106.74761	0.483808	2484.06
37	35.59212	-106.74734	0.488391	2484.13
38	35.59218	-106.74707	0.492164	2484.02
39	35.59223	-106.74680	0.494907	2483.81
40	35.59229	-106.74653	0.497720	2483.61
41	35.59240	-106.74630	0.500197	2483.40
42	35.59252	-106.74608	0.502928	2483.21
43	35.59263	-106.74585	0.505556	2483.00
44	35.59272	-106.74561	0.508090	2482.82
45	35.59281	-106.74536	0.513287	2482.60
46	35.59290	-106.74512	0.515764	2482.41

Table 3. Jemez Pueblo Gravity Survey (cont'd).

47	35.59297	-106.74486	0.518194	2482.23
48	35.59303	-106.74459	0.521296	2482.02
49	35.59310	-106.74433	0.591412	2482.01
50	35.59317	-106.74406	0.593924	2481.88
51	35.59323	-106.74380	0.596597	2481.65
52	35.59330	-106.74353	0.599016	2481.43
53	35.59345	-106.74331	0.601921	2481.29
54	35.59360	-106.74310	0.604375	2481.26
55	35.59375	-106.74288	0.606690	2481.18
56	35.59387	-106.74265	0.609039	2481.12
57	35.59399	-106.74241	0.611435	2481.02
58	35.59411	-106.74218	0.613808	2480.97
59	35.59423	-106.74194	0.615914	2480.90
60	35.59434	-106.74171	0.618391	2480.83
61	35.59446	-106.74147	0.622396	2480.76
62	35.59458	-106.74124	0.625081	2480.68
63	35.59470	-106.74100	0.627419	2480.61
64	35.59482	-106.74077	0.629931	2480.56
65	35.59494	-106.74054	0.632350	2480.55
66	35.59506	-106.74030	0.636042	2480.53
67	35.59518	-106.74007	0.638704	2480.45
68	35.59530	-106.73983	0.641701	2480.39
69	35.59541	-106.73960	0.644167	2480.35
70	35.59553	-106.73936	0.647477	2480.27
71	35.59565	-106.73913	0.650012	2480.14
72	35.59577	-106.73889	0.652569	2479.97
73	35.59589	-106.73866	0.655370	2479.79